84

13988

MICROFILMED—1984

Downloaded from SHAREOK. Persistent Handle URL: https://hdl.handle.net/11244/5220

INFORMATION TO USERS

This reproduction was made from a copy of a document sent to us for microfilming. While the most advanced technology has been used to photograph and reproduce this document, the quality of the reproduction is heavily dependent upon the quality of the material submitted.

The following explanation of techniques is provided to help clarify markings or notations which may appear on this reproduction.

1. The sign or "target" for pages apparently lacking from the document photographed is "Missing Page(s)". If it was possible to obtain the missing page(s) or section, they are spliced into the film along with adjacent pages. This may have necessitated cutting through an image and duplicating adjacent pages to assure complete continuity.

2. When an image on the film is obliterated with a round black mark, it is an indication of either blurred copy because of movement during exposure, duplicate copy, or copyrighted materials that should not have been filmed. For blurred pages, a good image of the page can be found in the adjacent frame. If copyrighted materials were deleted, a target note will appear listing the pages in the adjacent frame.

3. When a map, drawing or chart, etc., is part of the material being photographed, a definite method of "sectioning" the material has been followed. It is customary to begin filming at the upper left hand corner of a large sheet and to continue from left to right in equal sections with small overlaps. If necessary, sectioning is continued again—beginning below the first row and continuing on until complete.

4. For illustrations that cannot be satisfactorily reproduced by xerographic means, photographic prints can be purchased at additional cost and inserted into your xerographic copy. These prints are available upon request from the Dissertations Customer Services Department.

5. Some pages in any document may have indistinct print. In all cases the best available copy has been filmed.

University
Microfilms
International

300 N. Zeeb Road
Ann Arbor, MI 48106

8413988

Ziegler, Conrad Lawrence

RETRIEVAL OF THERMAL AND MICROPHYSICAL VARIABLES IN OBSERVED CONVECTIVE STORMS

The University of Oklahoma PH.D. 1984

University
Microfilms
International 300 N. Zeeb Road, Ann Arbor, MI 48106

PLEASE NOTE:

In all cases this material has been filmed in the best possible way from the available copy. Problems encountered with this document have been identified here with a check mark ✓.

1. Glossy photographs or pages _____
2. Colored illustrations, paper or print _____
3. Photographs with dark background _____
4. Illustrations are poor copy ✓
5. Pages with black marks, not original copy _____
6. Print shows through as there is text on both sides of page _____
7. Indistinct, broken or small print on several pages ✓
8. Print exceeds margin requirements _____
9. Tightly bound copy with print lost in spine _____
10. Computer printout pages with indistinct print _____
11. Page(s) _____ lacking when material received, and not available from school or author.
12. Page(s) _____ seem to be missing in numbering only as text follows.
13. Two pages numbered _____. Text follows.
14. Curling and wrinkled pages _____
15. Other _____

University Microfilms International

THE UNIVERSITY OF OKLAHOMA

GRADUATE COLLEGE

RETRIEVAL OF THERMAL AND MICROPHYSICAL VARIABLES IN OBSERVED CONVECTIVE STORMS

A DISSERTATION

SUBMITTED TO THE GRADUATE FACULTY

in partial fulfillment of the requirements for the

degree of

DOCTOR OF PHILOSOPHY

By

CONRAD LAWRENCE ZIEGLER

Norman, Oklahoma

1984

RETRIEVAL OF THERMAL AND MICROPHYSICAL VARIABLES

IN OBSERVED CONVECTIVE STORMS

APPROVED BY

DISSERTATION COMMITTEE

ACKNOWLEDGEMENTS

I wish to express my deep appreciation to Dr. Peter Ray, who has been my able mentor and good friend over the many productive years that we have worked together. Dr. Edwin Kessler provided fundamental insight into the interactions of wind and water substance during his graduate course entitled "Perspectives on Storm Systems," and my subsequent efforts to relate derived thunderstorm airflow and precipitation have been strongly influenced by his teachings. The many helpful discussions with and comments by Prof. Yoshi Sasaki, Dr. Carl Hane and Prof. Luther White during the course of this research are gratefully acknowledged. A special acknowledgement is extended to Prof. John Pflaum for a particularly thorough and insightful review of the manuscript. Prof. Robert Wilhelmson of the University of Illinois and Dr. Joseph Klemp of NCAR contributed invaluable advice during the programming phase of the model, and graciously provided a data set simulated with their dynamic model for tests of the retrieval method used in this research. Prof. Henry Leighton of McGill University generously provided the computer code for a finite difference coalescence model and made a considerable effort to explain the algorithm. I wish to thank Ms. Lynda McGinley, Ms. Sandra McPherson, and Ms. Michelle Foster for their patience in skillfully typing the manuscript. Ms. Joan Kimpel, Mr. Robert Goldsmith, and Mr. Charles Clark are gratefully acknowledged for providing drafting and photographic services. I would also like to thank my wife Diane and my parents Benjamin and Dorothy Ziegler for their loving and enthusiastic support during the long course of this research effort.

Retrieval computations with the three dimensional kinematic model were performed on the IBM 3081 machine at the Merrick Computer Facility at the University of Oklahoma. The majority of the research was supported by a graduate research assistantship at the Cooperative Institute of Mesoscale Meteorological Studies and the University of Oklahoma. Additional support was provided under NSF grant ATM-821-1399 and NOAA Task II NA80-RAH00004.

ABSTRACT

The study of air flow in convective storms, the forces that regulate the flow, and the processes that produce hydrometeors of various kinds, are all being studied intensively by meteorologists using Doppler radar observations. The research reported here proceeds from the observed motion through accompanying thermodynamic and microphysical processes to the analysis of hydrometeor content and thermal fields in thunderstorms. A three dimensional numerical kinematic cloud model employing fixed Doppler wind fields, is used to diagnose temperature and mixing ratios and assess the relative importance of the various thermodynamic, microphysical and transportive forcing mechanisms. The microphysical parameterization includes stochastic coalescence effects in warm clouds as well as wet and variable density dry hail growth.

Preliminary model tests using input from a dynamically simulated cloud establish the accuracy of the retrieval scheme. Real data tests indicate good agreement between retrieved and observed radar reflectivities, qualitative dynamic consistency between observed winds and retrieved buoyancies, and the model's ability to partition liquid and solid hydrometeors. Results further show that the overall echo configuration is controlled by the wind field while echo details are controlled by transients, the wind field, and the cloud microphysics. Recycling of millimetric ice, graupel and drops may strongly modulate storm core precipitation characteristics. Systematic or non-random wind analysis errors are detectable in principle by observing major differences between retrieved and observed reflectivities, provided that other sources of retrieval error are negligible.

List of Symbols and Notations

A_1, A_2	temperature-dependent parameters in deposition growth equation
A'	coefficient in Bigg freezing equation
a	parameter in Teten's formula, parameter in expression for ice nucleus concentration
a_1, a_2, a_3, a_4	coefficients in polynomial collection kernels
B'	parameter in Bigg freezing equation
b	parameter in Teten's formula
C	hydrometeor ventilation coefficient, coefficient in expression for aerosol concentration
c	parameter in expression for turbulent mixing coefficient, advection speed
C_D	hailstone drag coefficient
c_p	specific heat of air at constant pressure
D	diameter
D_g	ice-hail conversion threshold
D_w	transition diameter from dry to wet hail growth
d	droplet diameter
D_ϕ	turbulent diffusion rate
E_c	coalescence efficiency
E_i	wet hail coalescence efficiency for cloud ice
E_{ic}	cloud ice coalescence efficiency for cloud
f_v	ventilation factor
f_o	parameter in cloud ice melting equation
g	acceleration of gravity
H	depth of convection
K	collection kernel, mixing coefficient

K_D	fourth-order filter coefficient
K_ϕ	turbulent mixing coefficient
k	parameter in expression for aerosol concentration
k_a	thermal conductivity of air
L	liquid water content
L_v	latent heat of vaporization
L_f	latent heat of fusion
L_s	latent heat of sublimation
ℓ	grid cube volume
M	confluent hypergeometric Kummer function
M_ϕ	microphysical rate
M_o	zeroth moment of distribution
M_1	first moment of distribution
M_n	n-th moment of distribution
M_{oc}	zeroth moment of cloud distribution
M_{or}	zeroth moment of rain distribution
M_{1c}	first moment of cloud distribution
M_{1r}	first moment of rain distribution
N	number concentration
N_o	intercept parameter, coefficient in expression for ice nucleus concentration
N_c	cloud distribution number concentration
N_r	rain distribution number concentration
N_i	ice nucleus concentration
N_{oh}	hail distribution intercept parameter
N_{oi}	ice distribution intercept parameter

n	spectral number density
P	polynomial kernel approximation
Pr	eddy Prandtl number
p	pressure
p_o	reference pressure
q_v	vapor mixing ratio
q_c	cloud mixing ratio
q_r	rain mixing ratio
q_h	hail mixing ratio
q_i	ice mixing ratio
q_x	cloud ice mixing ratio
q_w	wet hail fraction
q_{vs}	saturation mixing ratio over plane water surface
q_{is}	saturation mixing ratio over plane ice surface
R	gas constant for dry air, collector drop radius
R_i	average radius of ice particle for cloud accretion
R1	rate of cloud nucleation
R2	rate of cloud condensation/evaporation
R3	rate of cloud self-collection for cloud concentration
R4	rate of cloud self-collection for rain concentration
R5	rate of cloud self-collection for cloud, rain mixing ratio
R6	rate of rain accretion of cloud for cloud concentration
R7	rate of rain accretion of cloud for cloud, rain mixing ratio
R8	rate of rain self-collection

R9	rate of rain evaporation
R10	rate of rain freezing for rain concentration
R11	rate of rain freezing for rain, ice mixing ratio
R12	rate of rain sedimentation for rain concentration
R13	rate of rain sedimentation for rain mixing ratio
R14	rate of dry mode hail accretion of cloud for cloud concentration
R15	rate of dry mode hail accretion of cloud for cloud, hail mixing ratio
R16	rate of wet mode hail accretion of cloud for cloud concentration
R17	rate of wet mode hail accretion of cloud for cloud, hail mixing ratio
R18	rate of hail accretion of ice
R19	rate of hail melting for rain concentration
R20	rate of hail melting for rain, hail mixing ratio
R21	rate of hail sedimentation
R22	rate of ice nucleation
R23	rate of ice deposition
R24	rate of ice accretion of cloud for cloud concentration
R25	rate of ice accretion of cloud for cloud, ice mixing ratio
R26	rate of ice sublimation
R27	rate of ice melting for rain concentration
R28	rate of ice melting for rain, ice mixing ratio
R29	rate of ice-hail conversion
R30	rate of ice sedimentation

R31	rate of cloud water freezing to cloud ice for cloud concentration
R32	rate of cloud water freezing to cloud ice for cloud, cloud ice mixing ratio
R33	rate of cloud ice sublimation
R34	rate of cloud ice melting/evaporation
R_h	radius at which rain peak appears
r_o	mean volume drop radius of cloud droplet and rain drop distributions
r_1	coefficient in saturation adjustment
s	supersaturation
T_c, T_a	undercooling
T_s	hailstone surface undercooling
t	time
u	x-component of air motion, dummy index for drop volume
V	terminal fallspeed
V_r	terminal fallspeed of rain
V_h	terminal fallspeed of hail
V_i	terminal fallspeed of ice
V_{ri}	rain-equivalent ice terminal fallspeed
v	y-component of air motion, drop volume
v_i	equivalent volume of nucleated ice crystal
v_o	mean drop volume
W	updraft velocity scale
x	drop volume, east-west coordinate, change of variable
y	north-south coordinate
Z	radar reflectivity

Z_e	equivalent radar reflectivity
z	vertical coordinate
δ	generalized difference operator
Δ	increment
Γ	complete Gamma function
γ	incomplete gamma function
λ	slope parameter
λ_h	hail distribution slope parameter
λ_i	ice distribution slope parameter
ν	gamma distribution shape parameter, kinematic viscosity of air
ν_c	cloud distribution shape parameter
ν_r	rain distribution shape parameter
π	Exner function, Pi
κ	power in Exner function definition
ρ	air density
ρ_h	hail density
ρ_i	ice density
ρ_o	surface air density
ρ_v	ambient vapor density
ρ_w	water density
ρ_{si}	saturation vapor density over ice
σ	standard deviation
τ	time level of finite-difference model integration, time scale
ξ	generalized independent variable
θ	reference potential temperature

θ	potential temperature
θ'	deviation potential temperature
ϕ	arbitrary model variable

Notations

$\bar{(\ )}$	Base state quantity, horizontal average
$(\ )'$	Error quantity
$\tilde{(\ )}$	Observed quantity
$\dot{(\ )}$	Substantial derivative
$\hat{(\ )}$	Empirical law
$L(\ )$	Laplace transform
$E[\ ]$	Statistical expectation

TABLE OF CONTENTS

		PAGE
ACKNOWLEDGEMENTS		iii
ABSTRACT		v
SYMBOLS AND NOTATION		vi
CHAPTER		
I.	INTRODUCTION	1
	1.1 The problem in perspective	1
	1.2 Historical background	2
	1.3 Continuity principles	7
	1.4 Scope of research	8
II.	THE MODEL EQUATIONS	10
	2.1 The kinematic framework	10
	2.2 The microphysical framework	12
	2.2.1 Condensation/evaporation adjustment	21
	2.2.2 Cloud nucleation parameterization	22
	2.2.3 Warm rain coalescence parameterization	23
	2.2.4 Collisional breakup parameterization	28
	2.2.5 Hail parameterization	29
	2.2.6 Ice parameterization	29
	2.2.7 Cloud ice parameterization	31
	2.2.8 Hydrometeor sedimentation	31
	2.3 The numerical framework	32
	2.4 Model solution	35
III.	KINEMATIC MODEL VERIFICATION TESTS	38
	3.1 Experimental procedure	38
	3.2 Results of retrieval experiments	39
	3.3 Analysis of retrieval error	54
IV.	MODEL TESTS WITH REAL DATA	64
	4.1 Real data initialization	65
	4.2 Model tests with 27 May data	66
	4.3 Model tests with 28 May data	101
	4.4 Precipitation growth rates	119
	4.5 Hail growth on 28 May 1977	126
V.	SUMMARY	132
	5.1 Results	132
	5.2 Model limitations	139
	5.3 Recommendations for future research	140
BIBLIOGRAPHY		142

APPENDICES

A. ANALYTIC INTEGRATION METHODS..... 149

B. PROPERTIES OF THE GAMMA DISTRIBUTION MODEL..... 151

C. WARM CLOUD PARAMETERIZATION..... 154
1. Cloud autoconversion parameterization..... 154
2. Rain accretion of cloud parameterization..... 160
3. Large hydrometeor self-collection..... 163
4. Collisional breakup parameterization..... 164
5. Cloud droplet condensation growth parameterization 166
6. Cloud nucleation parameterization..... 168
7. Rain evaporation parameterization..... 170

D. HAIL PARAMETERIZATION..... 172
1. Hail distribution model..... 172
2. Computation of the incomplete gamma function..... 174
3. Transition diameter D_w for dry/wet growth..... 176
4. Hail dry growth parameterization..... 177
5. Hail wet growth parameterization..... 182
6. Hail melting to rain..... 184
7. Hail accretion of ice..... 185

E. CLOUD ICE PARAMETERIZATION..... 187
1. Ice distribution model..... 187
2. Raindrop freezing to ice..... 188
3. Cloud ice nucleation parameterization..... 189
4. Ice riming of cloud..... 191
5. Deposition growth of ice..... 192
6. Ice/hail conversion..... 194
7. Cloud ice melting to rain..... 194
8. Sublimation of ice to vapor..... 195

F. CLOUD ICE SUBLIMATION..... 196

CHAPTER I

INTRODUCTION

1.1 The problem in perspective

Thunderstorm precipitation has a great impact on man's activities. Thunderstorm rains benefit agriculture, although flooding and soil erosion as a result of heavy rains may have serious negative consequences. These storms often produce damaging hail, which accounts for three-quarters of a billion dollars[1] in crop loss each year, and disastrous flash floods such as that at Big Thompson Canyon (Kessler, Ed., 1981).

Our interest in thunderstorms leads to questions about the various physical processes within them. How is updraft water vapor ultimately converted to precipitation? How is the precipitation distributed by air currents? What effect if any does precipitation have on the air currents? Meteorologists have developed physical theories of hydrometeor formation and growth processes although the concerted action of those processes on precipitation in actual thunderstorms is not well understood. The lack of observations of temperature and water vapor, quantities which are critical to the distribution of cloud, severely hampers attempts to study precipitation processes.

Knowledge of how precipitation mechanisms interact in thunderstorms would facilitate the interpretation of radar observations by forecasters and researchers. The availability of independent estimates of hydrometeor type and concentration would improve interpretation of radar

[1] 1975 dollars.

reflectivity, which is affected by hydrometeor phase or type (hail or ice) as well as number and size of precipitation particles. A technique for dividing the water field into liquid and solid parts may improve short-range hail and flash flood warnings based on radar observations, by relating radar echo features to the precipitation fields particular to the storm being observed. The thermal and water vapor buoyancy and precipitation loading represent forces that regulate air flow in thunderstorms, and a method of diagnosing these accelerations would assist studies of cloud processes and contribute to improved short range forecasting of storm intensity.

1.2 Historical background

Conceptual thunderstorm models developed since World War II have emphasized close relationships between fields of airflow and precipitation. The Thunderstorm Project (Byers and Braham, 1949) documented the existence of updrafts that provide condensate and balance the fallspeed of growing raindrops, and adjacent downdrafts which may arise from water load and allow drops to fall to the surface in a region of divergence at low altitude. Browning (1964) accounted for the hook echo, the sloping echo overhang in vertical cross-section, and the cyclonic rotation of portions of the echo, by a flow model which featured a cyclonically turning updraft tilted into the wind shear at low levels and a downdraft within the precipitation area adjacent to the updraft. Precipitation formed in and near the updraft in middle levels and shared the rotating horizontal motion of the air as it descended in the downdraft, thus forming an echo core tilted into the horizontal inflow and eventually a hook-shaped appendage of the low level precipitation field. Browning

(1965) associated the echo-free vault with an intense updraft which swept small hydrometeors through the cloud top before growth to radar-detectable size could occur. Browning further noted that a curtain of precipitation from a neighboring cell could be drawn into the base of the main updraft with abrupt uplifting, thereby illuminating the horizontal inflow and the narrowness of the zone of strong rising motion.

Marwitz (1972) found that subcloud air tends to flow into the reflectivity gradient bordering the vault, in contrast to the Browning model in which inflow streams in parallel with the edge of the vault. Hence, precipitation from aloft falls through the inflow in the reflectivity gradient bordering the vault, due to a combination of diminishing updraft and increasing fallspeed. Chisholm (1973) documented a strong relation between wind and reflectivity fields in Alberta hailstorms, noting in particular the "controlling influence" on storm structure exerted by "the environmental wind field, the intensity of the updraft, and the formation of precipitation and its interaction with the updraft."

The development of thunderstorm precipitation is related to the persistence, strength, and spatial variation of updraft, which provides condensate but may be too narrow and strong to provide adequate hydrometeor growth time. Browning and Foote (1976) argued that the intense and quasi-steady updraft tended to produce a persistent region of weak radar echo, due to the small rate of droplet coalescence characterizing continental clouds. The edge of the weak echo region or vault indicated the occurrence of hydrometeor growth by the collection of cloud droplets. This region was believed to contain favorable growth trajectories

arising from the coexistence of moderate cloud water content and moderate updrafts which suspended particles rather than sweeping them rapidly upward. Although the intense, single cell storm might not prefer hydrometeor trajectories passing through the updraft core where maximum cloud water and accretion rates are expected, a non-steady updraft might permit such favorable trajectories. Chalon et al. (1976) documented a Colorado multicellular storm which had as many as three cells in various evolutionary stages at a given instant. Individual cells in the transient mature stage possessed the weak echo region and forward overhang characteristic of severe unicellular storms, although periods of weaker circulation associated with hydrometeors entering the updraft core and the demise of the weak echo region. A comprehensive review of conceptual models relating airflow and precipitation fields in severe storms has been presented by Browning (1977).

The advent of the Doppler radar in thunderstorm research has had a significant impact on studies relating to airflow and precipitation fields, since knowledge of the velocity removes certain deductive aspects which were characteristic of classical efforts. Foote and Frank (1983) employed multiple Doppler observations to study the modulation of the classical quasi-steady main updraft and reflectivity structure by a series of smaller cellular developments which sequentially moved through the main cell of a Colorado storm. A multicellular Colorado storm studied by Miller and Fankhauser (1983) possessed a main cell with supercell characteristics. Doppler derived updrafts coincided with the vault from near the surface to 7 km, with an echo overhang in the updraft above 7 km. The precipitation core reached the ground within a

downdraft situated downwind of the updraft with respect to the low level inflow. Nelson (1983) used Doppler wind fields and a numerical hail growth model to study a supercell hailstorm, concluding that a broad region of moderate updraft may be necessary for large hail growth. This result concurs with the earlier finding that inefficient precipitation growth produces the vault region of intense storms. These studies support the theory that precipitation and cloud structures respond to details of the wind field.

Relationships between airflow and the temperature and water vapor fields are not as well understood as is the case with precipitation, owing to a paucity of direct observations. Several important aspects of the thunderstorm thermal fields have nonetheless emerged, in preliminary efforts to understand the distribution of buoyancy which contributes to the vertical acceleration of air parcels and regulates the supply of condensate via the saturated adiabatic process. From observations of non-uniform depth of penetration of the stratosphere by thunderstorm tops, Newton (1966) deduced that a typical updraft is composed of two roughly annular regions, the core and the sheath. Air in the core is adiabatic and unmixed and realizes maximum kinetic energy via thermally buoyant acceleration, while air in the surrounding outer sheath experiences variable degrees of mixing with the environment and acquires a lower equilibrium level than the core. Downdrafts ingest potentially cold middle level air and evaporation of precipitation accelerates negatively buoyant descent.

Studies by Barnes (1970) and Davies-Jones (1974) of balloon soundings taken in updrafts of Oklahoma storms, reveal that updrafts extend

virtually undiluted through middle levels and possess moist adiabatic lapse rates. The latent heat release under water-saturated conditions yields thermally buoyant acceleration consistent with the observed updraft profile estimated from excess balloon rise rate. Updrafts are weaker than predicted by a simple adiabatic parcel model that does not account for association of vertical and horizontal airflow kinetic energies via the pressure field. A study of Colorado cumulus congestus by Heymsfield et al. (1978) reveals moist adiabatic lapse rates which indicate a low level inflow source. Fankhauser (1976) reports high values of equivalent potential temperature below cloud base in the region of inflow to the updraft, which suggest that air originating in the lowest 500 m feeds the updraft.

The representation of cloud processes by dynamical cloud models provides complete and internally consistent field of cloud airflow, temperature, and water substance for comparison with observations and verification of conceptual thunderstorm models. The 2-dimensional models of Hane (1973) and Orville and Kopp (1977), which describe cloud evolution in one horizontal dimension as well as the vertical, simulate classical cloud features such as the adjacent updraft and downdraft, the precipitation overhang aloft with descending core in the low level downdraft, and a rather undiluted, moist-adiabatic updraft. The 3-dimensional models of Klemp and Wilhelmson (1978), Schlesinger (1978), and Clark (1979) avoid the flow distortion characteristic of the 2-dimensional models, and additionally simulate updraft rotation and precipitation descent outside the plane of storm inflow. The simulated airflow and the thermal and precipitation fields agree with the main

features of classical conceptual models. Klemp et al. (1981) report encouraging agreement between the simulated and observed airflow and precipitation fields in a mature supercell storm. The simulated precipitation overhang near the updraft summit, descent of the precipitation core in the downdraft, and cyclonic wrapping of precipitation around the west and south edge of the mesocyclone to form a hook, are also present in the observations. Toutenhoofd and Klemp (1983) successfully simulate aspects of the circulation and precipitation field of a non-severe storm in Colorado. Klemp and Rotunno (1983) realistically simulate the wrapping of the precipitation hook around the maximum of mesocyclone vorticity, in agreement with observations by Garrett and Rockney (1962).

1.3 Continuity principles

An equation of continuity of a particular fluid characteristic expresses the conservation principle applicable to that characteristic. As one example, the familiar mass continuity equation states that mass can neither be created nor destroyed. The previously discussed numerical cloud models employ additional continuity relations for heat and the water substance. These are analogous to the mass continuity equation, although the effects of sources or sinks due to hydrometeor phase and size changes must additionally be accounted for. The relative motion of precipitating water substance with respect to the air must also be represented. Note that the classical conceptual models implicitly rely on these continuity principles - for example, vertical motion removes precipitation from the vault region at a rate which counterbalances the production of precipitation from cloud droplet coalescence. Careful reasoning suggests that if the wind field is

known, the fields of temperature and water substance can be derived from continuity principles. Kessler (1969) used continuity principles to study the distribution of water substance in relation to modelled one and two dimensional flows. Rutledge (1983) studied the dominant precipitation mechanisms in extra-tropical cyclone rainbands through the combined use of continuity principles, approximate representation of warm rain and ice microphysical processes, and 2-dimensional motions inferred from a single Doppler radar. The use of multiple Doppler derived airflow and continuity principles may provide a more realistic diagnosis of natural precipitation fields than is possible with approximate flow models, since the aforementioned conceptual and dynamical modelling studies have emphasized the impact of the detailed wind field.

1.4 Scope of research

The goal of this research is to analyze hydrometeor distributions and temperature and vapor fields within observed thunderstorms, relating them to thermodynamic, microphysical, and transportive forcing. The analysis method reported here proceeds from the storm motion observed by Doppler radar through accompanying models of thermodynamic and microphysical processes to diagnosis of internally consistent hydrometeor content and thermal fields. The relative importance of the forcing mechanisms are assessed. The goal is further addressed through study of spatial variations of derived fields. The analysis tool is a 3-dimensional diagnostic numerical model depicting variations of potential temperature, water vapor, cloud liquid water and ice, rain, ice and hail, by a system of equations expressing continuity of heat and water substance. Thermal and hydrometeor fields diagnosed by the current

model are verified with radar reflectivity and other available observations. Elements of the diagnosed fields are compared to the classical conceptual models discussed in this chapter.

The organization of the dissertation is now described. The mathematical model, the numerical analog, and the method of solution of the numerical model, are discussed in Chapter II. The results of preliminary tests using a warm cloud version of the model and input from a dynamically simulated cloud are presented in Chapter III. Chapter IV contains the results of two limited case studies of one weak and one strong convective storm, based on the input of Doppler derived winds and environmental soundings into the full warm/cold cloud model. Chapter V presents a summary and conclusions of the research along with proposals for ongoing research.

CHAPTER II

THE MODEL EQUATIONS

The principle analysis tool employed here is a warm/cold cloud numerical kinematic model based on continuity equations for heat and the water substance. The model is time-dependent, 3-dimensional, and incorporates thermodynamic and transportive processes, parameterized microphysics, and Doppler radar observations of velocity. The system of continuity equations depicts the variations of potential temperature (θ), water vapor mixing ratio q_v (gg^{-1}), cloud droplet total number concentration $N_c(cm^{-3})$ and mixing ratio $q_c(gg^{-1})$, rain drop total number concentration $N_r(cm^{-3})$ and mixing ratio $q_r(gg^{-1})$, hail mixing ratio $q_h(gg^{-1})$, ice mixing ratio $q_i(gg^{-1})$, and (non-precipitating) cloud ice mixing ratio $q_x(gg^{-1})$. The model domain corresponds to the Doppler radar observation domain.

2.1 The kinematic framework

The prognostic equations for θ, q_v, N_c, q_c, N_r, q_r, q_x, q_i and q_h may be effectively represented, following the notation of Klemp and Wilhelmson (1978), in the form

$$\frac{d\phi}{dt} = M_\phi + D_\phi , \tag{2.1}$$

where ϕ represents a generalized model variable, M_ϕ are microphysical source - sink rates, and D_ϕ are turbulent diffusion rates. The diffusion rates are defined later in this section while microphysical

processes are defined in the next section of this chapter. The operator $\frac{d}{dt}$ denotes the substantial derivative given in tensor form by

$$\frac{d}{dt} \equiv \frac{\partial}{\partial t} + u_j \frac{\partial}{\partial x_j},$$

where u_j are the u(west-east), v(north-south), and w (vertical) air motion components. The diffusion terms are approximated by the expression

$$D_\phi = \frac{\partial}{\partial x_j} \left(K_\phi \frac{\partial \phi}{\partial x_j} \right),$$

where K_ϕ is the eddy mixing coefficient. The value of K_ϕ is parameterized in terms of the spatially variable deformation of the velocity field (Smagorinsky, 1963). Following Takahashi (1981) and considering only deformation effects, the eddy mixing coefficient is written in expanded form as

$$K_\phi = c^2 \ell^2 Pr^{-1} \{ (\frac{\partial u}{\partial y} + \frac{\partial v}{\partial x})^2 + (\frac{\partial w}{\partial x} + \frac{\partial u}{\partial z})^2 + (\frac{\partial v}{\partial z} + \frac{\partial w}{\partial y})^2$$

$$+ 2[(\frac{\partial u}{\partial x})^2 + (\frac{\partial v}{\partial y})^2 + (\frac{\partial w}{\partial z})] \}^{1/2},$$

where c is a constant proportional to turbulence strength, $\ell = (\Delta x \, \Delta y \, \Delta z)^{1/3}$ is the appropriate length scale, and Pr is the eddy Prandtl number (typically in the range 1/3 to 1). Following Klemp and Wilhelmson (1978) in this study, Pr equals 1/3 and c equals 0.21. Additional mixing provided by a sub-unity value of the Prandtl number helps

to control the buildup of noise in the θ field during integration of the thermodynamic equation. Chapter III discusses a sensitivity test with K_ϕ equal to a specified constant. In the kinematic approach to solution of eq. (2.1), the u_j components appearing in the advection terms and in the turbulence parameterization are specified from Doppler observations.

2.2 The microphysical parameterization

A cloud model describes the distributions of the various hydrometeors in the particle size domain as well as in space and time, and relates the variations of the constituents to certain fundamental physical processes. A scheme that parsimoniously represents the water substance distribution and the various form and phase transitions taking place in the cloud, is termed a microphysical parameterization. In the alternative finite difference method, a discrete set of mass or size categories are used to approximate the continuous size distribution with the physical processes applied directly to each category. The parameterized scheme usually assumes a particular functional form of the continuous distribution, with the variation of the distribution being defined by the changes in power moments of the assumed distribution. The underlying physics is incorporated into the expressions for the power moment tendencies. For the set of moment tendency equations to be properly determined, the number of moment tendencies must equal the number of variable parameters in the assumed distribution function. The parameterization must balance the increase in physical resolution against the limitations of observational capabilities and computing resources. Observations and studies of natural precipitation events and

processes should be considered, to determine if simple and appropriate distribution models exist.

Numerous observations of cloud and rain have been reported in the literature. Squires (1958), Ryan et al. (1972) and others have associated high droplet concentration with small droplet size. Their results further show that continental cumulus droplet distributions tend to be characterized by a single concentration peak while maritime cumulus or stratiform cloud droplet distributions may have two peaks. Planck et al. (1980) document the dependence of raindrop size distribution on sampling time, finding that distributions tend toward a peaked or monodisperse shape for short sampling time and broadly conform to gamma distributions. The gamma function describes distributions with concentration peaks. The observations of Marshall and Palmer (1948) are long time averages, possibly explaining why they tend to be of inverse exponential form. These observations collectively suggest that a simple distribution function capable of explaining peaks in distributions, could provide an acceptable approximation to the forms of natural drop distributions.

Observations of hail and ice reported in the literature indicate that the distribution of these hydrometeors may be either inverse exponential or peaked. Federer and Waldvogel (1975) show that individual 30 s average hail distributions at the ground vary between inverse exponential and peaked shapes. The distributions may be broadened by differential advection. Ziegler et al. (1983) find clear evidence of hailstone distributions at the ground characterized by a single peak, although the inverse exponential and gamma functions each provide a good

fit to several of the 10-20 min samples. Ice crystal samples reported by Hobbs et al. (1974) are all distinctly peaked, while long time averaged snowflake distributions reported by Gunn and Marshall (1958) are of inverse exponential shape. Additional evidence in the literature indicates that an inverse exponential function appears to provide an acceptable fit to many natural hail and ice distributions.

Several theoretical and numerical studies of warm cloud coalescence have used functions capable of representing peaked cloud and rain distributions. Cotton (1972), Leighton and Rogers (1974), Berry and Reinhardt (1974a-d), and others have used a gamma function to specify the initial cloud droplet distribution for their numerical calculations of coalescence. Clark (1974) has developed a cloud phase parameterization assuming that cloud droplets are distributed according to a gamma function for all time. Clark (1976) has developed a warm cloud condensation-coalescence model in which the drop distribution is expressed in terms of a series of lognormal functions. His six parameter model produces simulated drop distributions in good agreement with the results of a highly resolved finite difference model. Williams and Wojtowicz (1982) have developed a cloud droplet distribution function in the form of a gamma function of droplet volume, which appears to provide a good fit to experimental data reported in the literature.

The minimum number of distribution parameters are determined by consideration of the fundamental microphysical processes and their effect on distribution moments. Each physical process considered here to be active in a convective cloud changes at least the total number concentration N and/or the mixing ratio Q of a particular specie,

although the radar reflectivity is primarily related to these two moments. For example, the accretion process of rain changes Q_r but not N_r, the self-collection of rain N_r but not Q_r, and drop freezing both N_r and Q_r. To represent the various physical processes adequately, we must maintain the independence of N and Q in the parameterized framework. This can be achieved by the inclusion of these or equivalent variable parameters in the assumed distribution function. Additional independent parameters may be added for better physical resolution, although their values may not be verifiable with observations.

With these observational and theoretical considerations in mind, the gamma function has been selected to represent model cloud and rain distributions, while the inverse exponential function represents the model hail and ice distributions. The functional form of the various distributions is assumed to be constant in space and time, so that only the distribution parameters vary. The gamma distribution used here has the form

$$n(v) = N[(\nu+1)^{\nu+1}(v/v_o)^{\nu}e^{-(\nu+1)v/v_o}]/\Gamma(\nu+1)v_o \quad , \tag{2.2}$$

where N is the total concentration (cm^{-3}), v_o is the mean volume (cm^3), ν is the shape parameter, v is volume, and n is the concentration per unit volume interval. Properties of the gamma distribution are shown in Appendix B. The inverse exponential function used here is of the form

$$n(D) = N_o e^{-\lambda D}, \tag{2.3}$$

where N_o is the intercept parameter, λ is the slope parameter, and D is diameter. Properties of the inverse exponential function for hail and ice are outlined in Appendices D.1 and E.1, respectively. The parameterization specifies ν in eq. (2.2) and N_o in eq. (2.3), and allows N, v_o, and λ to vary. This treatment is justified by the previously referenced observational and modelling studies. Additionally, Orville and Kopp (1977) fix the value of N_o in their hail model. Passarelli (1978) has assumed a snowflake distribution of the form of eq. (2.3), although his model allows N_o to vary in order to represent the aggregation process.

Fig. 2.1 illustrates the gamma distribution function for a cloud of varying mixing ratio and shape parameter with fixed total concentration. The horizontal axis shows drop radius (μm) on a log scale while the vertical axis indicates liquid water content per unit log radius on a linear scale. With this mapping, equal areas under the curves correspond to equal water contents. The dashed curves are droplet distributions with a shape parameter equal 3, while distributions having a shape parameter equal 0 are illustrated by solid curves. The clouds depicted in each panel have a concentration N = 1000 cm^{-3} which is typical of continental cumulus. The cloud in the left panel has a liquid water content L of 0.5 g m^{-3}, while the cloud in the right panel has a water content of 4.0 g m^{-3}. This eight-fold increase in liquid water content associates with a doubling of the radius of the mean volume (v_o) drop via the gamma distribution moment relation $Nv_o \propto L$ (Appendix B). This rightward shift of the droplet distribution in the size domain with increasing liquid water content reproduces the effects of condensation

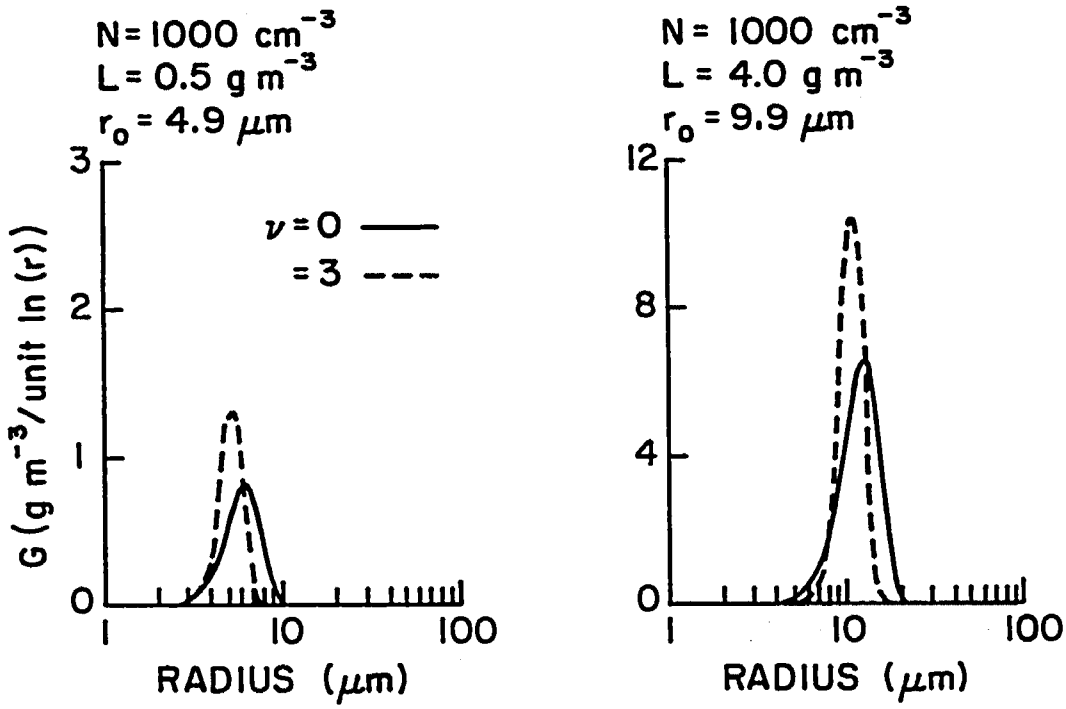

Fig. 2.1 Illustration of the gamma distribution function for a cloud of varying mixing ratio (L) and shape parameter (ν) with fixed total concentration (N). Liquid water content per unit log radius (G) is plotted versus droplet radius for gamma distributions with ν = 0 (solid line) and ν = 3 (dashed line). Pertinent distribution parameters are shown in the upper left corner of each panel.

growth in cloudy updraft air. The dispersion of mass about the mean radius droplet decreases with increasing shape parameter. As the tails of the distribution contract, the peak concentration increases to effectively conserve the area under the curve. With the increase of ν in the right panel, a decrease of standard deviation from 3.7 μm to 1.8 μm occurs (Appendix B).

The individual microphysical processes in the model source/sink terms M_ϕ in eq. (2.1), are listed in Table 1 along with the affected model dependent variables, symbols denoting each rate, the type and direction of associated phase transitions (if any) and location of each rate definition in the thesis. In the interest of continuity in reading, the detailed rate derivations are presented in the Appendices. Each rate is symbolized as in Table 1 to uniquely associate each rate expression in the Appendices with M_ϕ in the text. The warm cloud parameterization (cloud and rain) is reproduced in Appendix C, the hail parameterization in Appendix D, and the precipitating ice parameterization in Appendix E. Appendix F discusses the cloud ice sublimation parameterization. The necessary analytic integration techniques are shown in Appendix A. The microphysical processes M_ϕ are

$$M_\theta = \frac{L_v}{c_p\bar{\pi}}(R2 - R9) + \frac{L_s}{c_p\bar{\pi}}(-R26 - R33 - R34)$$

$$+ \frac{L_f}{c_p\bar{\pi}}(R11 + R15 + R17 + R22 + R23 + R25$$

$$- R20 - R28 + R32), \tag{2.4}$$

$$M_{q_v} = R9 + R26 + R33 + R34 - R2, \tag{2.5}$$

$$M_{N_c} = R1 - R3 - R6 - R14 - R16 - R24 - R31, \tag{2.6}$$

$$M_{q_c} = R2 - R5 - R7 - R15 - R17 - R22 - R23 - R25 - R32, \tag{2.7}$$

$$M_{N_r} = R4 + R12 + R19 + R27 - R8 - R10, \tag{2.8}$$

$$M_{q_r} = R5 + R7 + R13 + R20 + R28 - R9 - R11, \tag{2.9}$$

$$M_{q_h} = R15 + R17 + R18 + R21 + R29 - R20, \tag{2.10}$$

$$M_{q_i} = R22 + R23 + R25 + R30 - R26 - R28 - R29, \tag{2.11}$$

$$M_{q_x} = R32 - R33 - R34, \tag{2.12}$$

where L_v, L_f, and L_s are respectively the latent heat of vaporization, fusion, and sublimation, c_p is the specific heat of air at constant pressure, and the various rate terms are defined in this chapter or in the Appendices as indicated in Table 1. The Exner function π is defined by

$$\pi \equiv \left(\frac{p}{p_o}\right)^{\kappa} = \left(\frac{p}{p_o}\right)^{R/c_p},$$

where R is the gas constant for dry air, p is the air pressure, and p_o is a reference pressure. In this study p_o is set to 1000 mb . Overbars denote base state quantities.

Table 1.: The Microphysical Processes In brackets are listed each dependent variable affected by the specified microphysical process, followed by a symbol representing the corresponding rate expression appearing in the model equations. Variables are defined in the text.

Physical Process	{affected variable/rate symbol }	Phase Transition	Definition
cloud nucleation	{N_c/R1}	none	C.6, Text
cloud condensation/evaporation	{θ, q_v, q_c/R2}	vapor ↕ liquid	C.5, Text
cloud self-collection	{N_c/R3; N_r/R4; q_c, q_r/R5}	none	C.1
rain accretion of cloud	{N_c/R6; q_c, q_r/R7}	none	C.2
rain self-collection	{N_r/R8}	none	C.3,C,4
rain evaporation	{θ, q_v, q_r/R9}	vapor + liquid	C.7
rain freezing	{N_r/R10; θ, q_r, q_i/R11}	liquid + solid	E.2
rain sedimentation	{N_r/R12; q_r/R13}	none	Text
hail accretion of cloud (dry mode)	{N_c/R14; θ, q_c, q_h/R15}	liquid + solid	D.4
hail accretion of cloud (wet mode)	{N_c/R16; θ, q_c, q_h/R17}	liquid + solid	D.5
hail accretion of ice	{θ, q_i, q_h/R18}	none	D.7
hail melting	{N_r/R19; θ, q_r, q_h/R20 }	liquid + solid	D.6
hail sedimentation	{q_h/R21}	none	Text
ice nucleation	{θ, q_c, q_i/R22}	liquid[+vapor]+solid	E.3
ice deposition	{θ, q_c, q_i/R23}	liquid[+vapor]+solid	E.5
ice accretion of cloud	{N_c/R24; θ, q_c, q_i/R25}	liquid + solid	E.4
ice sublimation	{θ, q_v, q_i/R26}	vapor + solid	E.8
ice melting	{N_r/R27; θ, q_i, q_r/R28}	liquid + solid	E.7
ice-hail conversion	{q_i, q_h/R29}	none	E.6
ice sedimentation	{q_i/R30}	none	Text
cloud water freezing to cloud ice	{N_c/R31; θ, q_c, q_x/R32}	liquid + solid	Text
cloud ice sublimation	{θ, q_v, q_x/R33}	vapor + solid	F
cloud ice melting/evaporation	{θ, q_v, q_x/R34}	vapor +[liquid+]solid	Text

2.2.1 Condensation/evaporation adjustment

The condensation and evaporation processes represented by R2 involve a hybridization of the Soong and Ogura (1973) moist adjustment procedure with the gamma parameterization condensation growth process (Appendix C.5). The saturation ratio q_v/q_{vs} is computed after all variables have been advected and diffused, using Teten's formula in the linearized form (Klemp and Wilhelmson, 1978)

$$q_{vs} = \frac{3.8}{\bar{p}} \exp\left[17.27 \frac{\bar{\pi}\theta - 273}{\bar{\pi}\theta - 36}\right].$$

With supersaturation, the decrease in q_v (with attendent increases in θ and q_c) necessary to maintain exact saturation is computed. These adjustments are

$$q_v = q_v^* - r_l(q_v^* - q_{vs}^*) \tag{2.13}$$

$$\theta = \theta^* + \frac{L_v r_l}{c_p \bar{\pi}} (q_v^* - q_{vs}^*), \tag{2.14}$$

and

$$q_c = q_v^* + q_c^* - q_r, \tag{2.15}$$

where starred variables are quantities known prior to the adjustment step and

$$r_l = \left(1 + \frac{a(273-b)\,\bar{\pi}\, q_{vs}^*\, L_v}{(\bar{\pi}\theta^* - b)^2\, c_p \bar{\pi}}\right)^{-1}.$$

The parameters a and b are from Teten's formula for water saturation. In the event that cloud already exists, the gamma parameterization condensation rate is computed from eq.(C.5.6). The condensation rate R2 is then prescribed to be the minimum of the rate implied by eq. (2.13) and the explicit condensation rate. The principle advantage of this approximate adjustment scheme is that the constraint of exact saturation is relaxed. Supersaturation should be permitted in updraft regions, where intense scavenging reduces cloud to such a degree that it is incapable of consuming the excess vapor supplied to it. The evaporation of cloud is assumed to be instantaneous, and to be prescribed by eqs. (2.13 - 2.15) for saturated conditions. If cloud is consumed, rain evaporation may occur at the rate R9 (eq. C.7.1) if $q_v < q_{vs}$. If saturation deficit with respect to ice exists, ice sublimation may then occur at the rate R26 as determined by eq. E.8.1. The evaporation and sublimation adjustments are governed by equations analogous to eq. (2.13) and eq. (2.14) for cloud.

2.2.2 Cloud nucleation parameterization

Cloud nucleation (R1), described in Appendix C.6, depends upon the updraft strength (rate of supersaturation generation) and thermodynamic properties at cloud inflow boundaries, or the occurrence of supersaturation in the cloud interior via the condensation scheme. Concentration at inflow boundaries is determined from a power law relation with supersaturation, and an estimate of peak supersaturation due to Twomey (1959). The Alofs and Liu (1981) CCN distribution is used in most of the model tests, although sensitivity to reduced concentration is investigated. As a possible future model improvement, cloud nucleus

concentration could be added as a model dependent variable as in the warm cloud model of Silverman and Glass (1973). Nucleus conservation would improve the retrieval of cloud concentration in precipitation cores, but would have no appreciable effect on mixing ratios.

2.2.3 Warm rain coalescence parameterization

The warm rain coalescence parameterization features an analytic solution of the stochastic coalescence equation (SCE) using the gamma distribution and an accurate polynomial form of the collection kernel due to Long (1974). This test function approach to approximate the solution of the SCE is unique in the literature. The autoconversion parameterization of Cotton (1972) is useable in a Lagrangian reference frame only, while the current parameterization may be used in both Lagrangian and Eulerian frames because the rate expressions are functions only of local drop distribution properties in time and space. The underlying concept of the current parameterization is due to the cloud and warm rain coalescence models of Clark (1974, 1976, 1983). Clark's parameterizations allow the flexibility of an arbitrary collection kernel and multiple basis functions but require numerical quadrature to evaluate the coalescence integrals. Since the current treatment integrates the SCE, the corresponding solutions offer a simple and straightforward conception of the underlying physics of the coalescence process. The Clark parameterization probably has greater physical resolution than the scheme developed here. The form of the current parameterization is similar to the warm cloud coalescence parameterization of Berry and Reinhardt (1974d). However, their rate coefficents are approximations to integrals and require significant calculation to

evaluate while the coefficients in the current parameterization are prespecified constants. The concepts of cloud droplet self collection, rain collection of cloud, and rain self-collection due to Berry and Reinhardt (1974a) are used here. A new technique for parameterizing drop breakup is introduced, which involves reducing the large hydrometeor self-collection rate coefficient according to the coalescence efficiency for filament breakup (Brazier-Smith et al., 1973; Low and List, 1982).

The realism of the warm rain coalescence parameterization is illustrated by comparing the outputs of the Lagrangian form of the parameterized model and a highly resolved finite difference coalescence model. The verification tests include the effects of coalescence and coalesence/breakup separately. To initiate the parameterized model, a cloudy, rain-free parcel is described for specified liquid water content, mean cloud droplet size, and distribution shape parameter. These conditions are identical to the initial conditions of the finite difference model integrations of Berry and Reinhardt (1974b), and integrations of the parameterized model are compared with their results as reproduced from that paper. Since these comparisons are qualitative in nature, the parameterization is probably not optimal. Clark (1983) claims optimal results based on extensive testing of his lognormal model. Tuning experiments with the lognormal model reveal that increasing the accuracy of mixing ratio in individual categories results in decreasing the accuracy of individual concentration and vice versa. By stressing the distribution moments in the current parameterization, a similar degradation in accuracy of individual concentrations is effectively obtained.

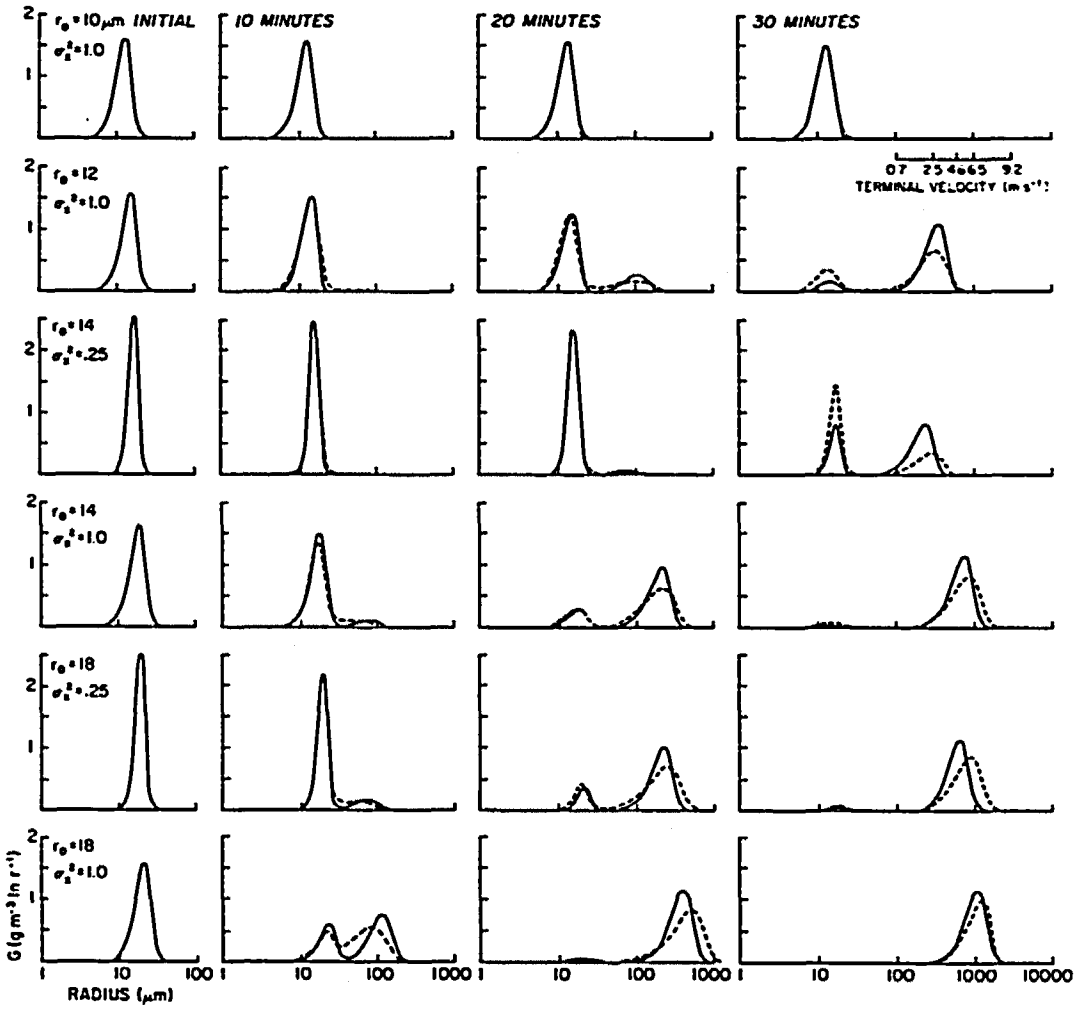

Fig. 2.2 Comparisons of results of parameterized and finite-difference warm cloud coalescence model integrations. Liquid water content per unit log radius versus drop radius, is shown by a solid curve for parameterized model output and a dashed curve for finite-difference model output. The curves coincide in some areas. The first column shows initial cloud conditions, while successive columns from left to right illustrate the evolving cloud droplet and rain drop distributions at 10 minute intervals. Each row corresponds to different initial cloud conditions, with mean radius and variance indicated in the upper left corner of each initial condition panel. Drop terminal fallspeed is indicated below the upper right panel. Finite difference model results are adopted from Berry and Reinhardt (1974b).

The model moment equations describing cloud autoconversion, rain accretion of cloud, and rain self-collection (Appendices C.1-3) are integrated forward in time to determine the evolution of the cloud and rain drop distributions. The parcel is assumed to be closed, so that neither condensation growth nor hydrometeor fallout and evaporation are treated here. The coalescence efficiency is set to unity in these tests, although collisional breakup is represented in the full parameterization. In order to match the Berry-Reinhardt model integration, the parameterized model integrations assume an initial 1 g m^{-3} liquid water content with six different combinations of initial mean droplet radius (range of 10-18μm) and cloud shape parameter (value 0 or 3). Results of these model integrations along with initial cloud conditions, are illustrated in Fig. 2.2. Each row of four plots corresponds respectively to the initial cloud condition and the subsequent cloud and rain distributions at 10 min intervals in the integration. The solid curve in each panel represents the parameterized distribution, while the dashed line denotes the finite difference model solution. At the base of the last panel of Fig. 2.2, rain drop terminal fallspeeds are indicated as a function of size. The horizontal axis shows drop radius (μm) on a log scale while the vertical axis indicates liquid water content per unit log radius on a linear scale. The general pattern during coalescence is for autoconversion and accretion to transfer water from cloud to rain, with the drop self-collection causing the rain peak to shift to the right with time in the absence of water transfer[1]. The

[1]In this regard, Clark describes the gamma distribution function as a "movable" basis function.

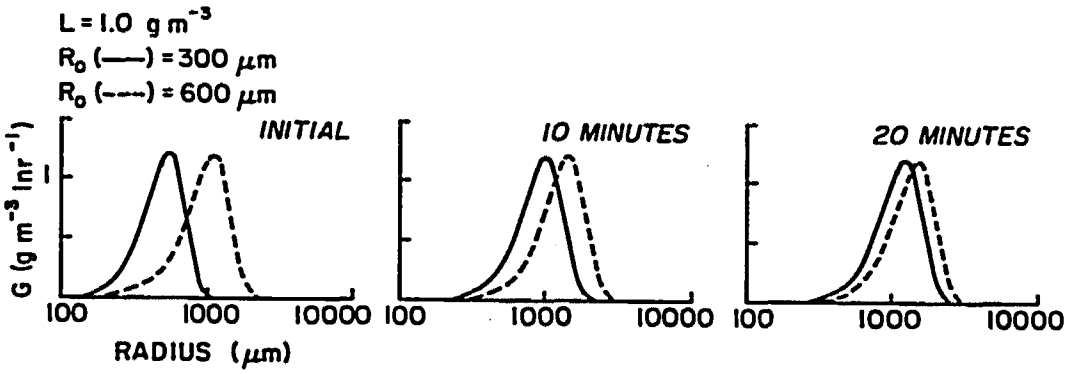

Fig. 2.3 Comparisons of time evolution of two different drop distributions at 10 minute intervals in the parameterized model. Both distributions are acted on by self-collection/breakup only. Liquid water content and initial mean volume radius are indicated at upper left. Graphical scheme is the same as in Fig. 2.1.

timing of rain formation, as judged by the position of and area under the rain distribution at 30 min of integration, seems to be well represented. While particular distributions at specific times exhibit noticeable differences in regard to rain water content at a given radius, the total rain water contents appear to be in good agreement. Errors in mean drop fallspeed appear to be less than or of order 1 ms^{-1} based on the separation of parameterized and finite difference rain peaks at 30 min. This error is less than 10% of typical peak updrafts, which exceed 10 ms^{-1}. The great sensitivity of drop distribution evolution to the position of the cloud distribution is clearly evident. Since bulk parameterizations of autoconversion do not include the modulating effects of droplet size, their ability to adequately represent the physics of cloud conversion would seem to be seriously limited.

2.2.4 Collisional breakup parameterization

The breakup parameterization limits the difference in the location of the rain peak between the full warm cloud model (Appendix C.4) and the finite category model. This parameterization provides an (asymptotically approached) upper limit on drop size. Breakup decelerates the rightward propagation of the drop distribution in the radius domain with increasing mean diameter beyond 600 μm, as demonstrated in Fig. 2.3. In this simulation, two drop distributions having initial mean diameters of 600 and 1200 μm and liquid water contents of 1 g m^{-3}, are both acted on by self-collection and breakup. The initial separation of the peaks decays in about 10 min in this case. The implication of this test result for the full coalescence model is that rain distribution position errors due to false resolution of the

coalescence process have diminishing impact in time as collisional breakup opposes drop self-collection.

2.2.5 Hail parameterization

The hail parameterization features expanded representations of dry and wet hail growth. Utilizing the threshold diameter for the onset of wet growth from Lagrangian hail growth theory, the total hail distribution is subdivided into two parts that are characterized by dry or wet growth. The approximate effects of low density riming on the dry growth rate are included. Pflaum (1980) has argued that such effects may play an important role in hail formation and growth. This treatment contrasts with the hail parameterization of Orville and Kopp (1977), who compute dry and wet bulk accretion rates for the entire distribution and use the smaller of the two rates to vary hail mixing ratio. They also assume a constant ice density of 0.9 g cm^{-3} in their riming calculations, which may overestimate terminal fallspeed and the collection kernel for dry growth. Hail accretion of rain is neglected compared to hail accretion of cloud because the collection kernel of mean diameter cloud droplets and hail particles is much larger than the kernel for typical mean diameter hail particles and rain drops. Drop concentrations are reduced to negligible values by freezing, while small cloud droplets typically have much higher concentrations. This enhances the relative importance of hail accretion of cloud.

2.2.6 Ice parameterization

A key feature in the ice parameterization is the representation of the process whereby ice particles, growing by vapor diffusion and riming of cloud water, become large enough to serve as hail embryos. In the

ice-hail conversion process (R29), the amount of ice mass residing in the ice distribution at diameters exceeding an assumed minimum embryo size is transferred to the hail distribution[1]. Based on the typical observation that rain and ice crystal distributions have similar shapes and intercept parameters while hail distributions are typically much flatter[2], frozen rain drops are associated with the ice distribution. This averts the strong probability of a positive feedback between rain and ice/hail mixing ratios across the freezing level, due to the inverse relationship between mean hydrometeor fallspeed and intercept parameter (Appendix D.1). Variations of ice particle growth rates due to mixing of spherical and crystalline geometry is not considered. The ice parameterization does not explicitly treat individual ice crystal habits. The deposition growth parameterization is based on an expression of individual growth rate as a function of temperature and crystal habit (assumed temperature dependent also).

The rate computations to be reported in Chapter IV indicate that deposition growth and cloud riming are among the more important ice processes. Retrieval error may be largely due to the absence of explicit crystal habits in the ice parameterization. Since the deposition growth parameterization already includes the effect of variation of crystal shape with temperature, attention may be further restricted to

---

[1]This treatment implicitly redistributes the mass of large ice particles to all diameters from zero to infinity. A more internally consistent treatment might be to model ice and hail as adjoining inverse exponential distributions truncated at the threshold size, so that converted ice mass resides in particles with diameters exceeding the threshold only.

[2]Observed hail and rain distributions have a three order of magnitude difference in intercept parameter.

the accretion process. The assumed collection efficiency is questionable because it represents the average for an ensemble of ice habits and sizes. A sensitivity test featuring variation of ice collection efficiency is presented in Chapter IV. Sensitivity tests are needed to assess the impact of error in a given term because the model is nonlinear. If a very specialized microphysics investigation requires explicit habit information, the model can be expanded to include the additional detail.

2.2.7 Cloud ice parameterization

Small cloud ice particles form by the freezing of cloud water at or below -40°C. The spontaneous freezing of cloud water to cloud ice is represented via the rates R31 and R32, wherein all cloud mass is transferred to non-precipitating ice and cloud number concentration is set to zero. Sublimation of cloud ice (R33, Appendix F) occurs only at sub-ice saturation and follows the evaluation of ice sublimation. Cloud ice is assumed to instantaneously melt at or above freezing and evaporate in an environment sub-saturated with respect to water (R34).

2.2.8 Hydrometer sedimentation

The sedimentation rates for rain (R12, R13), hail (R21), and ice (R30) are all of the form

$$(M_\phi)_{sedi} = \frac{1}{\bar{\rho}} \frac{\partial}{\partial z} (\bar{\rho} \bar{V} \phi), \tag{2.16}$$

where V is the appropriate mean terminal fallspeed, the rate R12 corresponds to N_r, R13 to q_r, R21 to q_h, R30 to q_i, and ϕ represents one of these four variables. Rain terminal fallspeed is defined by eqs. (B.5) and (B.6), hail terminal fallspeed by eq. (D.1.3), and ice terminal fallspeed by eq. (E.1.3). Although size-sorting effects are not taken into account, the resulting error in the flux divergence expressed by eq. (2.16) is minimized by the use of fallspeeds associated with the center of concentration and mass of hydrometeor distributions.

2.3 The numerical framework

The system of continuity equations follows the form of eq. (2.1) and is solved numerically, after being represented in finite-difference form. After extensive experimentation using various numerical approximations, the second-order leapfrog time and fourth-order space differencing scheme used by Klemp and Wilhelmson (1978) has been adopted. Forward-upstream and forward-quasi-Lagrangian schemes were also tried, but these were undesirable due to computational damping and truncation errors in the numerical solutions. An unstaggered mesh system is employed here because only advection and diffusion terms are being evaluated. Use of the leapfrog scheme requires the storage of two time levels of each dependent variable, however this scheme does not have computational damping. Second-order space differences are used in the vertical, with fourth-order differencing in the horizontal.

Following Lilly (1965), the various time and space differencing operators are all of the form

$$\delta_{n\xi}\phi(\xi) = \frac{1}{n\Delta\xi}\left[\phi(\xi + n\Delta\xi/2) - \phi(\xi - n\Delta\xi/2)\right] ,$$

where ϕ denotes the dependent variable, ξ the independent variable, and $n\Delta\xi$ is the interval over which the operation takes place.

The finite-difference representation of eq. (2.1) for all dependent variables takes the form

$$\delta_{2t}\phi = -\frac{1}{3}u\,(4\delta_{2x}\phi-\delta_{4x}\phi) - \frac{1}{3}v(4\delta_{2y}\phi-\delta_{4y}\phi) - w\delta_{2z}\phi + M_\phi + D_\phi,$$

where ϕ is a dependent variable. In sensitivity tests using the Wilhelmson-Klemp proxy data set reported in the next chapter, the grid mesh is vertically staggered. The vertical advection term is there expressed as a vertical average of centered approximations over one grid interval. The diffusion terms D_ϕ are represented by

$$D_\phi = \delta_x(K_\phi\delta_x\phi) + \delta_y(K_\phi\delta_y\phi) + \delta_z(K_\phi\delta_z\phi),$$

and are evaluated at time $t-\Delta t$ to maintain stability in the leapfrog scheme. Time and space increments and the diffusion coefficient must satisfy the well-known condition $\Delta t \leq \text{MIN}\,[\Delta x/c,\ \Delta x^2/8K]$, for centered differences. The microphysical terms M_ϕ are evaluated in a semi-implicit fashion, following from advected and diffused values of the dependent variables. This treatment is used by Blottner (1970) in the marching solution of boundary layer equations for high speed flow. As also pointed out by Roache (1972), the so-called "stiff" or zero-order terms may dominate the computational stability of the finite-difference equations. The evaluation of the stiff terms semi-implicitly at time $t+\Delta t$ appears to mitigate potential instability problems.

At the lateral, upper and lower boundaries, an insulated inflow condition is adopted. An upwind difference outflow condition lagged to t-Δt maintains stability. Horizontal advection is evaluated with second-order centered space differences at all gridpoints one grid interval in from the lateral boundaries. Hail and ice are permitted to sediment at the upper boundary by assuming a computational mixing ratio value of zero one grid interval above the upper boundary, and obtaining a simple upwind convective derivative form for eq.(2.16). The normal component of the boundary mixing terms is set to zero[1].

All dependent variables are temporally smoothed with the Robert (1966) low-pass filter to suppress any tendency for time splitting of the leapfrog solution that may arise. Following Klemp and Wilhelmson, the filter is applied at every time step with the filter coefficient α set to 0.1. Temporal filtering must follow the evaluation of M_ϕ to maintain condensation adjustments. A fourth-order low-pass space filter of the form

$$\phi_j^{n+1} = \phi_j^{n-1} - \frac{2K_D\Delta t}{\Delta x^4}(\phi_{j+2}^{n-1} - 4\phi_{j+1}^{n-1} + 6\phi_j^{n-1} - 4\phi_{j-1}^{n-1} + \phi_{j-2}^{n-1})$$

is applied to all dependent variables to control the amplification of high frequency modes. This filter is applied at every time step with the diffusion terms. Here Δx is the grid spacing, Δt is the time step and K_D is a filtering coefficient whose value is determined

[1]A more satisfying treatment would be to extend the analysis/computational domain above the cloud top. A potential drawback of this approach is that Doppler data is probably not available near the cloud top.

experimentally. With the fourth-order filter applied both in the horizontal and vertical, an appropriate value of K_D is 2.0×10^9. It was found necessary to apply the filter in three dimensions in observed deep convective storms due to the intensity of the natural circulations and the coarse resolution of the Doppler analysis. Filtering damps noise wave components in the solution and mitigates the effects of shocks of possible spurious origin in the wind field. Stability considerations require that the filtering coefficient satisfy the relation $K_D \leq \Delta x^4/32\Delta t$, and less than 50% of this value is typically used to adjust for the effect of applying the filter in three dimensions.

2.4 Model solution

The finite-difference form of the model is integrated forward in time from a specified initial state to produce the solution fields of temperature and water substance. The model continuity equations are prognostic in the dependent variables whose diagnosis is sought. This situation contrasts with the dynamic retrieval method wherein the momentum equations are diagnostic in π and θ and prognostic only in momentum. Time-spaced Doppler observations allow specification of the local derivatives, and a purely diagnostic set of equations is obtained in that case.

Solution of the present problem effectively requires a diagnosis of the initial condition. There are three alternatives: insert time-spaced wind analyses into the model during time integration from the initiating cumulus stage through the complete life cycle of a storm, hold the storm-relative wind field (at a suitable intermediate stage of convection) constant during integration to a steady state (identifying the

steady solution with the wind field at that instant in time), or initiation of the former procedure with the latter procedure. In the final case, errors from the initial condition would propagate into the solution as integration proceeds. This error is due to possible storm-relative non-steadiness and a non-optimal choice of Galilean transformation.[1] Since wind data covering the entire life span of an individual convective storm are currently unavailable, the first method cannot be employed in this research. To limit the scope of this study, the steady approximation is adopted in the current research. An obvious course of future research is the insertion of time-spaced wind analyses to study transients in the model solution. The retrieval scheme should initially be tested in a relatively simple conceptual framework.

There is justification for employing the steady approximation from the results of this research. Extensive model testing and the evaluation of the relative magnitudes of model terms (to be discussed in Chapter III) provides conclusive evidence that the model local derivative terms are small compared with the remaining diagnostic terms within a typical convective cell. In modelling mature clouds where the warm cloud accretion process is very strong, the time scale associated with accretion is much shorter than the time scale of a typical convective cell ($\gtrsim$ 30 min). This point is illustrated as follows; consider a simple warm cloud accretion model wherein the scavenging of cloud is proportional to the product of cloud and hydrometeor mixing ratio

---

[1] A unique Galilean transformation yielding zero advection error does not exist in the case of a multi-cell storm with distinct cell velocities, even if each cell is steady with respect to it's own motion.

(Kessler, 1969; Klemp and Wilhelmson, 1978a). The decay time[1] associated with this process is the inverse of the dimensionless hydrometeor mixing ratio. Based on Z-q relationships applied to typical core reflectivities exceeding 55 dBZ, hydrometeor mixing ratios of order 10 g kg^{-1} are possible. The accretion time scale (inverse decay time) in this case is 10^2 s, a negligible value compared with the convective time scale. Even at some distance from the core where mixing ratios are of order 1 g kg^{-1}, the accretion time scale is still relatively small. In the case of precipitating ice, the accretion time scale increases to order 10^3 s (Heymsfield and Musil, 1982) due to decreased collection efficiency and fallspeed.

A radically different situation is anticipated in cells undergoing transition from the congestus to mature stage. As the initially echo-free cloud gradually fills with hydrometeors, the accretion process becomes strong and will produce an imbalance in the continuity equations. In transition stages of convective cloud development, time-spaced wind analyses should be used to integrate the model from the initial quasi-adiabatic cumulus stage through such nonsteady periods of development. The model *per se* is fully capable of accurate retrieval during unsteady development phases. The choice of a steady state approximation is made purely for convenience.

---

[1]The decay time is that period associated with the decrease of cloud content to e^{-1} times the initial value.

CHAPTER III

KINEMATIC MODEL VERIFICATION TESTS

The kinematic model has been tested against the output of the dynamic model of Klemp and Wilhelmson (1978), hereafter referred to as model D. The test approach is to retrieve temperature and mixing ratio fields with the kinematic model (hereafter referred to as model K) using the wind field generated by model D, and to subsequently verify model K output with the corresponding model D thermal and microphysical fields. Models K and D use identical bulk warm cloud parameterizations (Kessler, 1969) and exclude the ice phase. The wind field steadiness assumption, which may ultimately be necessary in order to permit diagnosis with the time dependent model K continuity equations, is probably the most serious of the model K approximations and must be evaluated before the kinematic method can be applied to real data with confidence. Other sensitivity tests, such as the effect of a random wind field error on retrieved fields, are also included.

3.1 Experimental procedure

The experimental procedure consists of: i) the initialization of the model K fields of θ, q_v, q_c and q_r, ii) the insertion of the model D storm-relative output wind field[1] into model K (subsequently held constant) and iii) integration of the time-dependent model K equations. The steady state is here subjectively defined by a one time step mixing

[1]Cell propagation vector given in Wilhelmson and Klemp (1978).

ratio change less than 0.01 g kg^{-1}. The model K and D continuity equations are identical in their continuous and discrete formulations, with the lone exception that model K turbulent diffusion coefficients are computed from the wind field deformation only. Differences between retrieved and model D output fields will likely arise purely from integration of model K to a steady state.[1] To obtain physical insight into the relative importance of the local derivative and hence the cause of possible retrieval errors, the model D thermal and microphysical rates are computed term-by-term (including the local derivative). The particular cloud simulation used here is reported by Wilhelmson and Klemp (1978). Dynamic temperature retrieval experiments using this data set as input have been conducted by Hane et al. (1981). The model D fields represent the culmination of 90 min of simulated storm evolution, at which point the simulated cell is approaching a steady state.

3.2 Results of retrieval experiments

Four retrieval experiments have been conducted, namely the control experiment (C) as previously outlined and three sensitivity tests. These tests involve: i) the addition of gaussian white noise (σ = 1 ms^{-1}) to each wind component (experiment N), ii) the varying of the initial condition from an updraft saturated at the environmental temperature (exp. C) to the stratification of the q_v field according to the environmental profile (experiment I), and iii) the fixing of the

[1]The model equations are fully time-dependent, but the steadiness assumption effectively cancels the local derivatives.

turbulent diffusion coefficient value at 100 $m^2 s^{-1}$ (experiment T).[1] Test results are illustrated by selected horizontal and vertical cross-sections through the model D/K domain of proxy and retrieved fields as well as error fields. Horizontally averaged error statistics for each variable and each test are computed based on stratified samples from the updraft region and from the rain/weak updraft region only.

The error analysis will concentrate on experiments C and N. Based on the results of experiment I and from theoretical considerations, it is concluded that the steady state solution of model K is insensitive to the particular choice of initial condition. Experiment T demonstrates that the solution is not generally sensitive to turbulence strength, although physically realistic levels of turbulent dissipation should be included to control the buildup of high frequency noise during model integration. Although error statistics for all tests will be discussed, display of plotted fields is restricted to the results of experiments C and N only.

Kinematic model output, the known model D fields and difference fields for experiment C are displayed by selected vertical cross-sections in Figs. 3.1 - 3.4. Figs. 3.1 and 3.4 are oriented south-north through the updraft core, while Figs. 3.2 and 3.3 are oriented west-east through the updraft core. Fig. 3.1a-c depicts potential temperature deviation from the environment (°C) as retrieved by the kinematic model (a) and as output from the dynamic model (b), as well as retrieved minus known temperature (c). The contour interval is 0.5 degrees. Retrieved

---

[1] Typical values of K_d in the cloud exceed 1000 $m^2 s^{-1}$, hence the diffusion terms are effectively "turned off" in experiment T.

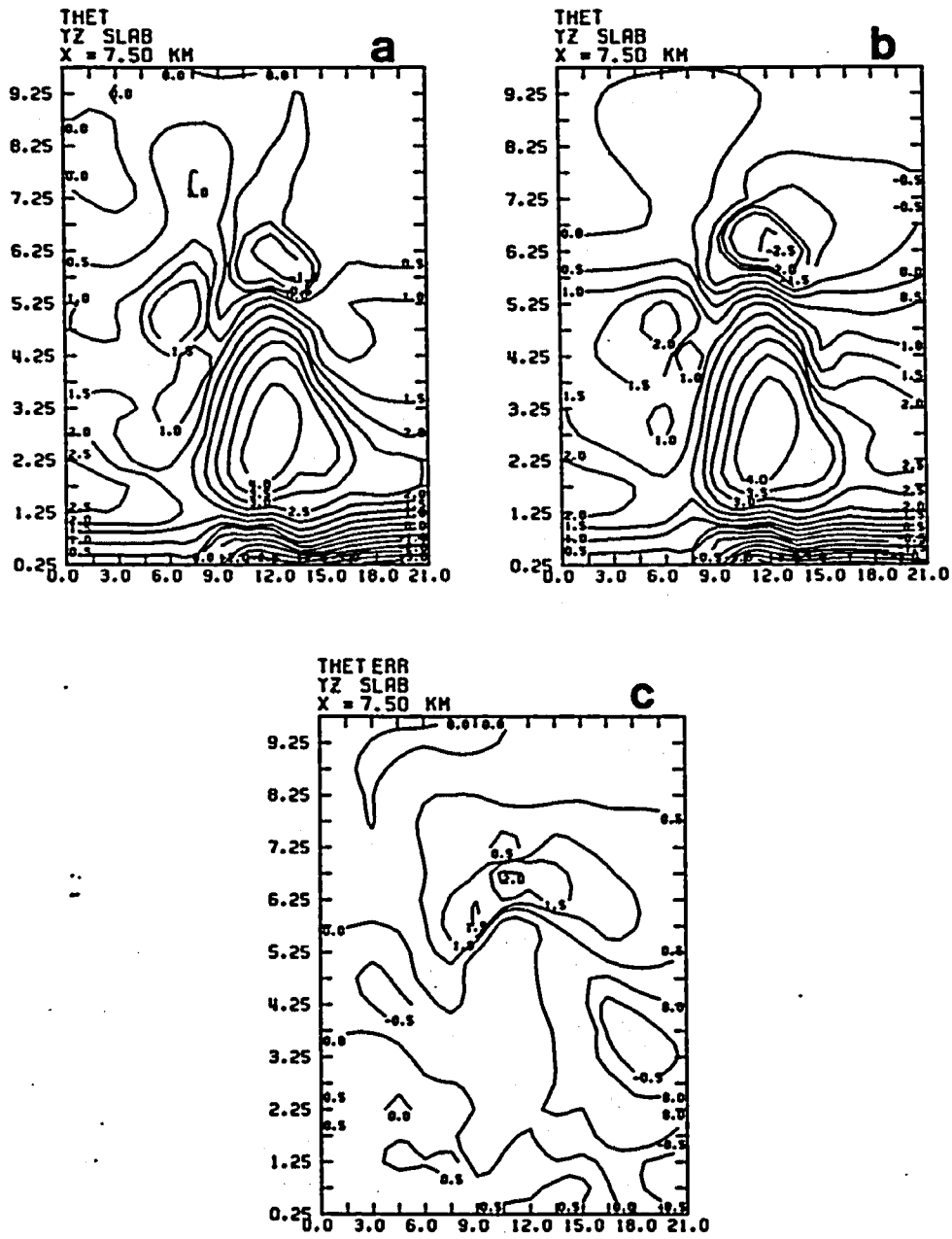

Fig. 3.1 Experiment C south-north oriented vertical cross-sections in the cloud core showing deviation potential temperature (°C) of kinematic model (a), with known field (b) and the difference field (c) obtained by subtracting panel (b) from panel (a). Contour interval is 0.5 deg.

temperatures are quantitatively very close to known temperatures, with errors in the middle levels of the warm core less than 0.1 degrees. At 6.75 km (above the cloud top) where errors are locally large, a temperature defect is correctly retrieved. The characteristic warm middle level and cold upper level thermal structure of the deep moist updraft is physically due to the maintenance of moist adiabatic properties related to the environmental stratification. Cloud top temporal fluctuations may explain the retrieval inaccuracies at that level. By the 90 min time of the model D integration, the leading edge of the cold air outflow has passed through the lateral boundaries of the computational domain, thus permitting a fairly accurate retrieval with the steady solution.

Fig. 3.2a-c depicts water vapor mixing ratio (g kg^{-1}) as retrieved by model K (a) and output from model D (b), as well as the difference field (c). As in the case of retrieved temperature, water vapor errors are very small within the saturated updraft core, manifested here by an upthrust of the environmental moisture stratification. Errors are locally large above cloud tops and within the middle levels of the clear environment on the west flank of the cloud. Note that the unsaturated, precipitation-free environment conserves moisture and entropy following the local air motion and indeed does not satisfy a steady model.[1] The model K domain is nested within the model D grid and encloses the cloud core only, so that the model K lateral boundary conditions do not

[1]Local changes are compensated only by advection.

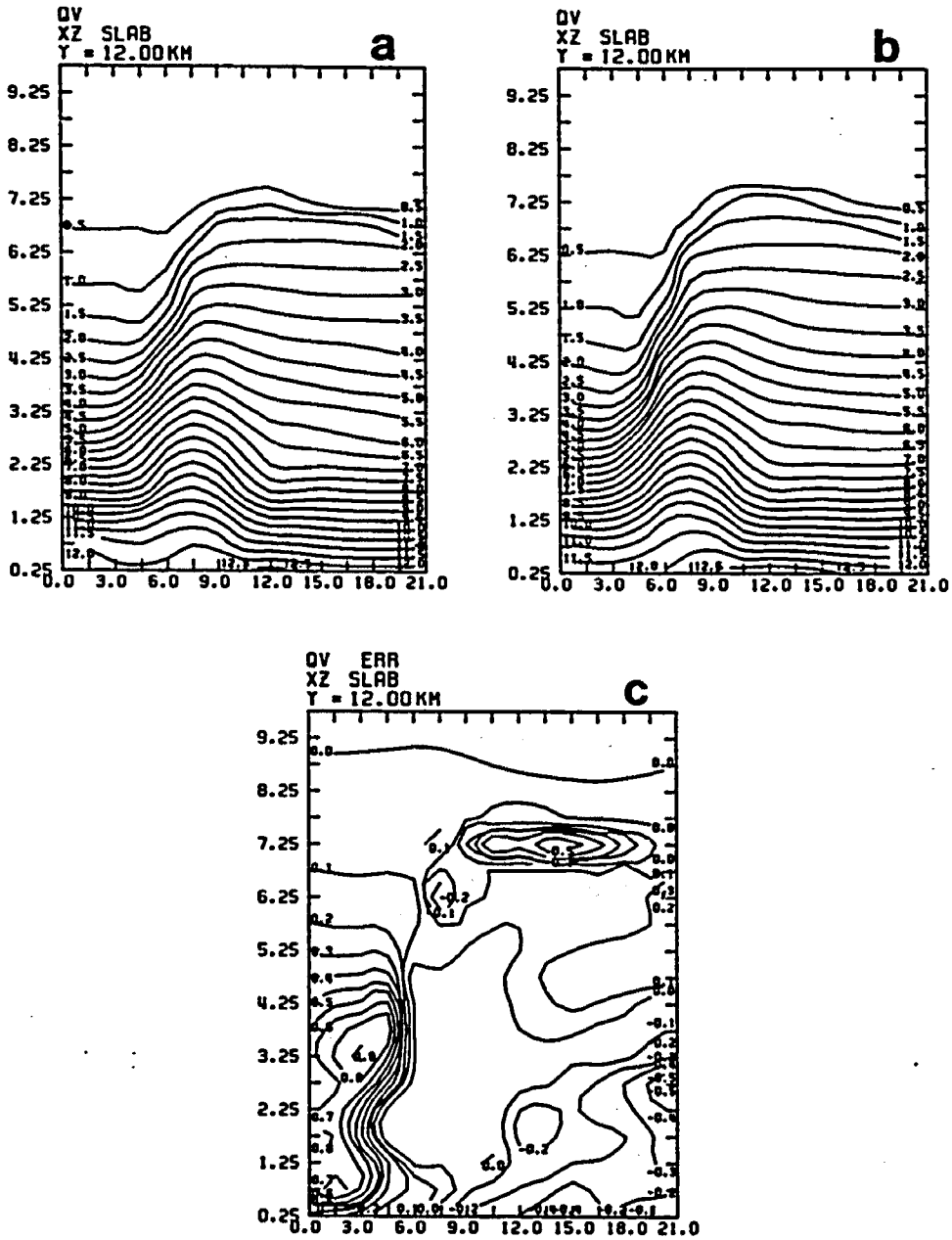

Fig. 3.2 Same as in Fig. 3.1, but for water vapor mixing ratio (g kg^{-1}) in a vertical west-east cross-section. Contour interval in panels (a) and (b) is 0.5 g kg^{-1}, and in panel (c) 0.1 g kg^{-1}.

adequately represent the storm environment as defined by the model D output.

Cloud mixing ratios (g kg^{-1}) from the retrieval (a) and model D output data (b) as well as the difference field (c), are shown in Fig. 3.3. The general character of the cloudy updraft/anvil region is well reproduced in the retrieved fields. The leading edge of the anvil has passed through the lateral boundaries, permitting a meaningful steady solution. Errors on the downstream end of the anvil top may be due to local non-steadiness.

Fig. 3.4a-c depicts rain water mixing ratio (g kg^{-1}) from the retrieval (a) and model D output (b) data, as well as the difference field (c). Orientation of the precipitation core as well as extreme values are well reproduced, although a constriction of the retrieved rain area in the vertical is manifested by negative error at upper levels and positive error in middle levels. This results in a decrease in middle level cloud via accretion, and increases the low level precipitation content via sedimentation. It should be noted that the peak updraft decreases from 14.5 ms^{-1} to 12.1 ms^{-1} in the 10 min prior to the proxy data, and would produce an imbalance between vertical advection and sedimentation above the level of maximum rain content. Errors are on the order of 10% within the rain core, so that the effects of possible non-steadiness within the cloud core appear to be rather limited.

The effects of adding gaussian white noise to the wind fields prior to retrieval, are illustrated by vertical cross-sections in Figs. 3.5 (same as Fig. 3.1) and 3.6 (same as Fig. 3.4). While both the temperature (Fig. 3.5) and rain water (Fig. 3.6) fields display small scale

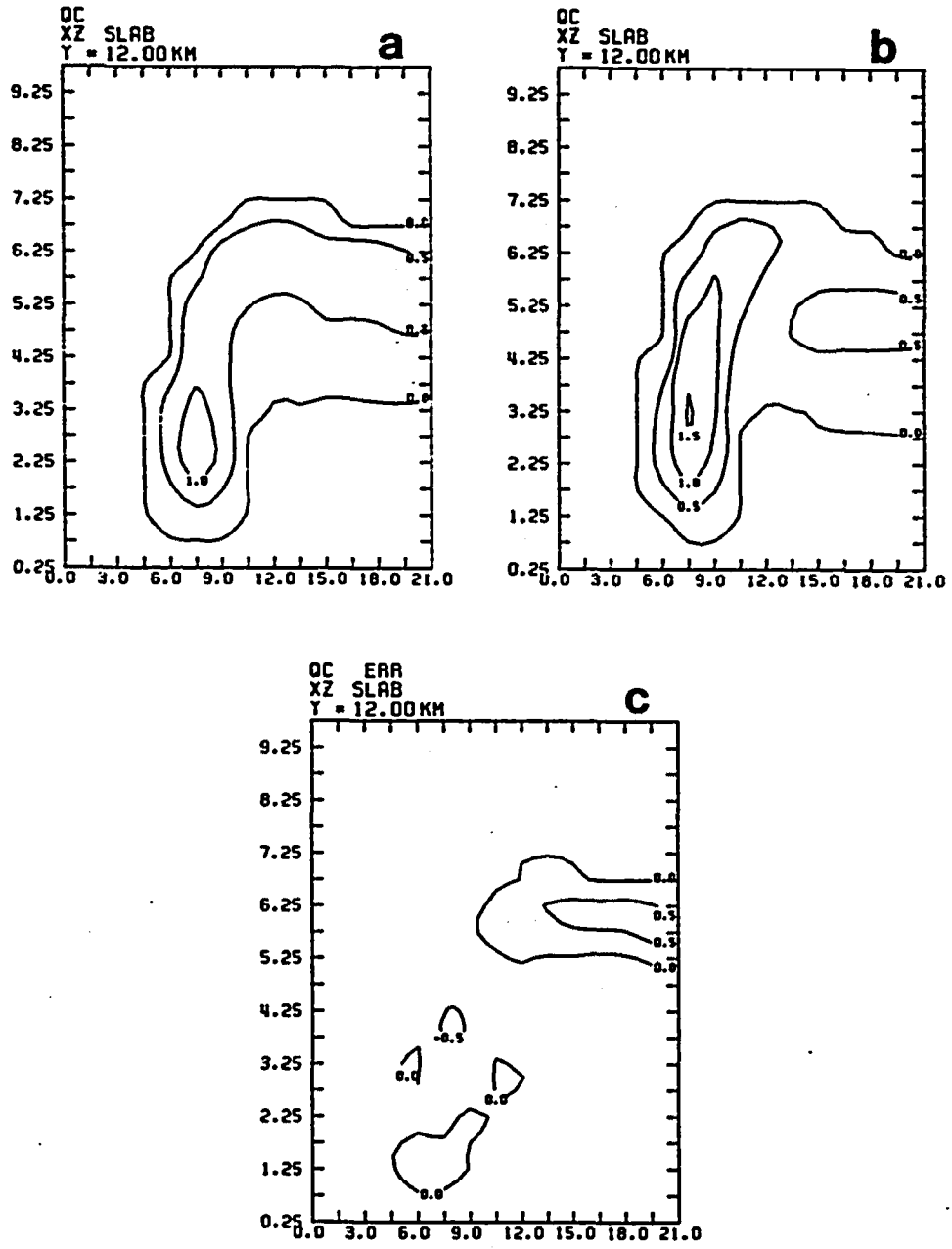

Fig. 3.3 Same as in Fig. 3.2, but for cloud water mixing ratio (g kg^{-1}). Contour interval is 0.5 g kg^{-1}.

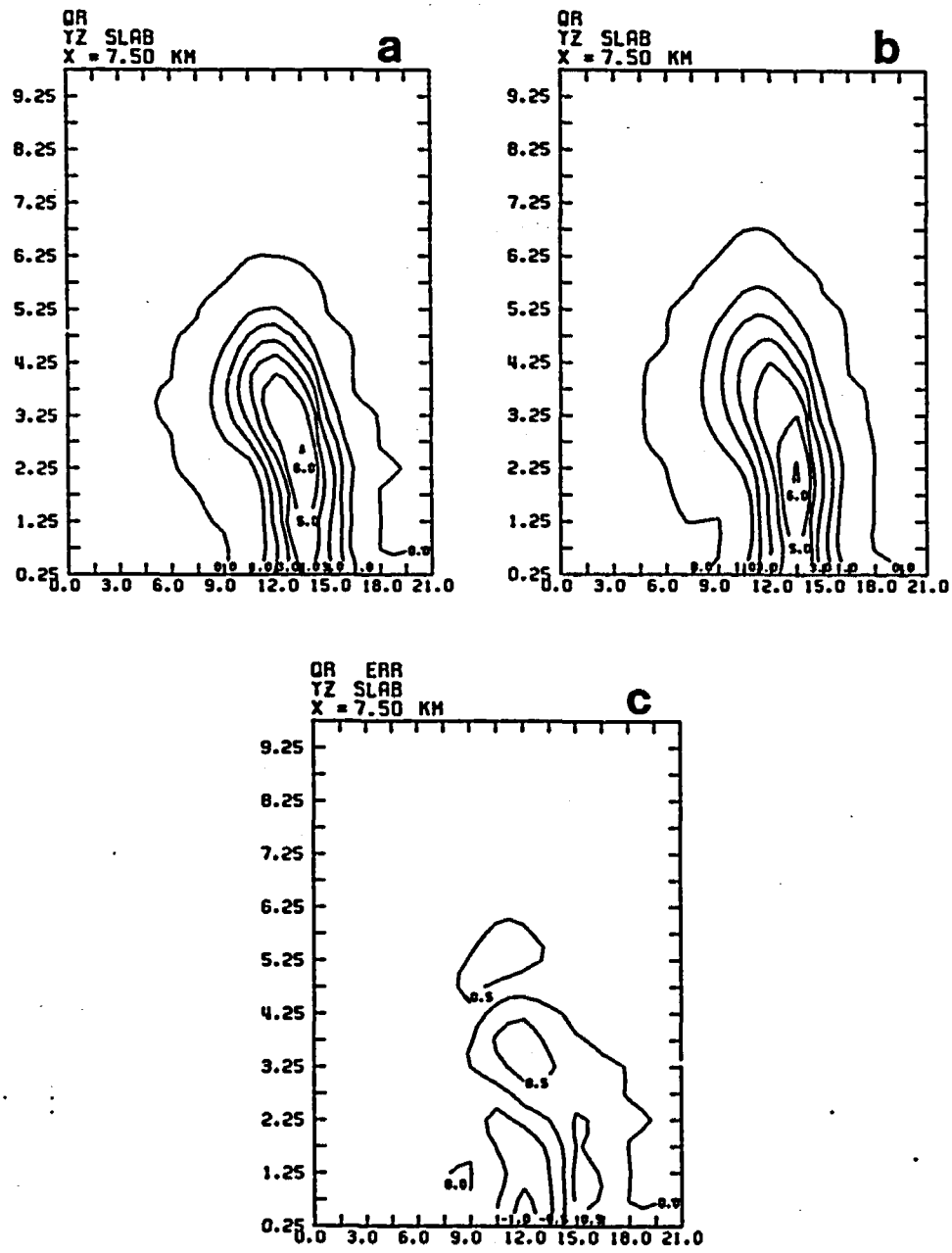

Fig. 3.4 Same as in Fig. 3.1, but for rain water mixing ratio ($g\ kg^{-1}$). Contour interval in panels (a) and (b) is 1 g kg^{-1}, and in panel (c) 0.5 g kg^{-1}.

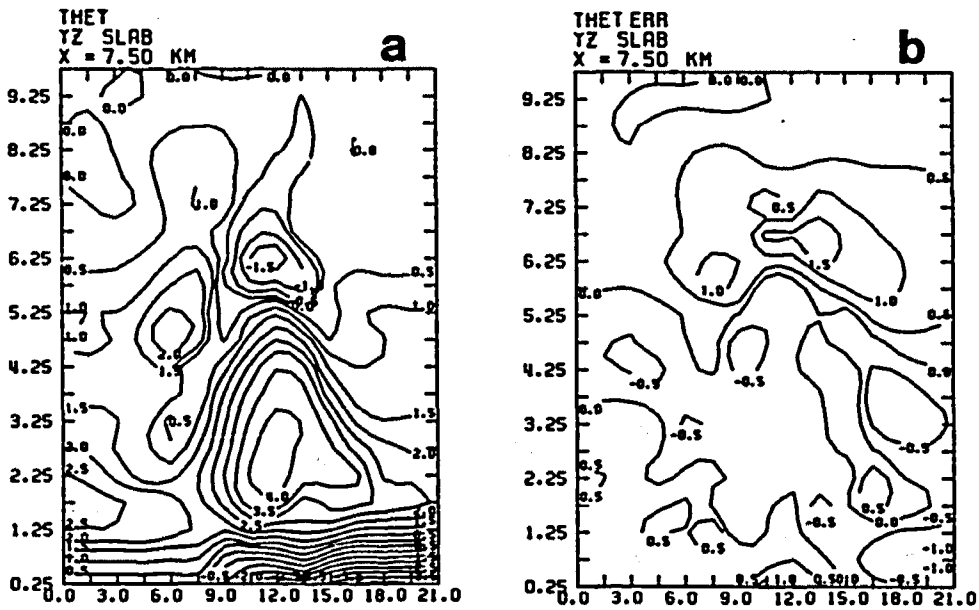

Fig. 3.5 Same as in Fig. 3.1, but for the results of experiment N and showing only kinematic model output (a) and difference field θ (b).

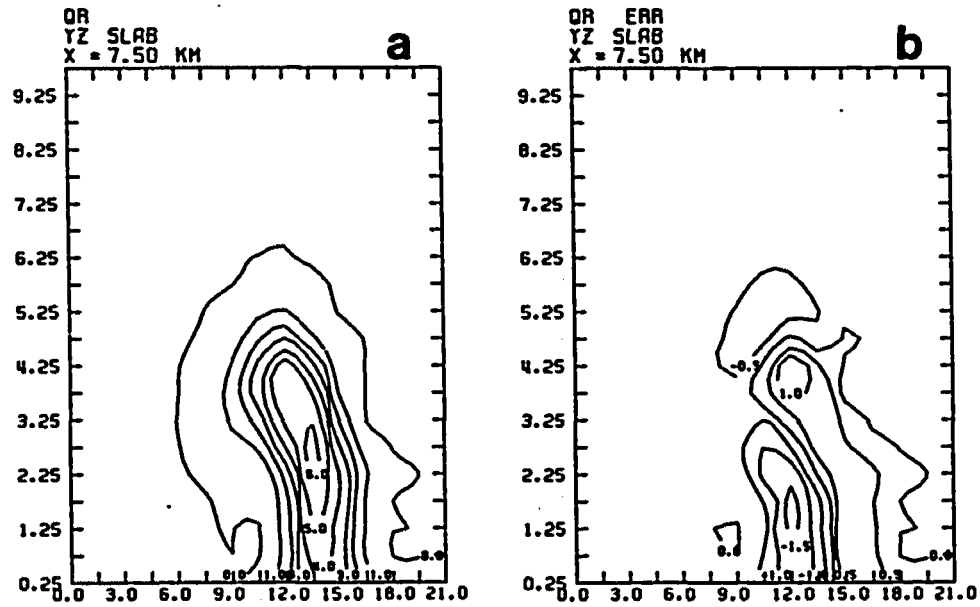

Fig. 3.6 Same as in Fig. 3.4, but for the results of experiments N and showing only kinematic model output (a) and difference field q_r (b).

noise fluctuations, there are no large systematic differences between the results of experiments C and N (best illustrated by comparing error fields). The additional error due to noise addition to the wind field is generally small compared with that error associated with experiment C.

Horizontal averages of error statistics for each of the four retrieval experiments, have been compiled separately for the updraft region ($w \geq 1$ ms^{-1}) and the rain region excluding updrafts ($q_r > 0$ and $w < 1$ ms^{-1}). This step has been taken to avoid excessive bias of means due to the relatively narrow cloud and precipitation core. Error statistics are not computed in the rain-free environment, where the steady approximation does not apply. Fig. 3.7 illustrates vertical profiles of error in the updraft region while Fig. 3.8 corresponds to the rain region. Panels (a) through (d) in each figure show horizontal mean error profiles for temperature, water vapor, cloud, and rain respectively, in relation to the profile of horizontal mean values of those quantities. A solid line represents the mean of the variable, the dotted line the extreme of that variable at a given level, the dash-dot line the experiment C profile, the dash-dot-dot line the experiment N profile, and the short dash line the experiment T profile. An error bar illustrating the experiment C rms error deviation is plotted with the experiment C profile. All plots are semi-logarithmic, with the vertical axis linear height (km AGL) and the horizontal axis logarithmic to illustrate the great ranges involved as well as to resolve the errors of the various experiments. Fig. 3.7 generally illustrates that errors are less than or of order 10% in the updraft region, with the thermal

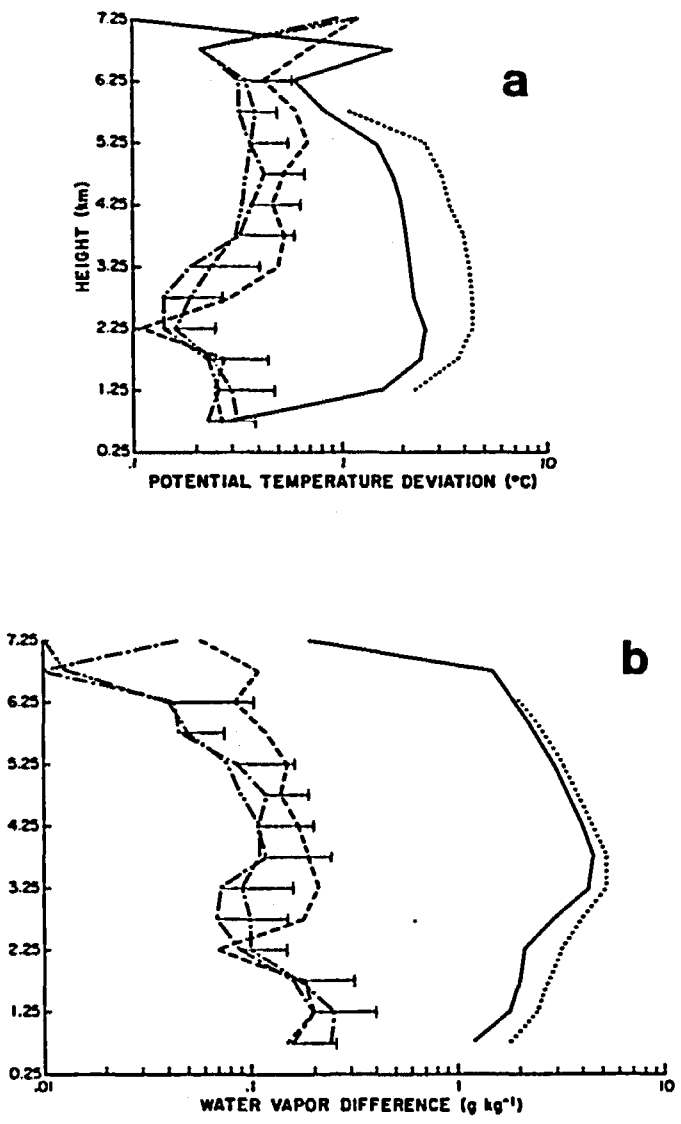

Fig. 3.7 Vertical profiles of θ (a), q_v (b), q_c (c), and q_r (d) error (deviation between retrieved and known) horizontally averaged over the region of $w > 1$ ms^{-1} and $q_r > 0$. The solid curve in each panel shows the average observed deviation from the base state in the model D output, while the dotted curve shows the maximum deviation profile. The vapor mixing ratio deviation from the environment is shown in (b). The dash-dot curve represents the experiment C error profile, the dash-dot-dot curve the experiment N profile, and the short dash curve the experiment T profile. Error bars representing one standard deviation above the mean at each level within the updraft region, are added to the experiment C profile.

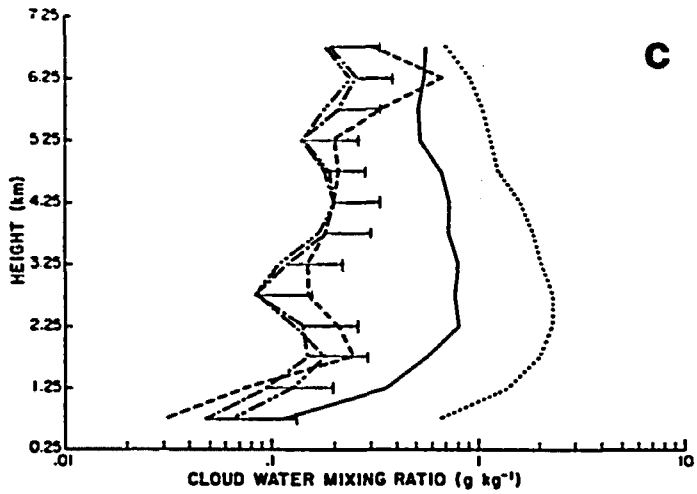

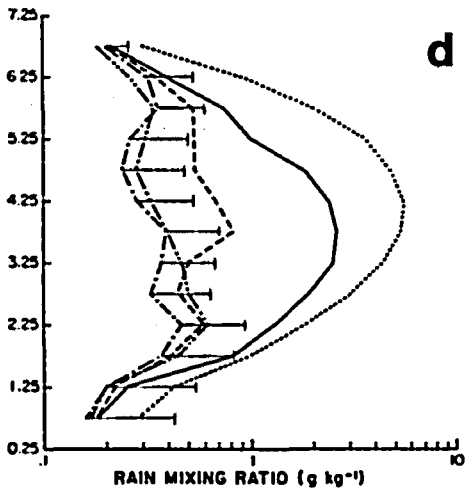

Fig. 3.7 (continued)

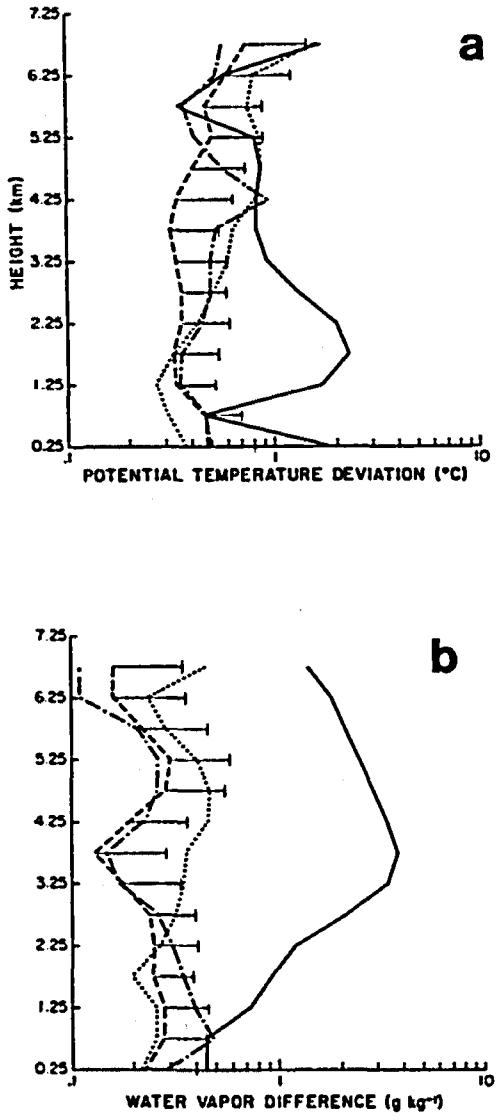

Fig. 3.8. Same as Fig. 3.7, but for the region of $w < 1$ ms^{-1} and $q_r > 0$. The maximum deviation from the base state is not shown, while the dashed curve represents the experiment C error profile and the dash-dot and dotted curves represent the experiment N and T error profiles respectively.

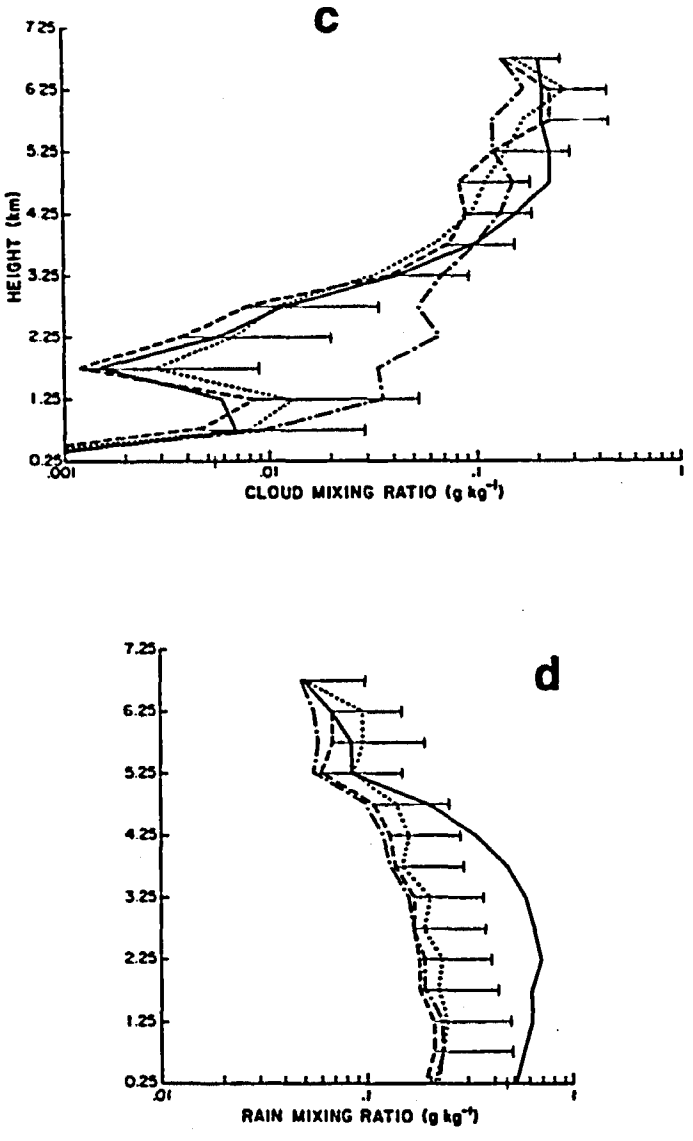

Fig. 3.8 (continued)

variables having errors of order 1%. Rain errors approach 100% at the base and summit of the updraft, although the magnitude of the rain mixing ratio itself is small at these levels and directly associates with diminished absolute errors. Minimizing the turbulent diffusion causes a significantly greater error than the addition of white noise to the wind field. Errors in Exp. T increase above 2.25 km due to noise production in the advection terms. In the rain region exclusive of updrafts (Fig. 3.8), relative errors tend toward 100% although the middle level fields are still rather well retrieved. This effect reflects a decreasing perturbation strength with roughly constant error magnitude. Hence errors due to non-steadiness appear to become important only on the fringes of the storm, and then only in a relative sense.

3.3 Analysis of retrieval error

Physical insight into the error producing mechanisms in model K will facilitate interpretation of model K output in real situations. Vertical profiles of various model terms have been constructed from term-by-term evaluation of the model equations applied to the model D output. Fig. 3.10 shows profiles of the absolute values of θ, q_v, q_c and q_r equation terms in the updraft core. The horizontal locations of these profiles relative to the 2.75 km rain water field, are shown in Fig. 3.9 by a dot labelled with the number one. Fig. 3.10a shows that the updraft is characterized by a balance between vertical advection of θ and condensation heating, with the local derivative playing a minor role in the θ equation. In the q_v equation (Fig. 3.10b), vertical advection of q_v is balanced by cloud condensation, with the local

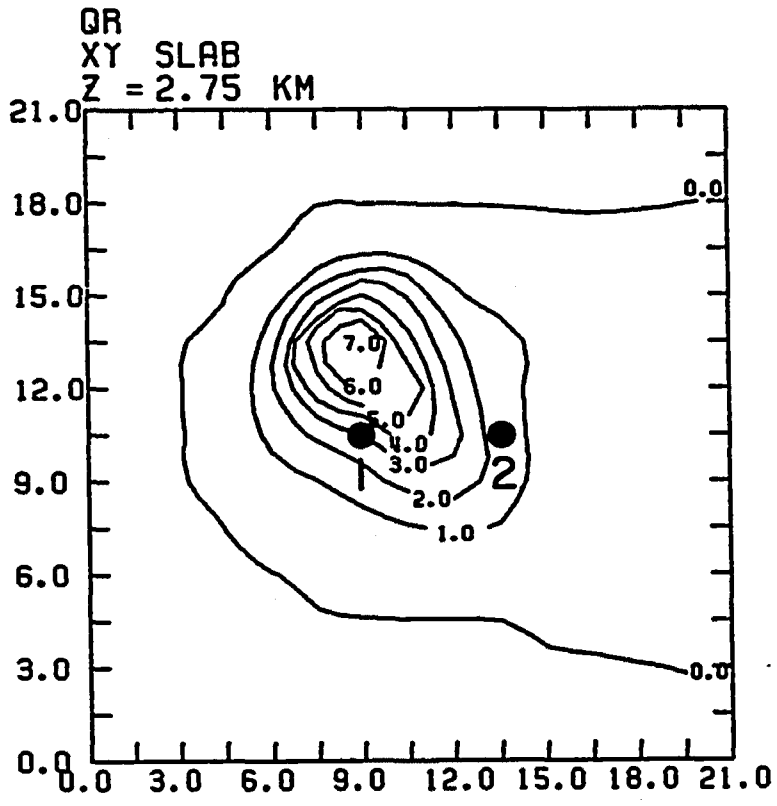

Fig. 3.9. Horizontal map of 2.75 km q_r field locating vertical profiles of model equation terms in Fig. 3.10 and Fig. 3.11. Dot numbered one (1) is located in the strong updraft, while dot numbered two (2) is downstream and outside of the updraft.

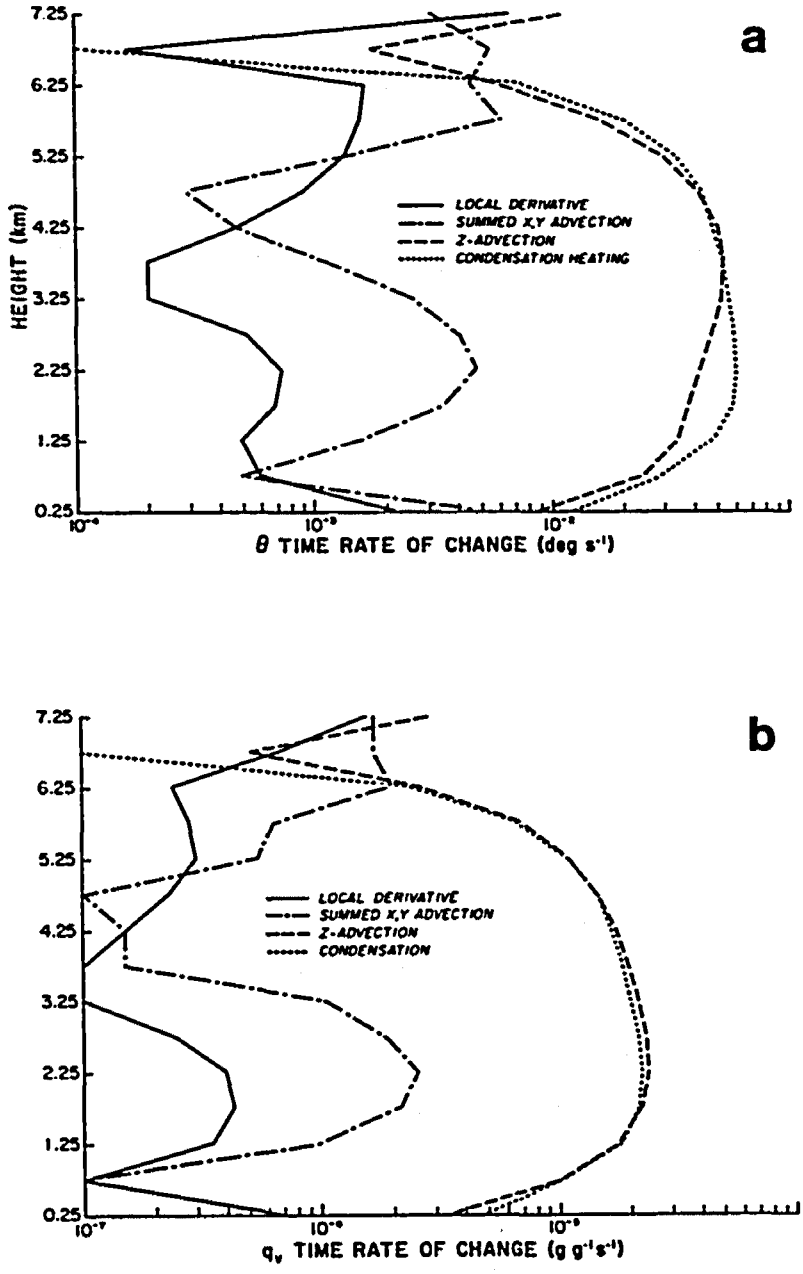

Fig. 3.10. Vertical profiles of selected θ (a), q_v (b), q_c (c), and q_r (d) equation terms within the updraft core, as located in Fig. 3.9. A key in each panel relates a specific equation term or group of terms to a specific curve type.

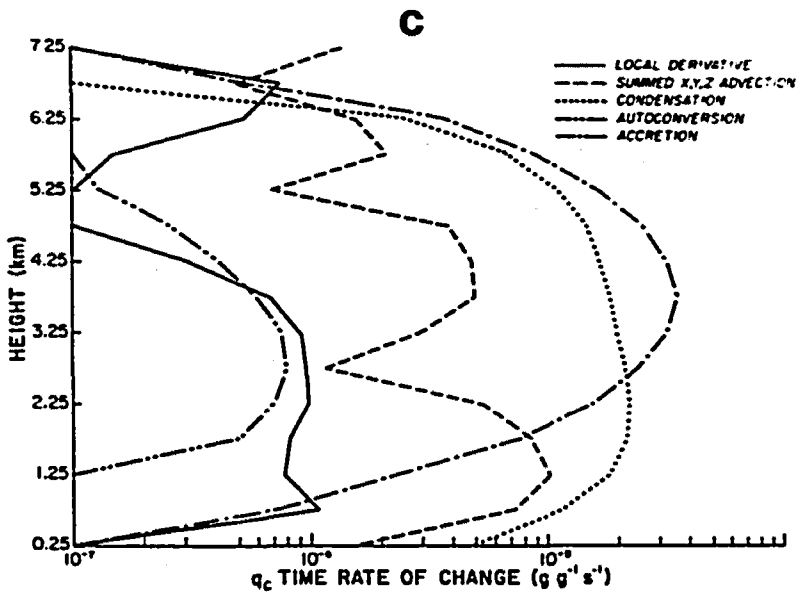

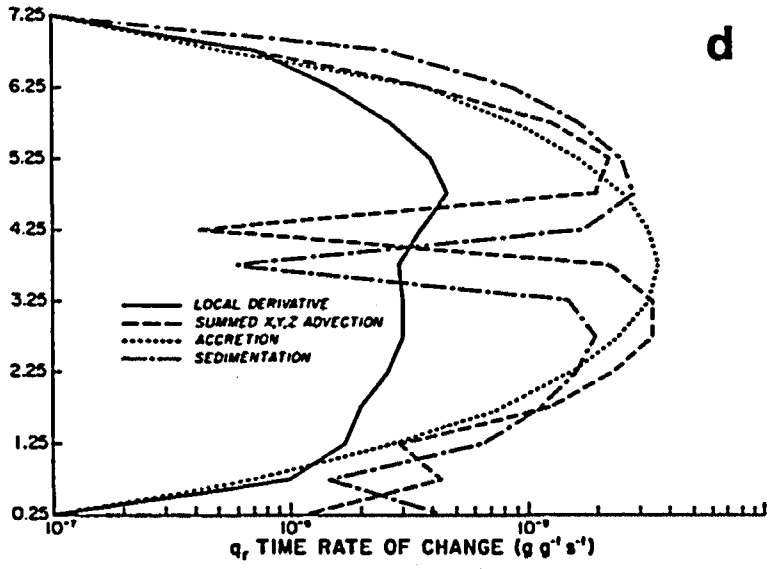

Fig. 3.10 (continued)

derivative again being negligible. The q_c equation terms (Fig. 3.10c) indicate that a more complex balance exists between condensation, accretion, and three dimensional advection, although the local derivative again is negligible. The q_r equation terms (Fig. 3.10d) reveal a balance between accretion, sedimentation and three dimensional advection. The pronounced local minimum of advection and sedimentation in the vicinity of 4 km associates with the local maximum of rain content. This leads to a small vertical gradient of q_r and consequently small vertical advection and sedimentation terms. The local derivative is negligible except near the ground and the cloud top, with a magnitude of 10% of the accretion rate in the middle level precipitation core and 25% immediately above and below that level. The local derivative of q_r is negative at all levels in the core, which is consistent with a slight decrease in storm intensity and the decrease of peak updraft already noted. The updraft region is generally in a quasi-steady state, the most notable exception being the q_r field near cloud top. The initial-boundary value problem posed by the time-dependent model effectively reduces to a boundary value problem, permitting accurate diagnosis via the steady solution of model K.

Fig. 3.11 shows profiles of q_r equation terms in the weak precipitation region downstream from the updraft core, at the location indicated by the dot in Fig. 3.9 labelled as profile 2. This figure is interpreted in a similar fashion as was Fig. 3.10d, except that here vertical advection is negligibly small compared to all other terms and is not shown. Although the local derivative of q_r is generally smaller than horizontal advection and sedimentation, it approaches 50% of the

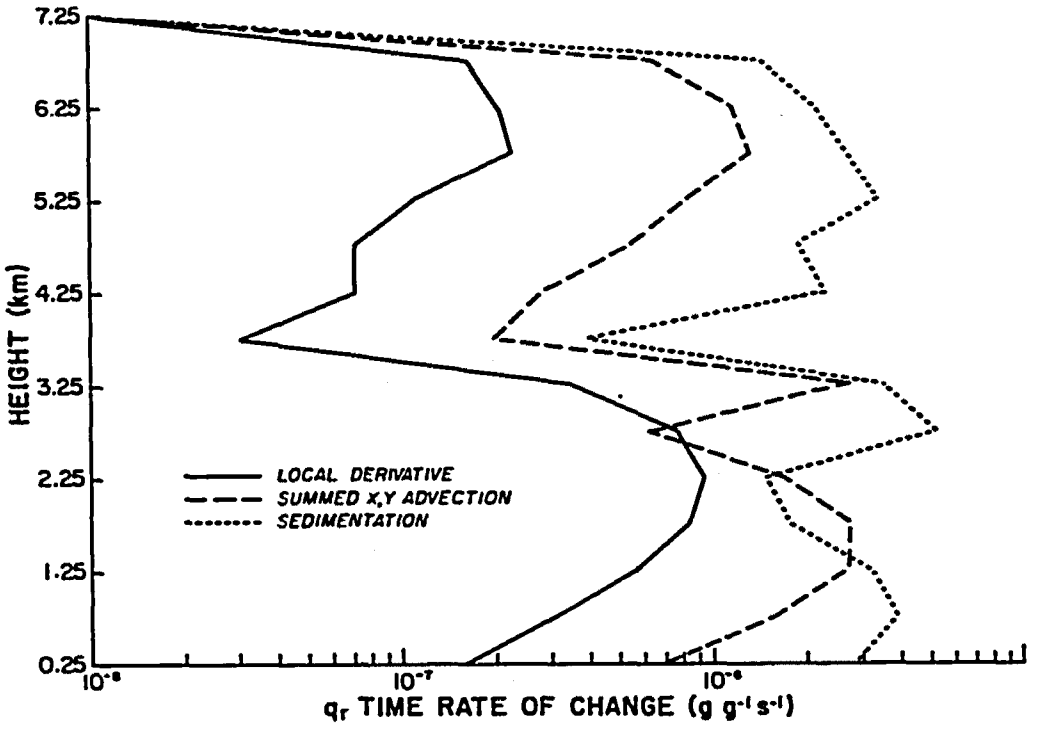

Fig. 3.11 Same as in Fig. 3.10, but for location 2 in Fig. 3.9 and for q_r equation terms only.

sedimentation rate at 2.25 km and at most levels is of the same order of magnitude. The steadiness assumption generally weakens from the storm core outward into the precipitation fringe area. A similar conclusion is obtained from the order of magnitude of the terms in the remaining governing equations of the model (not shown). A corresponding decrease in the q_c and q_r error as well as the difference between the error and mean values may be noted by inspecting Figs. 3.7 and 3.8. The θ and q_v error grows with increasing distance from the core. This is due to the effects of horizontal advection and diffusion outside the deep convective storm core. Both the mean and error components are transported downstream from the core, initially assuming the quasi-steady values of the core at a given level. Turbulent dissipation acts to exponentially diminish the mean and error of q_c and q_r as the parcel moves away from the core (due to zero mean and error values in the environment), with the result that relative error decreases with increasing distance from the core. Sedimentation transports q_r error downward. An analogous situation exists with respect to the θ and q_v fields, except that the error component in the environment exceeds the core errors (see Figs. 3.1c and 3.2c) and the action of diffusion is to transport error into the parcel following the motion. The error propagation is quantitatively difficult to establish due to the highly nonlinear character of the governing equations, although this heuristic discussion points out the key features of the observed error fields.

Simple scale considerations permit quantitative diagnosis of θ and q_v error magnitude in the convective core. By considering the balance

between advection and condensation implied by Fig. 3.10a and using the thermodynamic equation in the form of eq. 2.1, there follows

$$\frac{\partial \theta}{\partial t} = - w \frac{\partial \theta}{\partial z} + C,$$

where C is the condensation rate. Expanding θ into the sum of mean and error parts, the thermodynamic equation is rewritten as

$$\frac{\partial \theta'}{\partial t} = - \tilde{w} \frac{\partial \theta'}{\partial z} - \tilde{w} \frac{\partial \bar{\theta}}{\partial z} + C,$$

where a tilde (~) denotes an observed quantity and a prime denotes an error quantity. The vertical advection of the mean state θ balances condensation in the steady state, with the result that the local derivative of θ must be due only to vertical advection of θ'. This permits the representation of time t by the advective time scale $\tau = H/W$, where H is the depth of convection and W is the advection speed. For deep convection we have $\tau \sim \frac{H}{W} \sim \frac{10^4 \text{ m}}{10 \text{ ms}^{-1}} \sim 10^3 \text{ s}$. Consulting Fig. 3.10a, we note that typically $\left|\frac{\partial \theta}{\partial t}\right| \sim 10^{-4}$. Omission of the local derivative of θ should produce an error $\Delta\theta \sim \frac{H}{W} \left|\frac{\partial \theta}{\partial t}\right| \sim 10^{-1}$ deg based upon these scaling arguments, in good agreement with the observed error magnitude in Fig. 3.7a. Note also from Fig. 3.10a that the increase in $\left|\frac{\partial \theta}{\partial t}\right|$ with height is roughly correlated with increasing error in Fig. 3.7a with height. The magnitude of q_v retrieval error may also be explained by the omission of the local derivative from the governing equation. A similar effect must be present in the q_c and q_r equation, although the

presence of the nonlinear accretion term of the form $kq_c q_r$ renders a scale analysis more difficult.

In future experiments where the steady solution is used as the initial condition and time-spaced wind analyses are inserted during the time integration, the time propagation of the initial error is of interest. The previous discussion suggests that the initial error should be tranported from the convective cell in a period corresponding to the advective time scale. Replacing θ' by the horizontal average across the cell and integrating the linearized advection equation in time yields

$$\int_0^t \frac{d\overline{\theta'}}{\overline{\theta'}} dt = -\int_0^t \frac{\overline{\tilde{w}}}{H} dt,$$

or $\overline{\theta'} = \overline{\theta'}_o e^{-t/\tau}$, where τ is the advective time scale. This relation expresses an exponential decay of error as transients advect out of the domain and the characteristic solution of the advection equation becomes established. Nonlinear feedbacks in the full model e.g., precipitation interactions, will generally increase the time scale for decay of initial error.

The error analysis documented here has clearly shown the veracity of the steady state approximation for mature deep convection, as simulated by a three-dimensional dynamic cloud model. The results of this error analysis should extend to the case of real convection, although additional complications such as the presence of serious systematic errors in the analysed wind field, may be encountered. Recall from the discussion of the classical models in Chapter I that a weak echo region often associates with the low level inflow and updraft. This weak echo

may result in a data void where velocities are unobtainable. The elimination of updrafts in the low level inflow of the simulated cell or an actual thunderstorm would severely alter the thermal and microphysical variables in the storm core due to the weakening of moist static energy influx. The insertion of time-spaced wind analyses during model integration in future research holds the promise of mitigation of the error which is due to the steadiness approximation at the initial time. An expanded microphysical parameterization including ice must be employed in real storms. The error levels reported here appear insignificant from either a microphysical or dynamical viewpoint, although a more definitive conclusion must await the results of real data tests reported in the next chapter of this thesis.

CHAPTER IV

MODEL TESTS WITH REAL DATA

The complete warm/cold cloud version of the kinematic model is now applied to synthesized Doppler wind fields in two different storms. The first storm was non-severe while the second storm produced large hail. These cases test the ability of the kinematic model to discriminate between intense and weak convection. The first case probably has more accurately derived winds since it is based on data from three radars and an overdetermined two Doppler analysis as opposed to a dual Doppler analysis in the second case. The effect of velocity errors on the model solution can be qualitatively assessed. In the second case, a subjective wind field adjustment based on conceptual flow models results in dramatic improvement in the verification of model reflectivities. This suggests the possibility of using derived microphysical variables to improve wind synthesis from Doppler radars. The model is used to diagnose the buoyancy structure of both storms, which lends insight into storm dynamics. Inspection of model-derived bulk precipitation growth rates delineates the dominant microphysical processes in the warm and cold regions of these clouds. In this regard, the hail production mechanisms in the Wynnewood storm are of particular interest.

Each case study begins with a presentation of the Doppler wind fields. The temperature and water substance fields are derived from the model, and selected output is presented and discussed. The first case emphasizes the comprehensiveness of model data, the qualitative

consistency of airflow and retrieved buoyancy, and the sensitivity of retrieved total reflectivity to the variation of several important model parameters. The second case stresses the impact of airflow changes on retrieved reflectivity. The chapter concludes with a discussion of precipitation formation and growth processes in both storms.

4.1 Real data initialization

Multiple Doppler velocities are analyzed following procedures outlined in Ray et al. (1980) and Ray and Sangren (1983). The variational adjustment of observed horizontal winds is effected in accord with observational error such that the anelastic continuity equation as well as upper and lower w boundary conditions are simultaneously exactly satisfied. In the second case study, a smooth transition from observation domain to environment (as defined by a proximity sounding) is provided by extrapolating horizontal wind components up to 8 km from the observational domain boundary. The extrapolation uses a Cressman weighting function, and the environmental wind serves as a first guess value. At greater distances from the storm, the wind is set to its environmental value. The procedure in the first case study is to replace missing horizontal velocities by environmental values without additional adjustments. Horizontal winds are smoothed by making three passes using a 9-point Cressman filter, although only guessed wind vectors are replaced by their filtered counterparts. Vertical motion at all points outside the Doppler analysis volume is set to zero. Significant retrieval errors may result from this treatment if inflow was poorly defined by the analysis. Cell motion, as deduced from visual correlation of successive WSR-57 radar PPI scans, is subtracted from the

ground-relative observed horizontal wind fields. The initial conditions for potential temperature and vapor mixing ratio in the updraft core are based on a saturated adiabat derived from a proximity sounding, while stratified environmental values are used elsewhere. The updraft core is subjectively defined in terms of the exceedence of a preset threshold, typically 5 ms^{-1}. The top-hat initial profiles are smoothed into bell-shaped profiles with a two-dimensional fourier filter[1], which has a better response function than the standard Cressman filter. Cloud and precipitation mixing ratios and associated number concentrations are normally initialized to zero. The single exception to this rule involves the specification of inflow boundary conditions for rain and hail in the 28 May case study, which is discussed below in this chapter.

4.2 Model tests with 27 May 1979 data

These tests utilize triple Doppler wind fields and the 1400 FSI proximity sounding for the Broxton storm which occurred in central Oklahoma on 27 May 1979 during the SESAME field program. Inspection of soundings from the Chickasha (CHK) and Mountain View (MTV) stations reveal no systematic variations of low level temperature and moisture in the mesoscale environment of the Broxton storm, which might bias inflow conditions and precipitation production. The cloud model is utilized for microphysics sensitivity tests involving inclusion or exclusion of the ice phase and variation in the numerical value of several important microphysical parameters. The observed wind field is not extrapolated beyond the Doppler analysis domain in these tests, since the

[1]Dr. Kenneth Johnson, NSSL, private communication (1982)

Doppler-derived winds on the fringes of the storm generally agree very closely with the proximity sounding. The proximity sounding defines the horizontal wind at all points between the Doppler analysis boundary and the regular computational domain boundaries. The initial conditions used are the same for all tests, following from the findings in Chapter III. The model domain used in all integrations is a regular 25 by 25 by 15 mesh with a grid spacing of 1 km and origin (x,y,z) coordinates of (-89, -38, 0.5) km relative to the Norman Doppler radar. The model is integrated forward in time using a 10 s time step for a total time period of 80 min.

The observed wind field at the 6.5 km level is shown in Fig. 4.1. Note that Doppler and environmental sounding winds have been combined here. Horizontal velocity vectors are scaled according to the value indicated at upper right. East is to the right, making north toward the top of the page. Each model gridpoint is represented by a vector. The stippled regions denote vertical velocity between 5 and 15 ms^{-1}, with enclosed regions indicating extreme values. Bold horizontal and vertical lines denote the orientation of vertical west-east and south-north cross-sections to be referred to later in this section. The updraft is embedded in a prevailing southwesterly flow, with a stagnation point near the core at (8,8). A feeder cell updraft core is located on the upwind flank of the main updraft, at the coordinates (3,7).

The observed wind fields are further illustrated by vertical south-north and west-east cross-sections through the updraft core in Figs. 4.2 and 4.3, respectively. Orientation of the sections is shown in Fig. 4.1. The maximum updraft is 30.7 ms^{-1} at 10.5 km AGL. Axes are labelled

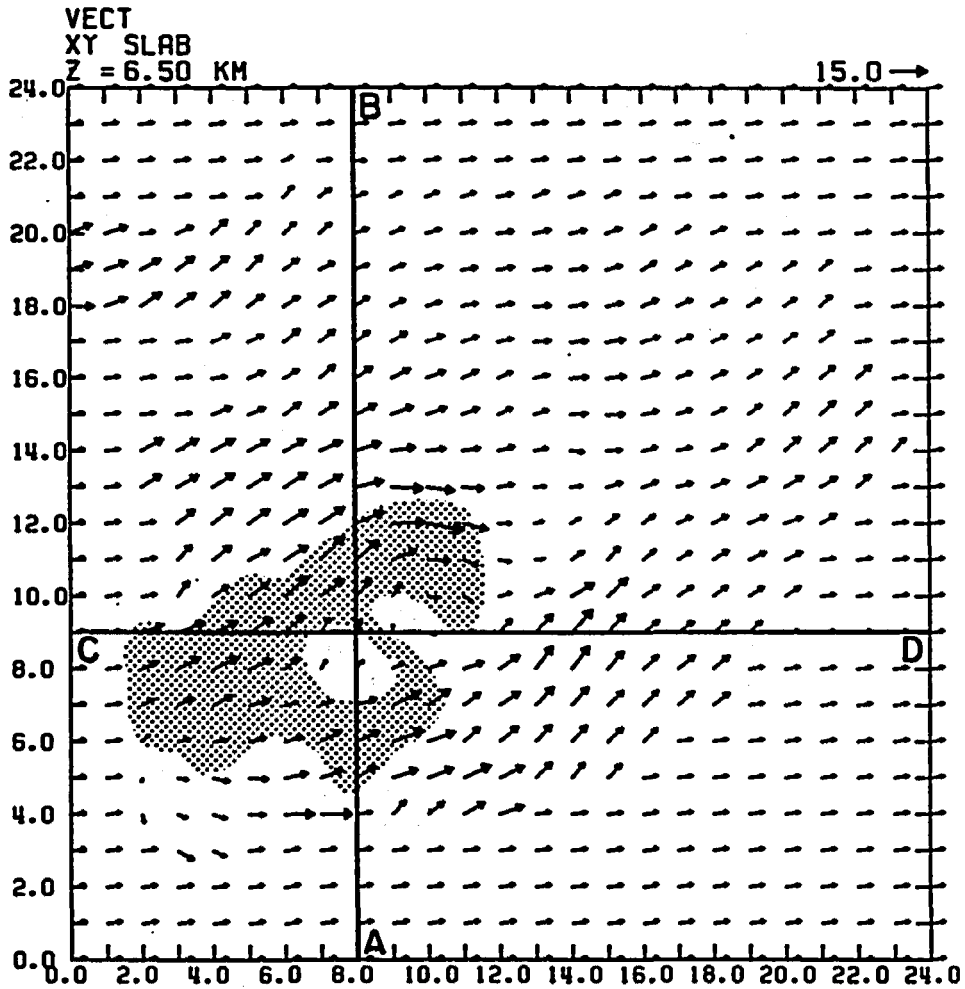

Fig. 4.1 Observed horizontal wind field used in model calculations at the 6.5 km level, at 1437 on 27 May 1979. Velocity scale is indicated at upper right. Horizontal coordinate is west-east distance (1.0 km grid spacing) while vertical coordinate is south-north distance. The stippling denotes vertical velocity between 5 and 15 ms^{-1}, with enclosed regions indicating extreme values. Bold lines denote the locations of vertical cross-sections AB and CD to be referred to in the text.

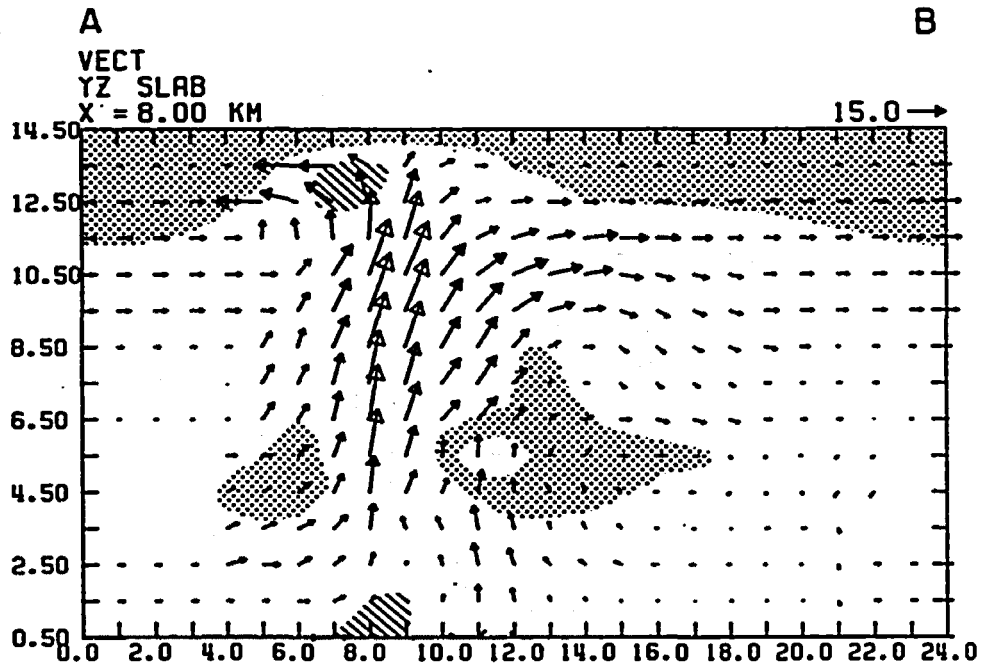

Fig. 4.2 Vertical south-north cross-section AB of observed winds, oriented as indicated in Fig. 4.1. Velocity scale is at upper right. Stippled regions indicate a u component between 10 and 15 ms^{-1}, while hatching indicates a u component less than -3 ms^{-1}.

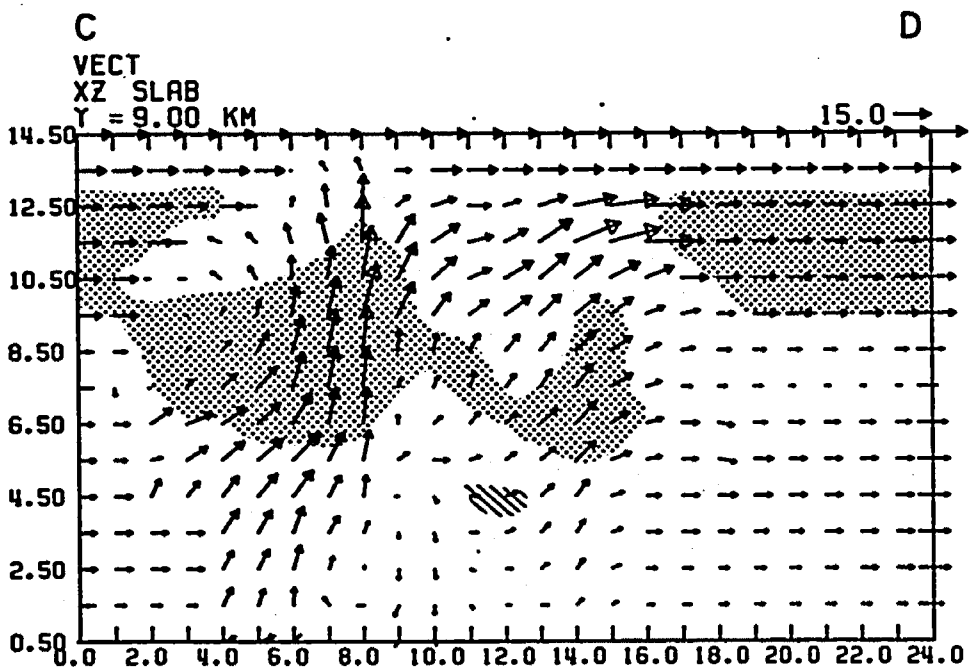

Fig. 4.3 Vertical west-east cross-section CD of observed winds, oriented as indicated in Fig. 4.1. Velocity scale is at upper right. Stippled regions indicate a v component exceeding 5 ms^{-1}, while hatching indicates a v component less than -5 ms^{-1}.

with units of distance (km), with height (z) on the vertical axis. Stippled regions indicate a positive normal velocity component, with negative values in hatched regions. In Fig. 4.2, stippling indicates a u component between 10 and 15 ms^{-1} while hatching denotes a speed less than -3 ms^{-1}. In Fig. 4.3, the v component thresholds are $\pm$ 5 ms^{-1}. Key velocity features in Fig. 4.2 are the strong deep updraft at center, flanking westerly wind maxima exceeding 10 ms^{-1} in middle levels, an outflow layer in the upper third of the cloud, and a horizontally split updraft profile in low levels. The weak split coincides with easterly winds, which are associated with low level outflow. In Fig. 4.3, the main updraft is located on the west flank of the storm with a broad weak updraft on the east side of the cell. Lack of data beneath the west flank echo overhang in the vicinity of (2,2.5) causes updrafts to be erroneously excluded from the analysis in that region. Meridional circulation in middle levels associates with a barrier flow pattern around the western updraft.

A total of nine sensitivity tests were performed using this wind data set. These are listed in order in Table 4.1 along with a brief description of pertinent model properties. The full warm/cold cloud model has subjectively been chosen as the control experiment with D_g = 0.3 cm and $\nu_c = 0$[1]. The control experiment also uses the Alofs and Liu (1981) CCN distribution $N = 3990\ s^{.643}$ (see Appendix C.6 for details). In experiment 27-2 the warm cloud bulk parameterization of Kessler

[1]This choice of ν produces a broad droplet distribution. Refer to discussion in Chapter II regarding the physical meaning of the shape parameter.

TABLE 4.1: 27 May 1979 (Sensitivity Tests)

EXPERIMENT	DESCRIPTION
27-1	Warm/cold cloud (D_g = 0.3, ν_c = 0)
27-2	Warm cloud bulk parameterization, no ice
27-3	Warm cloud gamma parameterization, no ice
27-4	Same as 27-1, D_g = 0.5 cm
27-5	Same as 27-1, ρ_h = 0.9 g cm^{-3}
27-6	Same as 27-1, ν_c = 3
27-7	Same as 27-1, reduce CCN concentration (N=1000 $s^{0.6}$)
27-8	Same as 27-1, E_{ic} = 1.0
27-9	Same as 27-1, slab symmetry

(1969) is utilized, while in experiment 27-3 the two moment gamma warm cloud parameterization is employed. In experiment 27-4, the effect of the hail parameter D_g on ice-hail conversion rate is tested by setting D_g to 0.5 cm. In experiment 27-5, the full model is run with a constant hail density of $\rho_h = 0.9$ g cm^{-3}. In experiment 27-6, the cloud shape parameter ν_c is reset from 0 to 3 to produce narrower droplet distributions. In experiment 27-7, the maximum cloud concentration is reduced to 25% of the control case value by using the modified CCN distribution $N=1000\ s^{0.6}$ to nucleate droplets. In experiment 27-8, the precipitating ice collection efficiency for cloud is increased to unity. In experiment 27-9, the effects of restricting circulation to two dimensions in a west to east cross section through the cloud are illustrated. A general finding of these experiments is that the thermal fields are rather insensitive to changes in microphysics which significantly modify the water and ice contents. Inclusion/exclusion of ice and hail associates with temperature differences of 0.1° C in the cloud core, because the latent heat of fusion is one order of magnitude smaller than the latent heat of vaporization. The model output for experiment 27-1 is discussed below in some detail, followed by intercomparisons of model output reflectivities and selected microphysical quantities of the different tests to illustrate sensitivity.

Selected model output of control experiment 27-1 is illustrated by horizontal sections at the 6.5 km level in Fig. 4.4. This section corresponds to velocities in Fig. 4.1. Fig. 4.4a through 4.4f show respectively temperature deviation (°C) from the environment, cloud mixing ratio (g kg^{-1}), cloud number concentration (cm^{-3}, multiply by 10^3), hail

mixing ratio (g kg^{-1}), model output reflectivity (10 log Z) obtained by summing partial reflectivities of rain, hail, and ice, and the observed reflectivity (10 log Z) from the CP4 radar. The updraft core at (8,8) (see Fig. 4.1) is warm and positively buoyant (Fig. 4.4a), but the cloud content of 1 g kg^{-1} and concentration of 100 cm^{-3} (Figs. 4.4b-c) are substantially below adiabatic levels due to intense scavenging from hydrometeors such as rain and hail. This is illustrated by comparing hail mixing ratios (g kg^{-1}) in Fig. 4.4d with the cloud fields. Hail accumulates in strong updrafts. Near-adiabatic cloud conditions exist to the west of the main updraft, in a region of low precipitation content. The use of the Alofs and Liu CCN distribution produces a cloud concentration maximum in this region of over 3500 cm^{-3}. If the Twomey parameters for the cloud activity spectrum had been used in the cloud nucleation parameterization (Appendix C.6, eq.1), the peak concentrations would have decreased to about 2000 cm^{-3}. Peak droplet concentrations in case 27-7 are near 1000 cm^{-3} due to the chosen value of the CCN distribution coefficient. The mean cloud droplet diameter of 10 μm in the adiabatic region increases with decreasing concentration[1]. Comparison of output reflectivity to observed reflectivity (Figs. 4.4e-f) indicates good agreement of the location, orientation and peak values in the storm core. The model reflectivities are about 5 dBZ too high, although the individual radars in the analysis measure reflectivities tending to differ by about 3 dBZ. Hence the

[1]Low concentration is necessarily balanced by a large mean volume droplet for fixed cloud content in the gamma parameterization. Refer to discussions in Chapter II and Appendix B for further details.

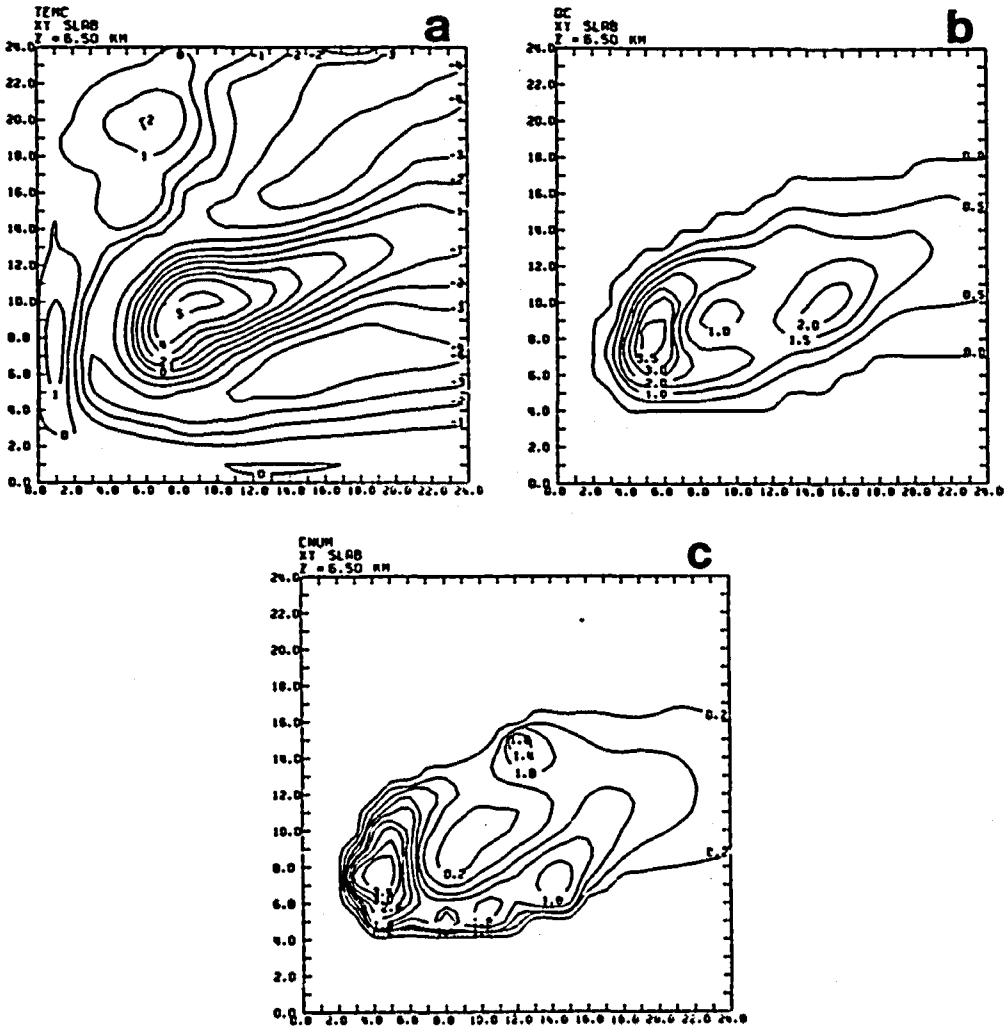

Fig. 4.4 Selected model output from experiment 27-1 in horizontal sections at the 6.5 km level, corresponding to velocities in Fig. 4.1. (a) temperature deviation from environment (°C), contour interval 1°C; (b) q_c (g kg^{-1}), contour interval 0.5 g kg^{-1}; (c) N_c scaled by 10^{-3} (cm^{-3}), contour interval 300 cm^{-3}; (d) q_h (g kg^{-1}), contour interval 0.5 g kg^{-1}; (e) computed model total reflectivity (dBZ), contour interval 5 dBZ; (f) observed reflectivity (dBZ), contour interval 5 dBZ.

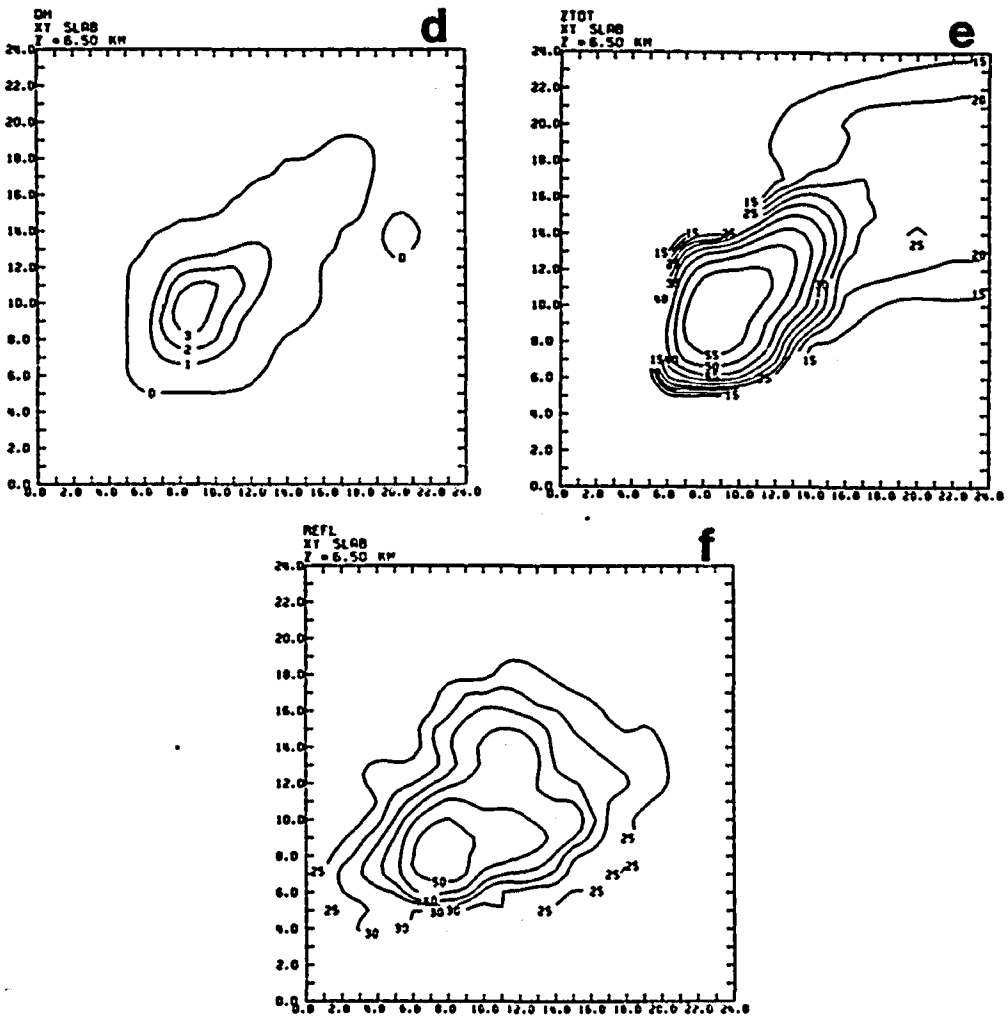

Fig. 4.4 (continued)

verification values are close to the noise level of the verification data. The secondary observed reflectivity maximum at (12.,13.) is moving from west to east with the mean flow, based on inspection of successive WSR-57 PPI scans. This feature represents the remains of an older cell, so that time-spaced wind analyses would be needed to retrieve this feature. An average graupel density of 0.5 g cm^{-3} with computed hail mixing ratios, would yield reflectivities (Appendices D.1 and E.1) in exact agreement with observations. Heymsfield (1978) finds that graupel densities in Colorado cumulus congestus clouds are typically lower than 0.5 g cm^{-3}, although this quantity is dependent on particle fallspeed and growth history as well as ambient temperature and cloud droplet size. Two important characteristics of the middle level storm structure are the existence of thermally buoyant updrafts in agreement with dynamics, and a large range of cloud conditions across the updraft defined by sub-adiabatic to near-adiabatic mixing ratios. This variation of cloud properties is due entirely to the presence of variable quantities of hydrometeors, and unrelated to dilution by turbulent mixing.

Control case model output is further illustrated by selected fields in a vertical south-north cross-section through the updraft core, as oriented in Fig. 4.1. Figs. 4.5a-f show respectively the potential temperature deviation from the environment (°K), the vapor mixing ratio (g kg^{-1}), cloud mixing ratio (g kg^{-1}), equivalent potential temperature (°K), model output reflectivity (10 log Z), and observed reflectivity (10 log Z). The thin dashed lines denote the freezing and -40 C levels for reference. The updraft core is associated with an excess potential

temperature slightly over 6 K. This quantity, vital to cloud dynamics, is directly related to acceleration in the vertical momentum equation via multiplication by the factor g/θ , where g is the acceleration of gravity and θ is the base state potential temperature. The retrieved temperature field appears to be dynamically consistent with the observed wind field, at least in a qualitative sense. A temperature defect of 11 K at (9.0, 12.5) is associated with the stable environmental lapse rate becoming less than the essentially dry adiabatic lapse rate within the upper levels of the updraft core. A temperature defect exceeding 4 K at (10.0, 0.5) is due to rain evaporative cooling in sub-saturated outflow air. The vertically oriented regions of temperature defect at y = 4 km and y = 14 km are due to the forced lifting of air parcels with anomalously low θ_e. Further research is necessary to determine if the updrafts associated with this feature are dynamically consistent. The vertical lifting of low level moisture by the updraft is well illustrated by Fig. 4.5b. This effect produces a vapor mixing ratio excess over the environment of 4 g kg^{-1} at 4.5 km, which enhances the thermal buoyancy. The cloud (Fig. 4.5c) has peak mixing ratios in middle levels and on the flanks of the precipitation core. Freezing converts all cloud liquid to non-precipitating cloud ice below -40 C. The windshift point or gust front at (12.0, 0.5), as located from Fig. 4.2, is beneath the low level updraft and associated cloud maximum. Note the rise in the cloud base to the south of the gust front within the precipitation core. The very common observation of low, dark shelf-like cloud ahead of the precipitation core of actual clouds bears great resemblance to the retrieved fields. A high equivalent potential temperature core

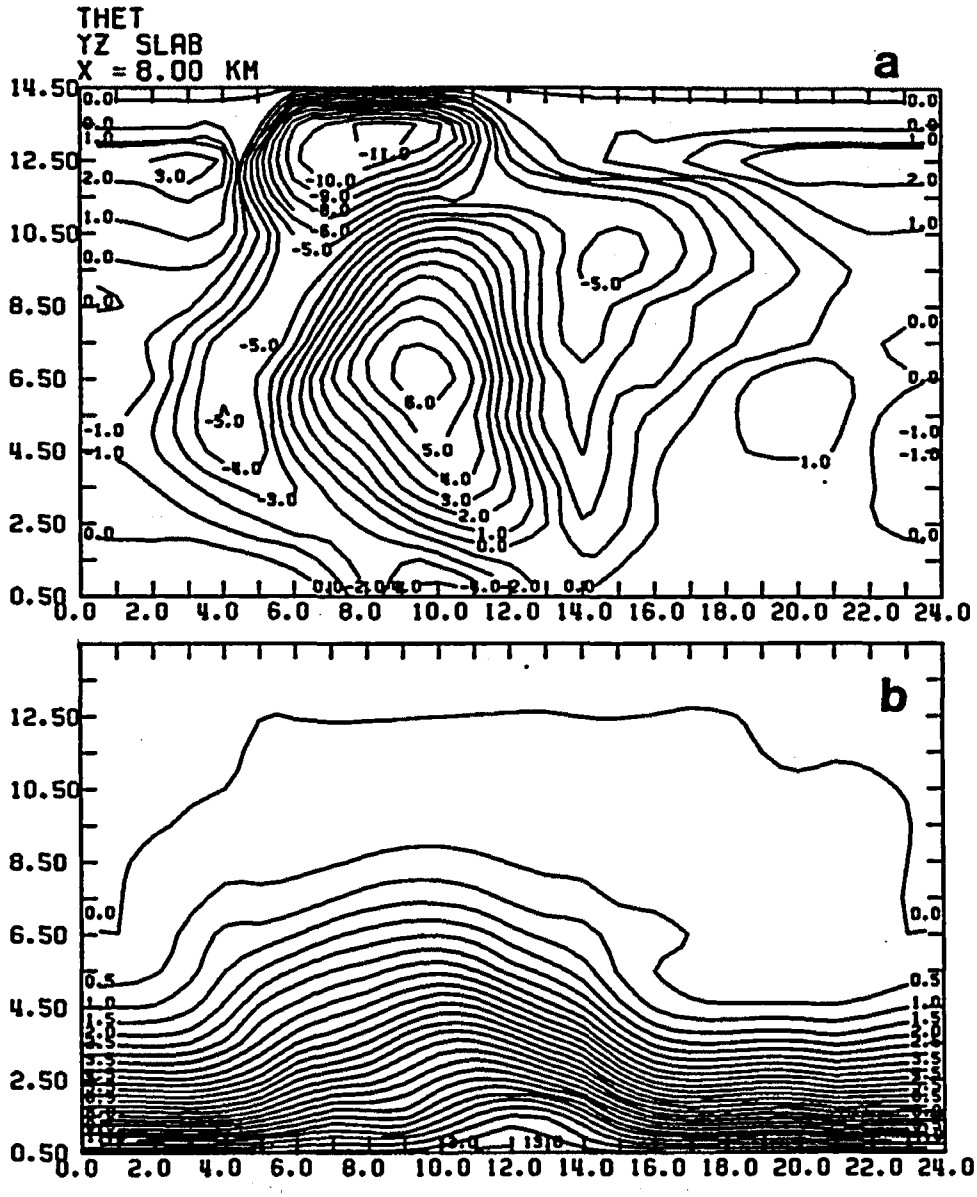

Fig. 4.5 Selected model output from experiment 27-1 in vertical south-north cross-sections AB, oriented as in Fig. 4.1 and corresponding to velocities in Fig. 4.2. (a) θ deviation from the environment (°C); contour interval 1 C; (b) q_v (g kg^{-1}), contour interval 0.5 g kg^{-1}, (c) q_c (g kg^{-1}), contour interval 0.5 g kg^{-1}; (d) θ_e (°K), contour interval 2 K; (e) computed model total reflectivity (dBZ), contour interval 5 dBZ; (f) observed reflectivity (dBZ), contour interval 5 dBZ. Thin dashed lines denote the freezing and -40 C levels for reference.

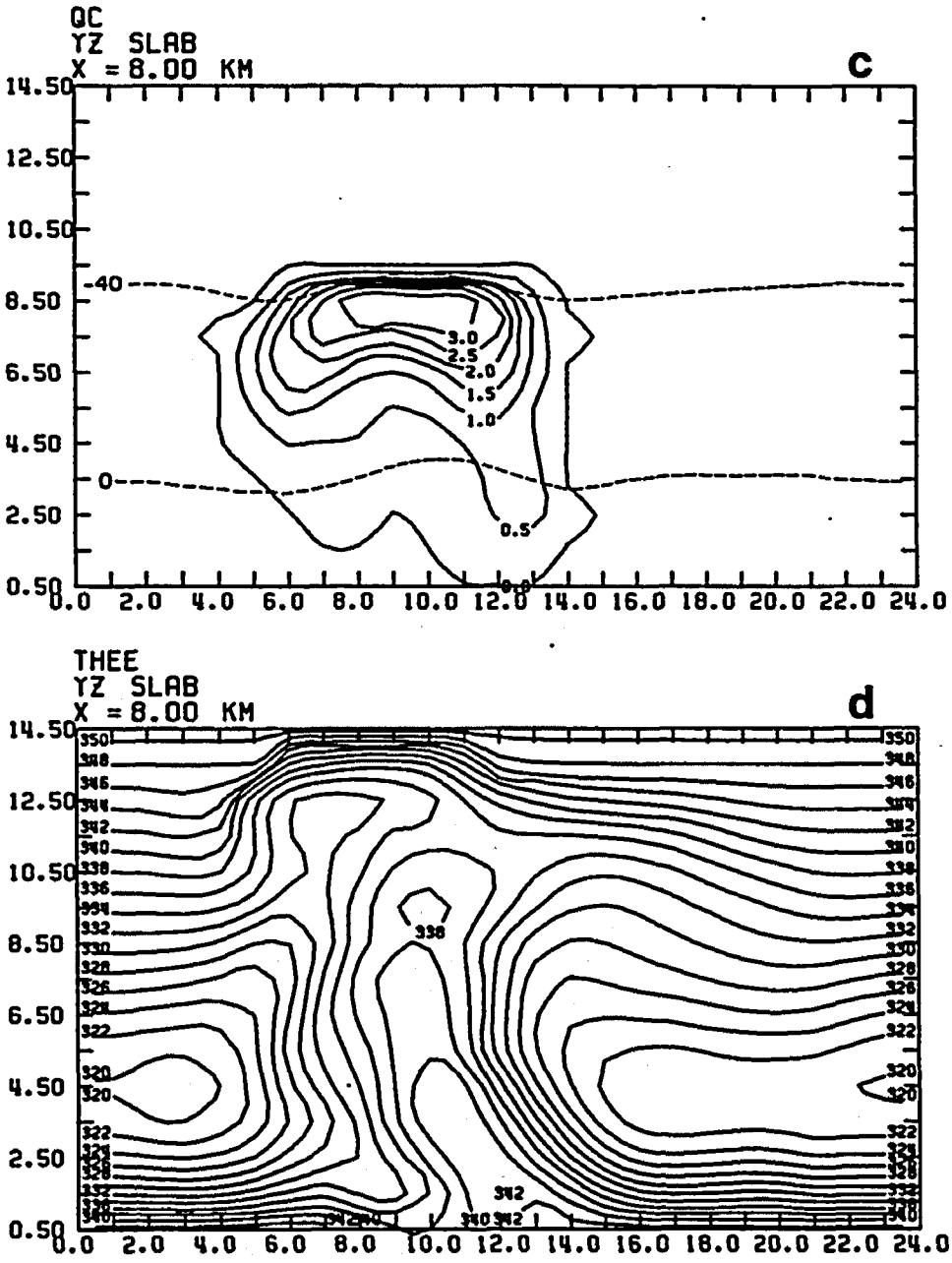

Fig. 4.5 (continued)

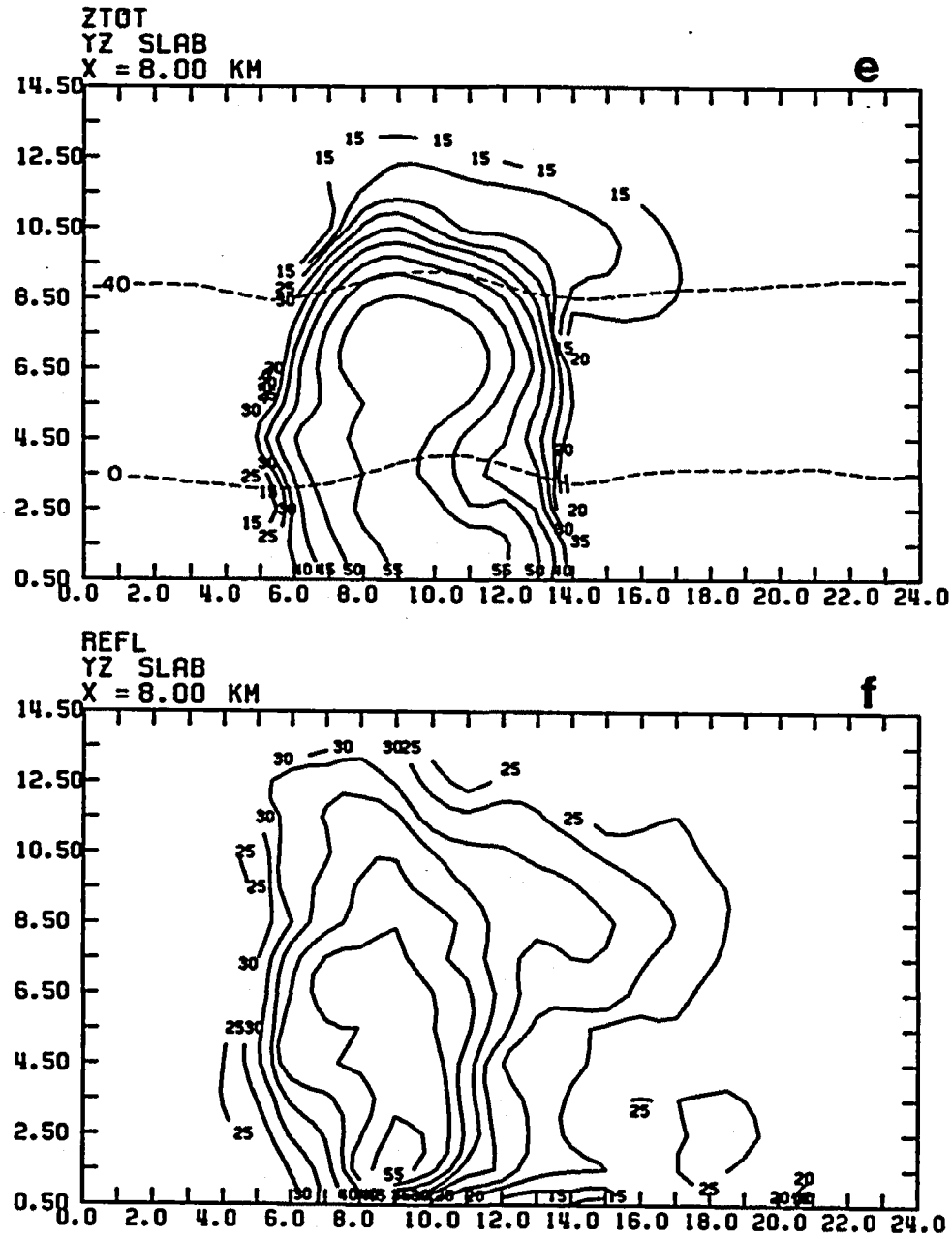

Fig. 4.5 (continued)

(Fig. 4.5d) coincides with the updraft, with cold middle level air characterizing the mesoscale environment.[1] The updraft core is moist adiabatic in agreement with classical models. Encroachment of cool middle level air from the downdraft is evident at (9.0, 1.5). Modelled and observed reflectivities (Figs. 4.5e-f) show good agreement in core location and orientation as well as peak reflectivities. The anomalously low observed reflectivities at 0.5 km are due to a calibration problem in the Norman radar data.

The relative maximum in reflectivity in low levels is influenced by the self-collection of raindrops. This is illustrated by vertical cross-sections in Fig. 4.6, which are oriented as in Fig. 4.5 and display rain quantities. Fig. 4.6a-d show the rain mixing ratio (g kg^{-1}), mean drop diameter (mm), drop total number concentration multiplied by 10^3 (cm^{-3}), and radar reflectivity (10 log Z), respectively. Although the rainwater maximum is located between 1.5 km and 2.5 km (Fig. 4.6a) the radar reflectivity maximizes below 1.5 km (Fig. 4.6d) due to increasing mean drop diameter below 1.5 km (Fig. 4.6b). Rain reflectivity experiences a net increase near ground due to the dependence on the sixth power of drop diameter (see Appendix B). The increase in drop size and reflectivity associates with decreasing drop concentrations below 2.5 km (Fig. 4.6c) which is due to the large hydrometeor self-collection (Appendix C.3). The ridge of high drop concentration extending from (8.,6.5) to (12.,3.5) is produced by cloud conversion to rain,

[1]This structure bears striking resemblance in all major features to the θ_e field in an Oklahoma squall line as simulated with a dynamic cloud model by Hane (1973).

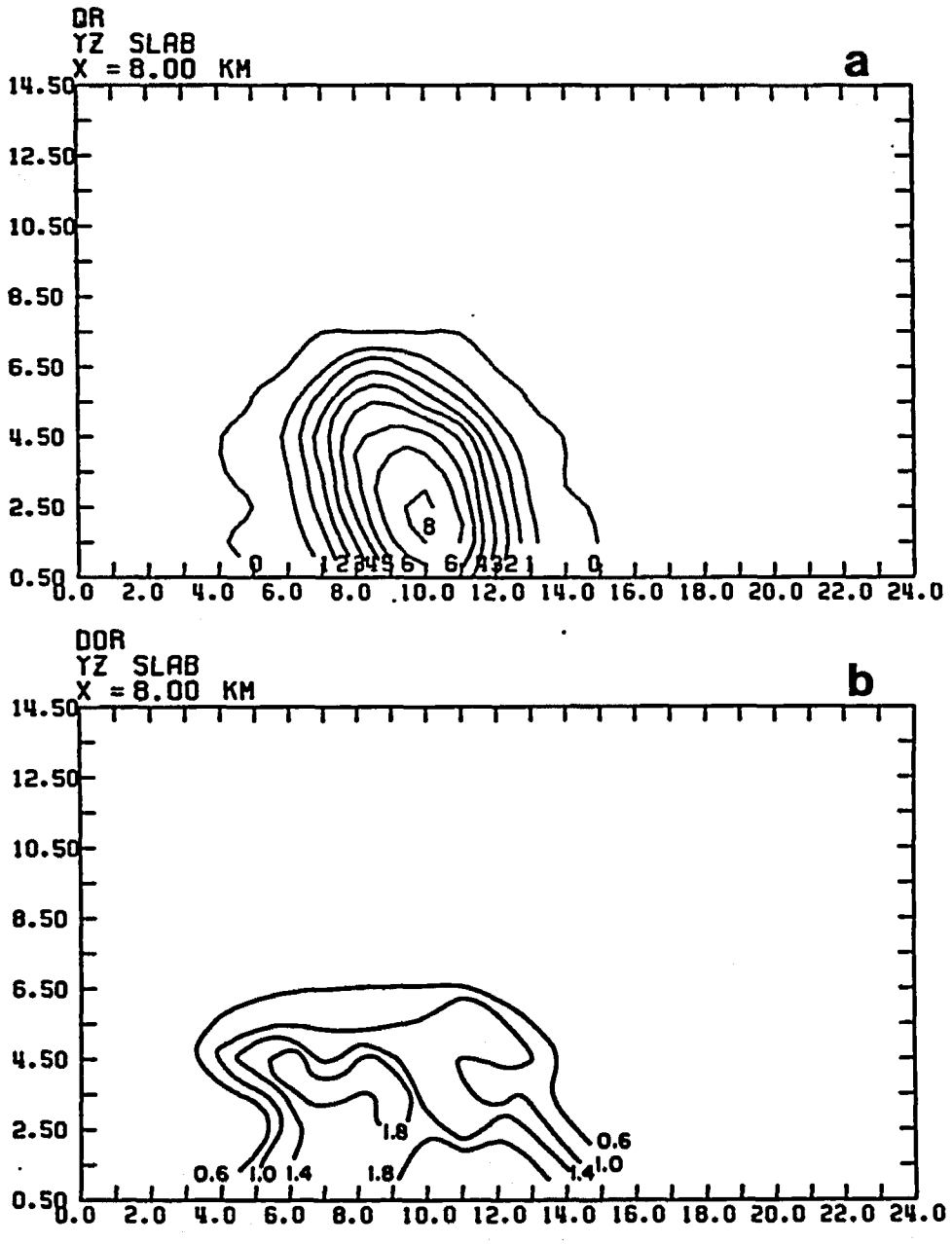

Fig. 4.6 Same as in Fig. 4.5, but showing only rain quantities. (a) q_r (g kg^{-1}), contour interval 1 g kg^{-1}; (b) mean volume drop diameter (mm), contour interval 0.4 mm; (c) N_r scaled by 10^3 (cm^{-3}), contour interval 10^{-3} cm^{-3}; (d) computed model rain reflectivity (dBZ), contour interval 5 dBZ.

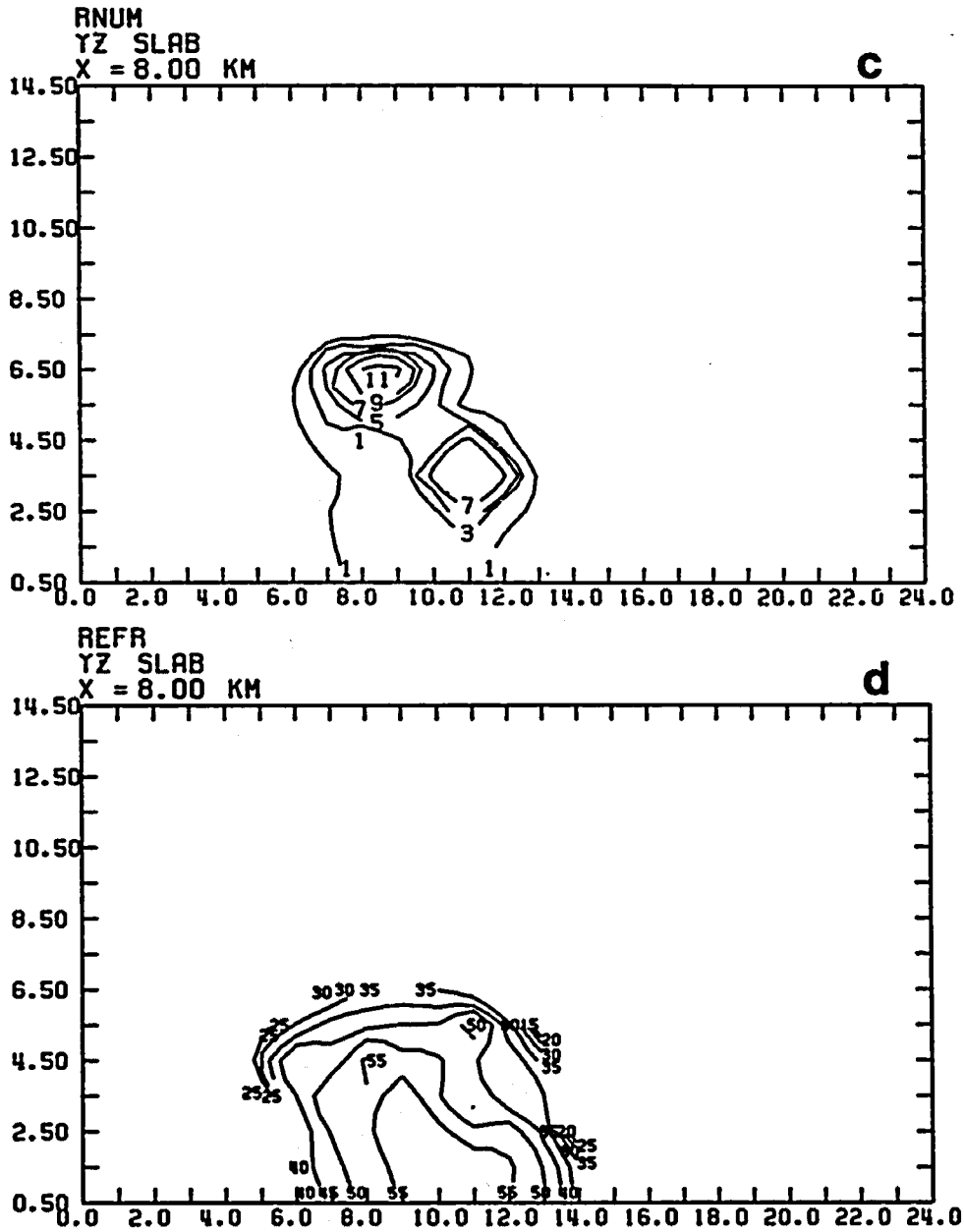

Fig. 4.6 (continued)

which locally dominates rain self-collection. Comparing Fig. 4.6d with Fig. 4.5e, the low level reflectivity structure is seen to be almost entirely due to rain properties.

Vertical west-east cross-sections of control case model output are shown in Fig. 4.7. These cross-sections are oriented as in Fig. 4.1. Fig. 4.7a shows model output reflectivity, Fig. 4.7b shows observed reflectivity, Fig. 4.7c shows cloud ice mixing ratio (g kg^{-1}), Fig. 4.7d shows mean cloud droplet diameter (μm), and Fig. 4.7e shows model output precipitating ice reflectivity. The freezing and -40 C levels are added for reference to Figs. 4.7a and c. The -15 C level is added to Fig. 4.7e for reference. The agreement between modelled and observed reflectivity is rather good, although the presence of an unobserved depression on the west flank of the modelled reflectivity is noted. The overhang in observed reflectivity from (3.0, 4.5) to (3.0, 8.5) is probably due to growth of small ice particles in the feeder cell. Referring to Fig. 4.3, a crucial lack of low level updrafts beneath the overhang is noted. Through the time lag associated with production of precipitation by cloud conversion, a spatial lag in the development of reflectivity results. This lack of updraft also prevents the middle level updraft from tapping low level moisture, with the result that cool, dry air is entrained and the cloud does not extend far enough to the west. The reflectivity depression would disappear if the updrafts were corrected. The precipitation core tilts to the west and into the inflow, in agreement with classical models. In Fig. 4.7c, we observe the formation of an extensive cloud ice anvil above 8.5 km. Additional measurements and research into cloud freezing are necessary to improve the modelling of

cloud ice nucleation. In Fig. 4.7d droplets of about 4 μm diameter form at cloud base and grow to over 20 μm on the east flank of the main updraft. In Fig. 4.7e, ice reflectivities maximizing between 30 and 35 dBZ are associated with temperatures near -15 C and the layer of peak deposition growth. These conditions agree closely with observations of northeastern Colorado cumulus (Dye et al., 1974).

A cursory assessment of model sensitivity to microphysical treatments is effected by the comparison of model output reflectivities. Fig. 4.8 displays vertical cross-sections (as in Fig. 4.5) of observed reflectivity (Fig. 4.8a), as well as model output reflectivities from experiments 27-2 through 27-8 (Figs. 4.8b-h, respectively). The Kessler bulk warm cloud parameterization (Fig. 4.8b) reproduces observed reflectivity features very well, although the core region of $Z > 55$ dBZ is too extensive.[1] The location of the precipitation core, the northward and southward extension of the anvil plume, and the change in echo cant from southward below 4.5 km to northward above 4.5 km, all indicate the controlling influence of the wind field. The gamma warm cloud parameterization (Fig. 4.8c) improves the representation of the low level reflectivity maximum in the observations, and the overall echo configuration shows the same kinematically controlled features as noted in the bulk retrieved reflectivities. The middle level notch at (11.0, 4.5) is an extension of the echo depression noted on the west flank of the full model retrieved reflectivity core (see Fig. 4.7a). The example directly

[1]This indictment is applicable to the result of several other retrieval experiments as illustrated by Fig. 4.8. Experiments including hail processes may have biased peak reflectivities due to the assumption of high density ice, as pointed out in the discussion of Fig. 4.4.

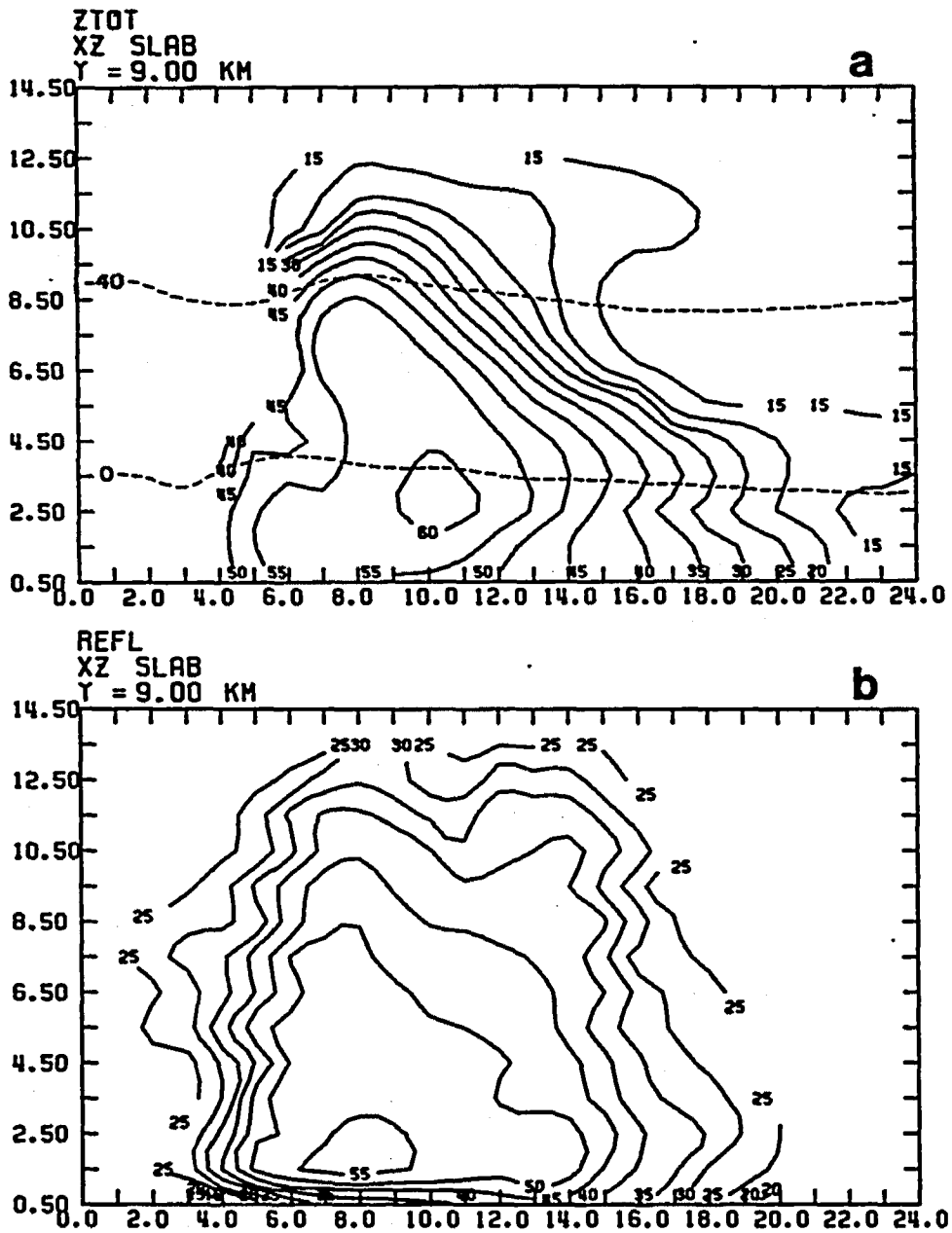

Fig. 4.7 Selected model output from experiment 27-1 in vertical west-east cross-sections CD, oriented as in Fig. 4.1 and corresponding to velocities in Fig. 4.3. (a) Computed model total reflectivity (dBZ), contour interval 5 dBZ; (b) observed reflectivity (dBZ), contour interval 5 dBZ; (c) q_x (g kg^{-1}), contour interval 0.5 g kg^{-1}; (d) mean volume cloud droplet diameter (μm), contour interval 4 μm; (e) computed model precipitating ice reflectivity (dBZ), contour interval 5 dBZ. Thin dashed lines denote freezing and -40°C levels for reference.

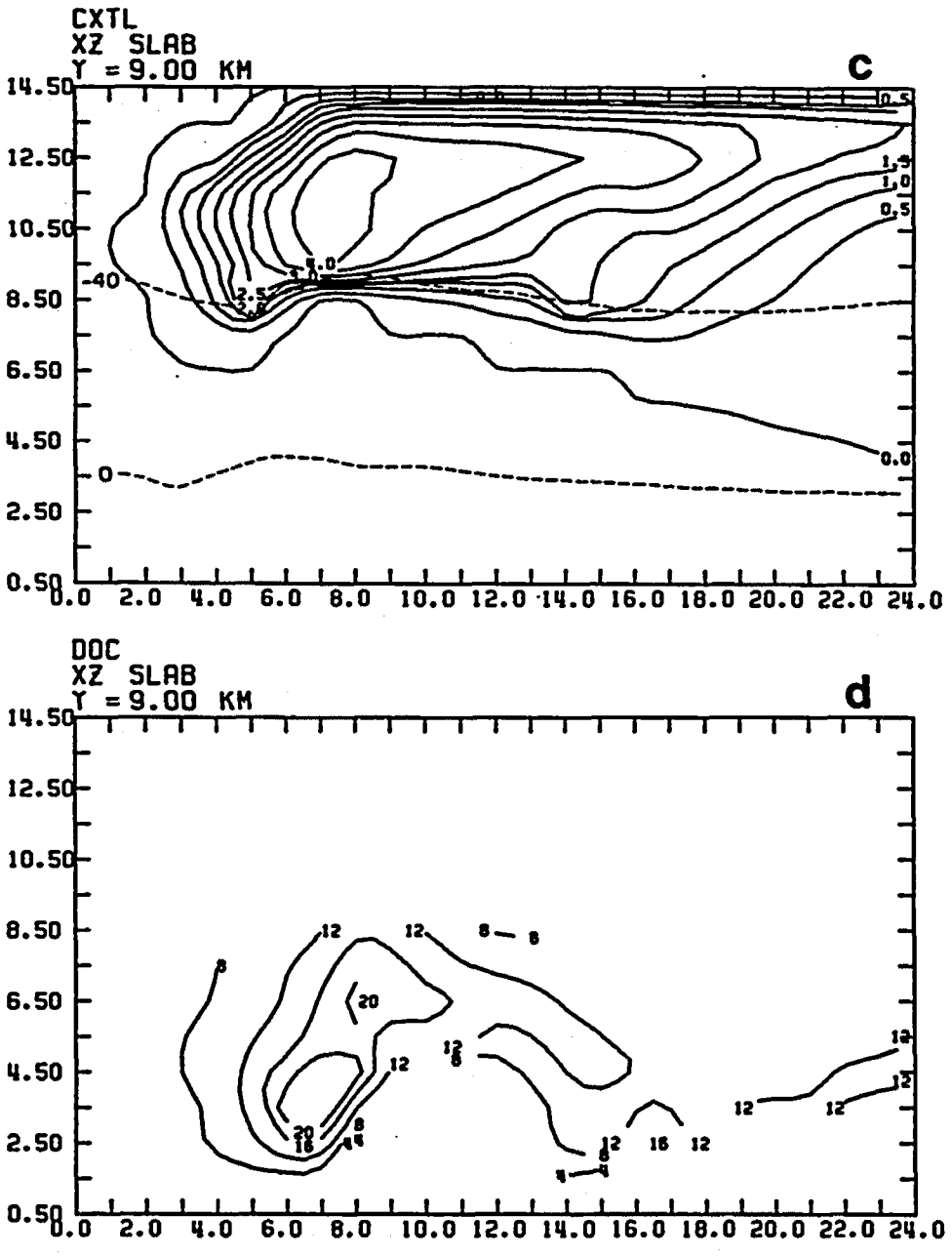

Fig. 4.7 (continued)

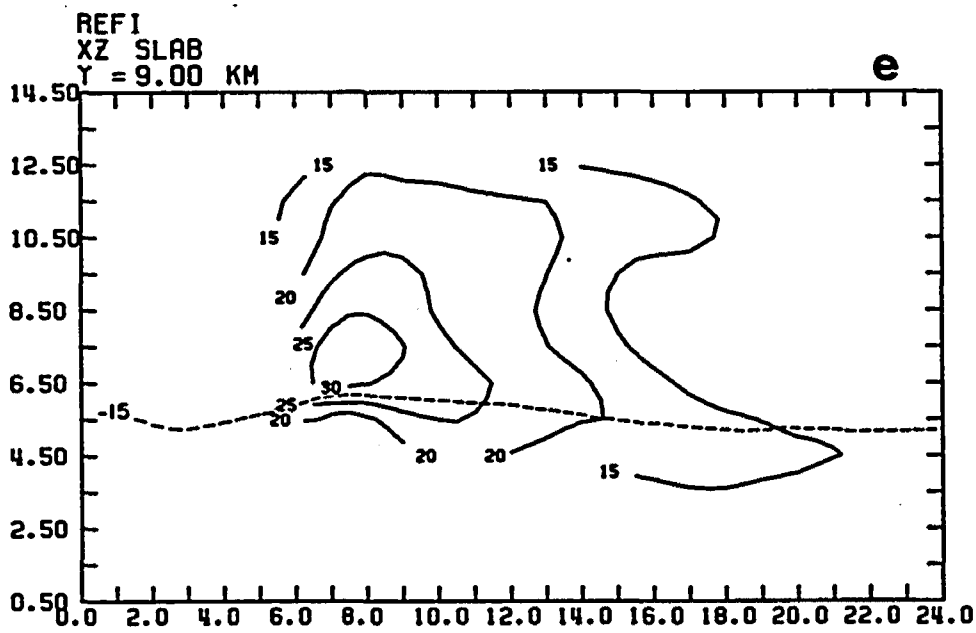

Fig. 4.7 (continued)

illustrates the reduced rate of cloud autoconversion to rain in the gamma model versus the Kessler model, as well as the tendency of the gamma model to produce more numerous, smaller rain drops in the early stages of coalescence (reduced radar cross section for a given mixing ratio). Neglect of the ice phase results in a temperature difference of order 0.1 C, which is within the retrieval noise level as concluded from Chapter III.

Additional microphysical sensitivites are illustrated in Fig. 4.8d-h. Comparing Fig. 4.8d, Fig. 4.8a (observations) and Fig. 4.5e (D_g = 0.3), the effect of increasing D_g is to reduce the upper reflectivity maximum below the observed value. This is due to the decrease in hail reflectivity and mixing ratio accompanying the reduced ice-hail conversion rate. Hail was probably present above 5.5 km, although none was reported at the ground. Ice reflectivities (not shown) correspondingly increase to nearly 40 dBZ. The optimal value of D_g may lie in the range of 3 - 5 mm. The effect of modifying the control model hail growth rate by imposing a constant ice density of 0.9 g cm^{-3}, shown in Fig. 4.8e, is to substantially increase the middle level reflectivity maximum to over 60 dBZ. The increased mean density is physically related to a larger growth rate. This larger growth rate leads to increased fallspeeds and a closer balance between sedimentation and vertical advection, further increasing hail mixing ratio. Although the representation of variable rime density in the current model is admittedly rather crude, it does permit a significantly and consistently better retrieval of radar reflectivity. Comparison of Fig. 4.8f and Fig. 4.5e indicates that the decrease of cloud droplet distribution width to simulate more

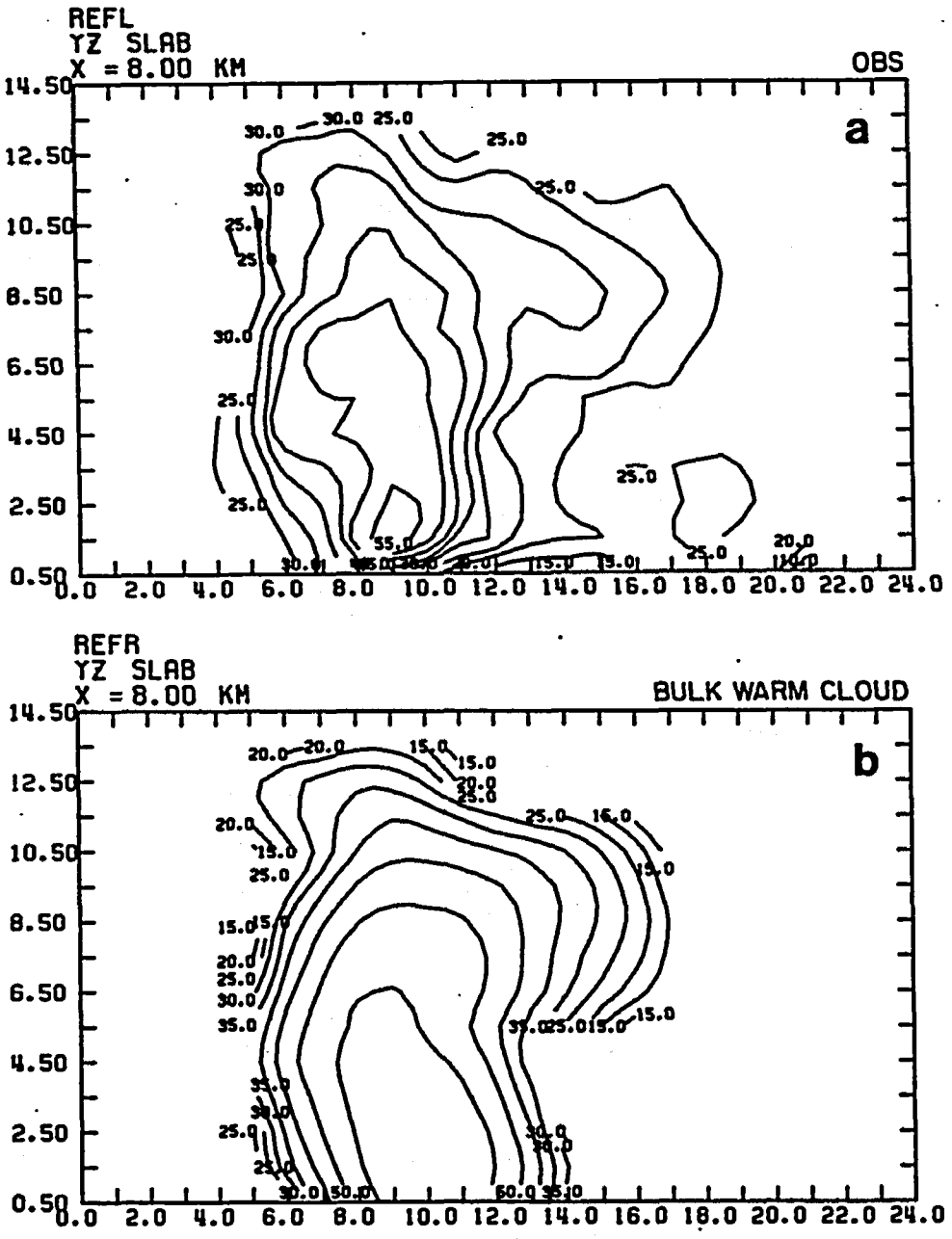

Fig. 4.8 Computed model total reflectivities as in Fig. 4.5e, but for results of sensitivity tests described in the text. Observed reflectivities are presented to facilitate model evaluation. Parts (a) through (h) are respectively the observed reflectivity as well as model reflectivity from the output of experiments 27-2 through 27-8. A label at upper right identifies a particular experiment.

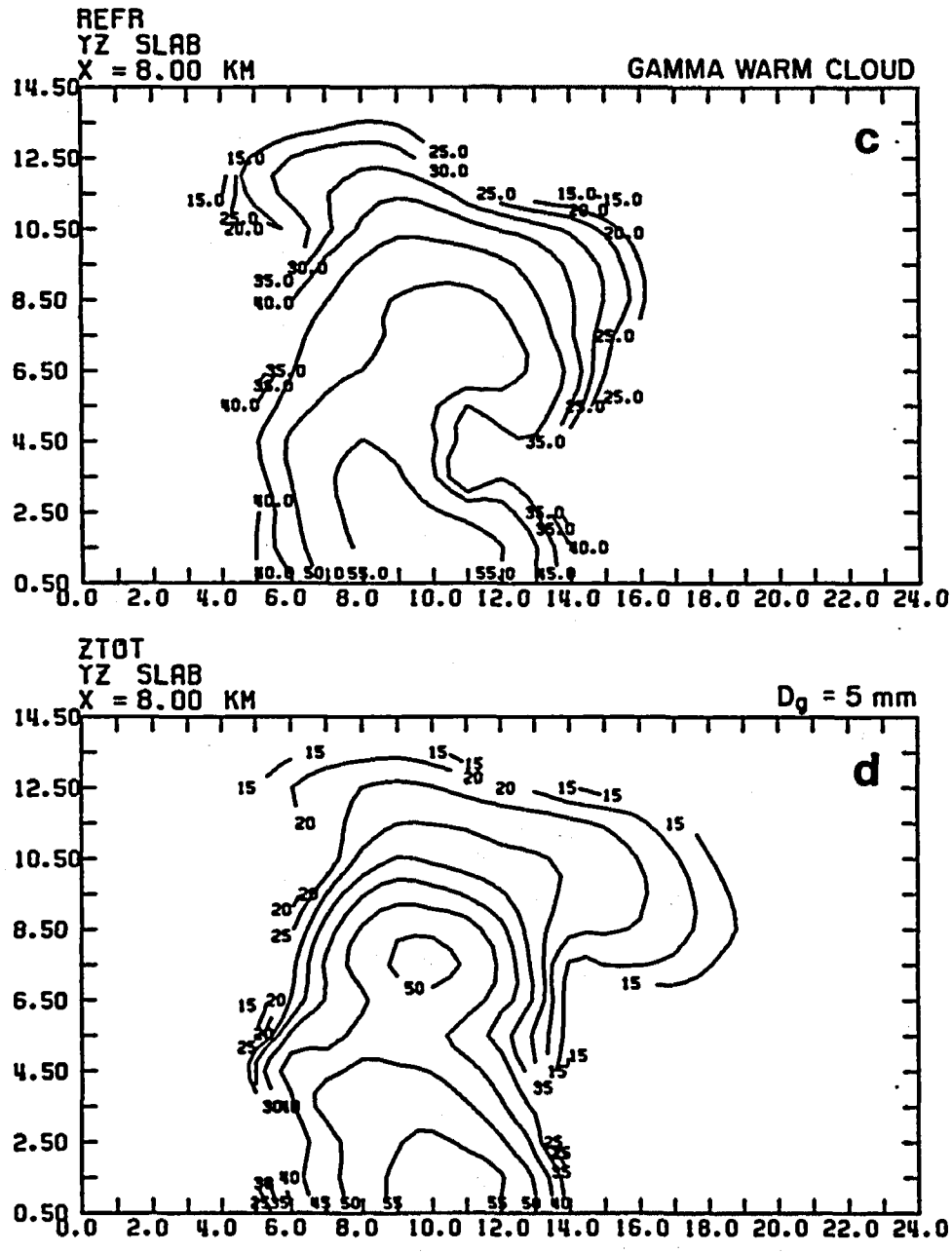

Fig. 4.8 (continued)

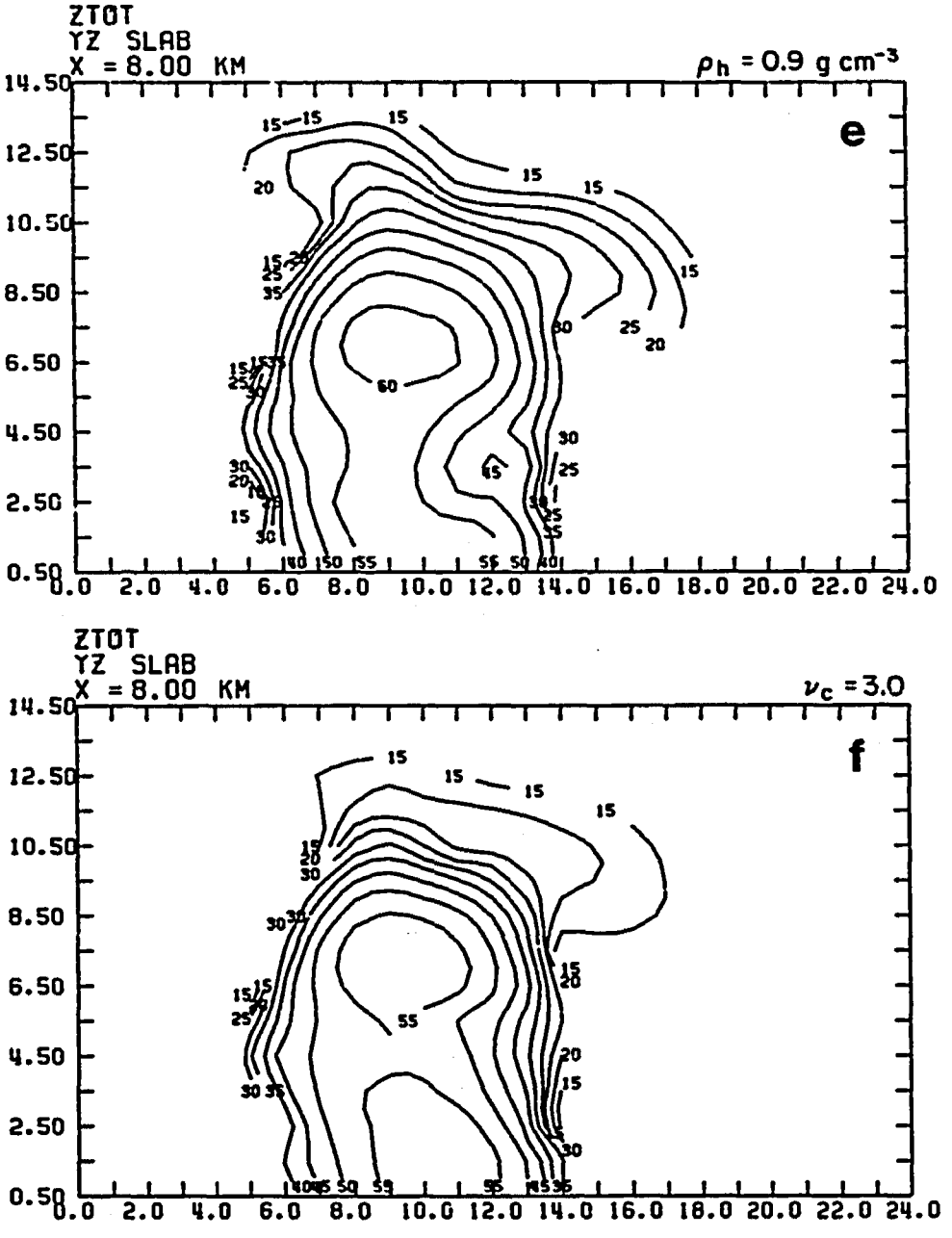

Fig. 4.8 (continued)

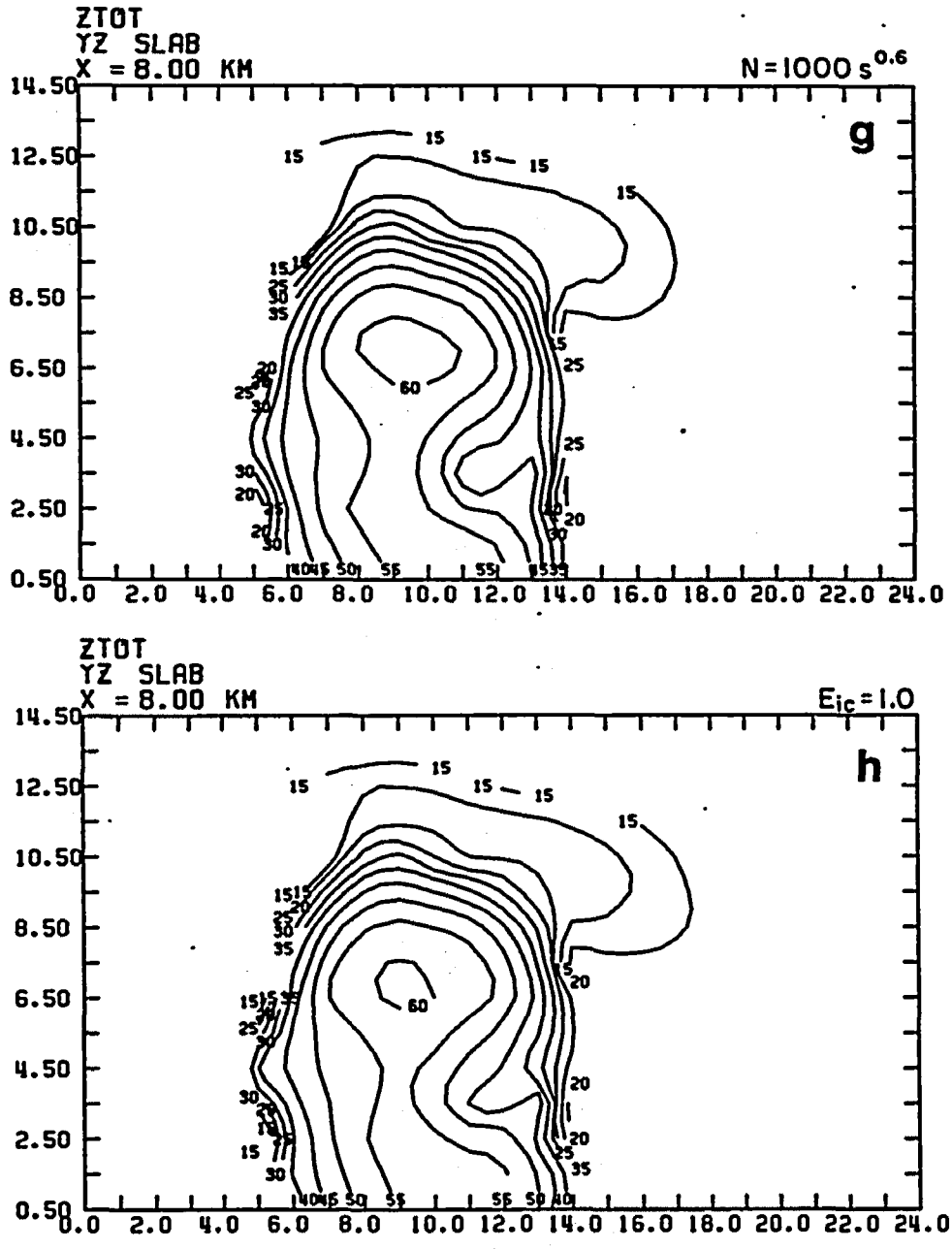

Fig. 4.8 (continued)

continental conditions has little noticeable effect on the retrieved precipitation fields. Additional test results (not shown) indicate that decreasing D_g from 0.3 cm to 0.1 cm, appears to over-accentuate the hail content by producing too rapid a transfer from precipitating ice to hail[1]. The decrease in cloud concentration in exp. 27-7 results in an increase in peak mean droplet diameter in the hail zone from 20 μm to 24 μm, which causes a 14% increase in the accretion rate. Fig. 4.8g shows the resulting increase in peak reflectivity to over 60 dBZ. Fig. 4.8h shows the peak reflectivities of over 60 dBZ from a doubling of the ice riming rate. Although the retrieved anvil reflectivities are generally lower than observed, the implied error in ice mixing ratio is probably of little practical significance. The most extreme changes in microphysics are observed to change only the magnitudes of relative maxima. The constancy of the overall echo configuration reflects the predominance of the fixed wind field effects.

In order to illustrate the effect of reducing the model geometry to two dimensions, such as might occur in the kinematic rainband model of Rutledge (1983) referred to in Chapter I, the control version of the model has been run in a vertical west-east cross-section identical to that depicted in Fig. 4.1 and used in Fig. 4.7. Velocities are as depicted in Fig. 4.3, except that the v component is set to zero for the slab test. Fig. 4.9 shows model output reflectivities in the two dimensional case, while Fig. 4.7a illustrates the three dimensional model output in the same cross section. The deep convective core is well

[1]A small value of D_g associates with a large fraction of the total ice mass with diameters exceeding D_g, hence a large transfer of ice to hail.

reproduced in two dimensions, but too much rain accumulates below 3.5 km and to the east of the vertical column x = 16 km. In particular, the observed reflectivity at (16.0, 0.5) compares favorably with the 3-D reflectivity (35 and 40 dBZ respectively) as opposed to the 50 dBZ secondary maximum in the 2-D case. This discrepancy is due mainly to the neglect of the 1-3 ms^{-1} v component in the stratiform precipitation region. Three space dimensions should be considered in cases where the storm relative wind changes direction with height, unless the normal gradient of precipitation content vanishes.

Verification of cloud model output with independent observations besides radar reflectivity, is highly desirable. The T-28 research aircraft was flying on 27 May, but unfortunately did not encounter any precipitation until one-half hour after the current Doppler data was collected, and then only in very minor amounts well outside of any active updrafts[1]. The NCAR Queen-Air flew along the southern inflow boundary of the model domain, well to the south of the storm. Hence no model verification is possible with this data. The NSSL surface network of SAM stations was also collecting data, and one station was apparently within the low level outflow of the Broxton storm. Additionally, the ARS rain gauge network had 6 stations in the vicinity of the storm.

Surface station models and ARS gauge locations, as well as horizontal Doppler winds and schematic model output fields at 0.5 km AGL, are shown in Fig. 4.10. Data at 1437 CST from stations BRX (Broxton), ANW, CNW and VSW are depicted by station models. Numbered dots indicate ARS

[1]Dr. Andrew Heymsfield and J. Parrish, NCAR, private communication (1983)

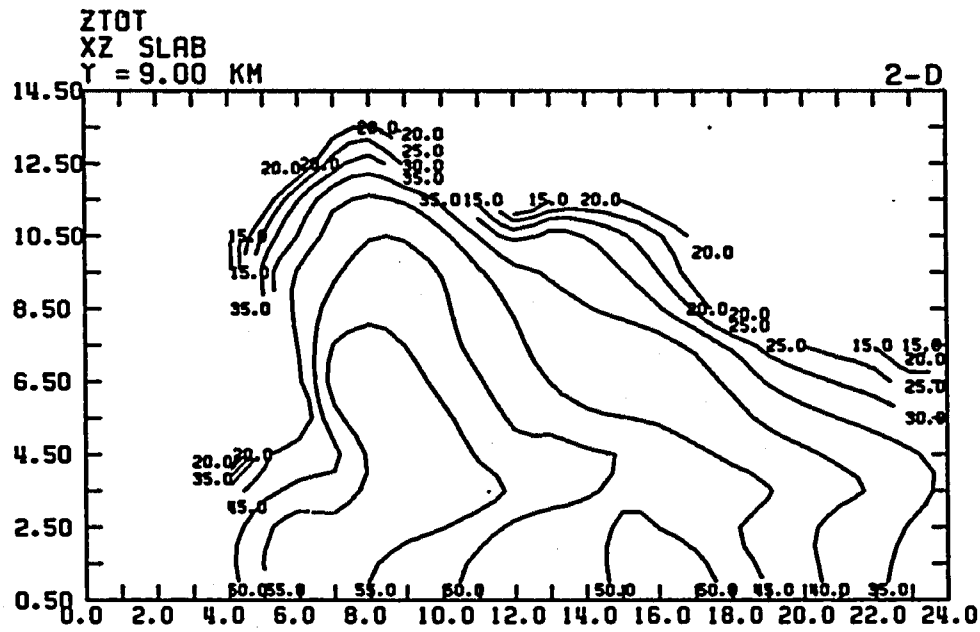

Fig. 4.9 Computed model output total reflectivity of slab model test referred to in text. Vertical west-east cross-section is oriented as in Fig. 4.7.

recording rain gauge station positions. Fig. 4.10 shows that the mesoscale boundary at 0.5 km, indicated by a bold dashed line, is located over BRX, although the surface boundary has moved north of BRX at the analysis time. The temperature at BRX is 19.8 C as compared to the 500 m model temperature of 19.3 C. Although no unique relation between surface and 500 m temperature exists in thunderstorm outflow, the implied boundary layer thermal stratification is consistent with a net 6 K increase in θ over the lowest 500 m. Such stratification has previously been observed behind the gust front surface boundary as determined by instrumented tall tower data in Oklahoma convection (Goff, 1975). The other surface sites are relatively unaffected by the convection, which appears to verify the extent of the envelope of contoured (solid line) 500 m temperature defect (C) as derived from the model. Cold outflow at BRX (with θ_e below 328 k) is consistent with the temperature in the rain-cooled downdraft in the vicinity of gridpoint (10,9). The diagnosis of a low θ_e value in the downdraft is consistent with classical models.

A comparison of ARS rain gauge measurements with 500 m model output rainfall rates is shown in Table 4.2. The mean and maximum rainfall rates (mm hr^{-1}) are derived from the strip chart recording from each station showing significant precipitation. Due to the small amount of total precipitation at gauge 129 and the use of a seven day trace at gauge 127, the mean and/or maximum rainfall rates could not be determined. As with the temperature comparisons, no unique relationship exists between surface and 500 m rainfall rate although qualitative comparisons are useful. The comparison between observations and model

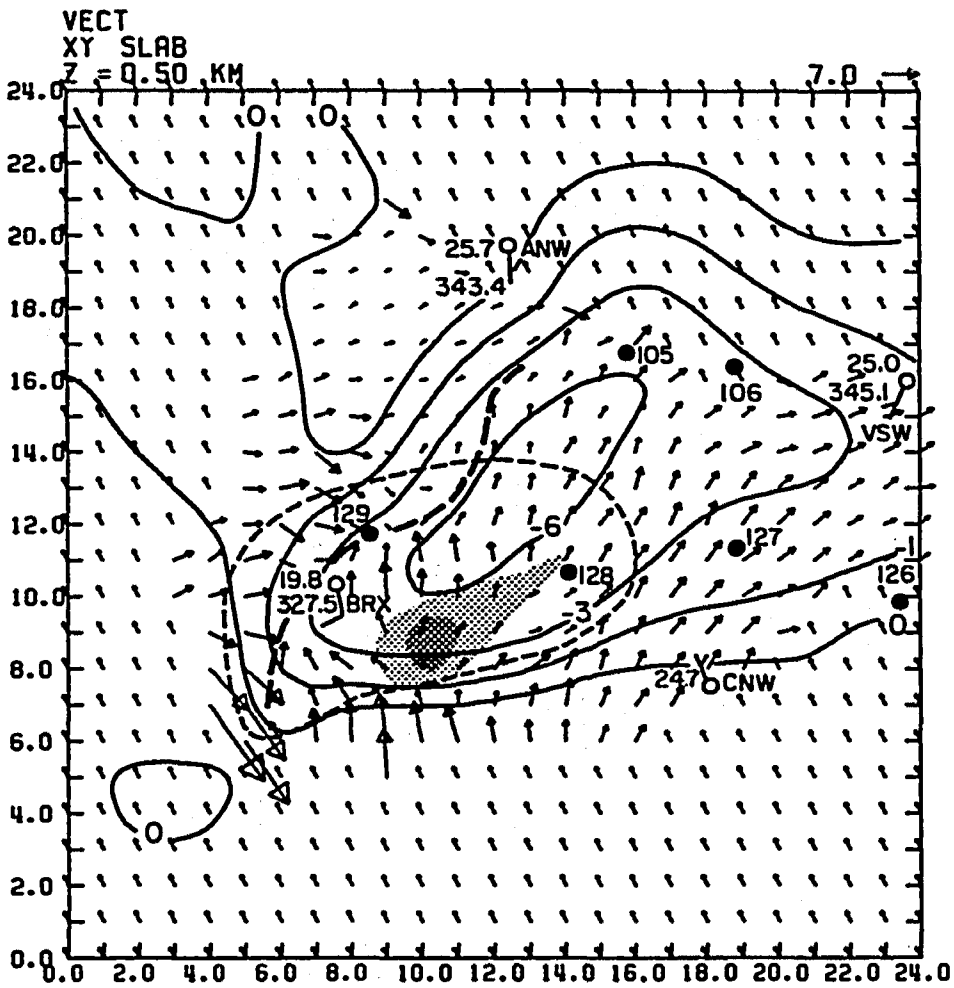

Fig. 4.10 Horizontal observed wind field at 500 m, with NSSL surface station models, ARS rain gauge locations, and selected model output included. Velocity scale is at upper right. Models for stations BRX, CNW, VSW, and ANW are indicated with wind barbs, air temperature (°C), and θ_e (°K). One full barb equals 5 ms^{-1}. Dots locate ARS gauge locations. A heavy dashed line indicates outflow boundary at 500 m, the solid contour shows temperature deviation from the environment (°C), and the small dashed line encloses the region of $q_r >$ 1 g kg^{-1}. Region of light stippling denotes 1.5 km $\theta_e <$ 330 K, while enclosed region of heavy stippling indicates $\theta_e <$ 328 K.

TABLE 4.2: Comparison of observed and modelled rainfall rates for case 27-1

ARS RAIN GAUGE NUMBER	24 HOUR ACCUMULATION (IN)	PRECIPITATION BEGAN	PRECIPITATION ENDED	RAINFALL RATE MEAN	RAINFALL RATE MAX	(mm hr^{-1}) MODEL	GRID
105	0.0	----	----	--	--	0	(10,17)
106	0.0	----	----	--	--	.22	(19,16)
126	0.0	----	----	--	--	.15	(24,10)
127	0.20	1425	1445	13	--	7	(18,11)
128	0.50	1425	1455	25	51	40	(14,11)
129	0.01	1440	1450	--	--	49	(8,12)

output is rather good, although gauge 129 did not record significant precipitation despite a significant model rainfall rate at that location. This is a result of the northward extension of the retrieved rain reflectivity area over the gust front (see Figs. 4.6a and 4.6d) and gauge 129, which is located within 1 km of the boundary near model gridpoint (8, 12, 0.5). The false spreading of the precipitation area to the north of the gust front may be due to low model spatial resolution, which could be improved. The gust front could have been propagating northward at this time, creating errors due to assumed steadiness. Due to internal consistency of model wind and water fields and the presence of significant analyzed updrafts ($w \sim V_r$) over grid point (8, 12, 0.5) and the ARS gauge (Fig. 4.2), the analyzed updrafts over the gust front are plausibly too extensive. This view is supported by the known smoothing effects of the analysis and by the good agreement between model and observations at the remaining sites, which are all outside of the region of strong convection where w errors are not a major factor. The areal extent of significant precipitation is in very good agreement with the observed and modelled low level temperature defect (Fig. 4.10).

4.3 Model tests with 28 May 1977 data

These tests utilize dual Doppler wind fields and a composite of the 1330 and 1641 EMC proximity soundings to assist in retrieving temperature and water substance in the Wynnewood storm, which occurred in south central Oklahoma on 28 May 1977. Additional soundings are not available in order to characterize the mesoscale environment, although Elmore City (EMC) is only 10 km west of the Wynnewood storm. For convenience in the

current sensitivity tests, the control version of the full warm/cold cloud model in the 27 May 1979 case is used here. The microphysical sensitivities in this case may not be the same as those in the previous case. Future research should pursue the generalization of model microphysics. Inspection of the 1716 Doppler wind analysis to be used as input to the model, reveals certain fundamental discrepancies between the derived fields and conceptual flow models. The effect of random errors on the input wind field has been explored in the proxy data tests, but the model response to systematic or bias errors is unknown. The primary goal of these sensitivity tests is to provide a minimal subjective correction to the derived wind field, which improves the retrieved reflectivities. Surface station and aircraft penetration observations for the cell in question have not been collected, so that the model verification must rely on observed reflectivity. Norman and CHILL Doppler reflectivities differ in this case by as much as 15 dBZ (7 dBZ on the average), introducing considerable uncertainty into the model verification. The Wynnewood storm produced hail up to 5 cm in diameter, some of which was collected in real time within the precipitation core. These ancillary hail observations evoke interest in the ability of the model to represent hail growth mechanisms, although the observations are far too limited to be of value for quantitative verification of size distributions.[1]

[1]The most reliable observed hail distribution is based on a 20 min sample. This period corresponds to a space resolution of 6 km, which is poor compared to the model output data.

In these tests, the wind fields are modified by extrapolation beyond the analysis domain. A feeder cell west of the cell to be studied, is providing hail embryos through the upwind or inflow boundary of the model domain. This role of the feeder cell has been determined in a study of large hail growth in the Wynnewood storm using a Lagrangian hail growth model (Ziegler et al., 1983). For simplicity, the hail mixing ratio above 3.5 km on the inflow boundary is fixed at a value prescribed from observed reflectivity and a standard Z-q relationship. In an analogous fashion, the rain mixing ratio is specified on the same boundary and below 3.5 km. The fixed drop concentration is computed by assuming a mean drop diameter of 1 mm for the gamma distribution. The model is integrated forward in time for 80 minutes to a quasi-steady state. The stronger circulations in this case compared to the 27 May case, require a 5 s model time step to maintain computational stability. The model domain is the same size as in the 27 May case, but the grid origin is located at (20,-82, 0.5) relative to the Norman radar.

The observed wind field at the 6.5 km level is shown in Fig. 4.11. Vertical cross-section orientations to be referred to later, are indicated by lines. The graphic conventions are the same here as those used in the 27 May case, except that lightly stippled regions indicate updraft speeds between 10 and 25 ms^{-1} and downdrafts less than -10 ms^{-1} are indicated by hatching. Barrier flow around a cyclonically rotating main updraft are notable velocity features, although significant vertical motion is present in regions devoid of pronounced horizontal flow perturbations. The vertical motions apart from the main updraft

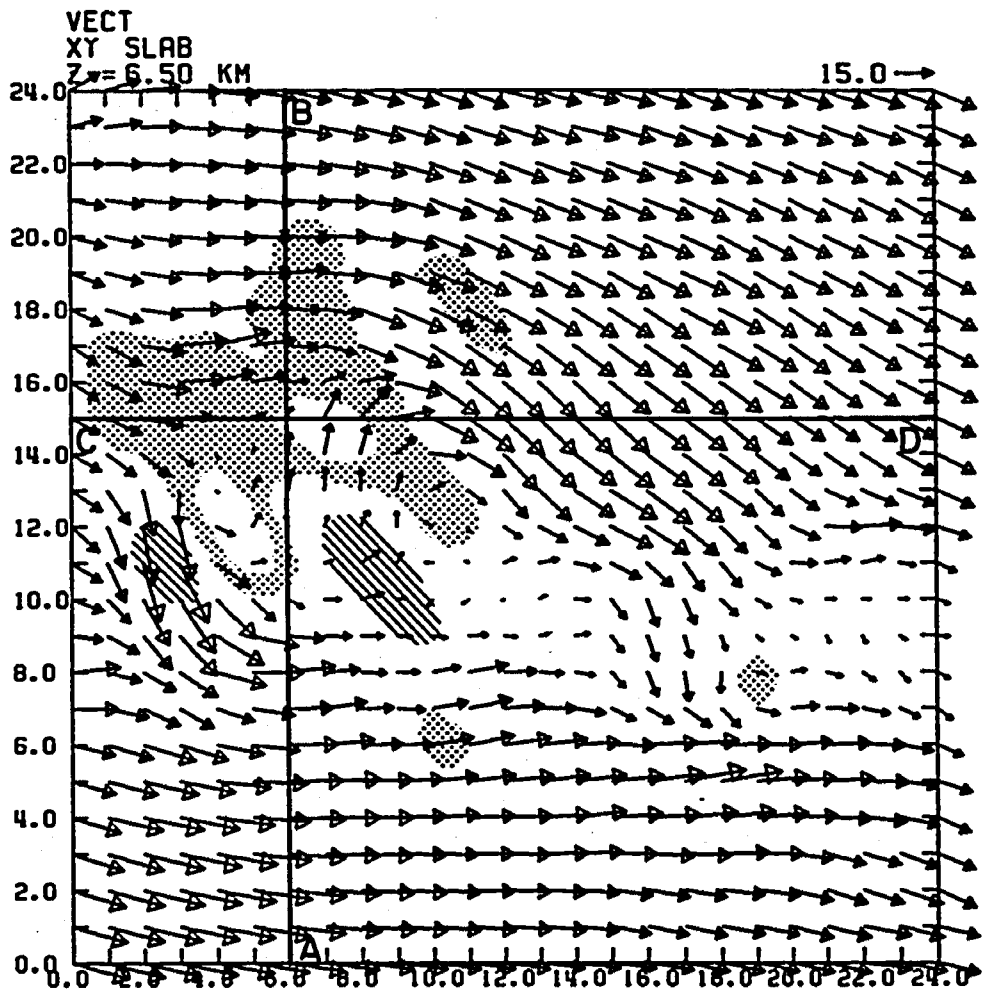

Fig. 4.11 Observed horizontal wind field at the 6.5 km level, at 1716 on 28 May 1977. Velocity scale is indicated at upper right. Horizontal coordinate is west-east distance (1.0 km grid spacing) while vertical coordinate is south-north distance. Lightly stippled regions indicate updraft speeds between 10 and 25 ms^{-1}, while downdrafts exceeding -10 ms^{-1} are indicated by hatching. Bold solid lines denote the orientation of cross-sections AB and CD to be referred to in the text.

should be as much as one order of magnitude weaker, in part from consideration of classical airflow models but mainly from inspection of the dynamically simulated wind fields due to Wilhelmson and Klemp (1978). These extraneous vertical motions produce readily discernable artifacts in the reflectivity field, thus raising the possibility that the model can be used to find regions of large errors in the vertical motion analysis.

The observed wind fields are further illustrated by a vertical south-north cross-section in Fig. 4.12, whose location is indicated in Fig. 4.11. Stippling denotes a region of westerlies between 15 and 20 ms^{-1} with unstippled closed regions indicating higher values. Hatched regions indicate easterlies exceeding 7 ms^{-1}. The maximum updraft in this plane is 37 ms^{-1} at (15.0, 8.5). The updraft is bifurcated, with the split occurring 2 km south of the peak updraft and extending through the cloud depth. This feature is possibly of spurious origin because it does not change to a strong updraft at high levels (see vertical cross-section showing properties of a splitting thunderstorm in Klemp and Wilhelmson, 1978). Westerly wind maxima in excess of 20 ms^{-1} flank the updraft in the vicinity of 6.5 km AGL, with a shallow layer of easterly winds beneath the updraft at 0.5 km AGL. Time lapse movies from NSSL indicate that the penetrative convection associated with the updraft core has exceeded 16 km in altitude, while the wind analysis ends at 14.5 km. The vertical motion is set to zero at 15 km in this analysis, which may be too small and has the result of weakening updrafts in the upper third of the analysis domain.

A vertical west-east cross section, oriented as in Fig. 4.11, is shown in Fig. 4.13. Light stippling denotes a v component between 10 and 15 ms^{-1} while hatching denotes a v component less than -10 ms^{-1}. The strong, erect updraft centered at x = 6 km is in the storm core. A layer of v component exceeds 10 ms^{-1} near the ground on the downwind side of the main updraft. A region of large v component is also found downstream of the updraft core in middle levels.

Two model tests have been performed using the 1716 wind analysis. These are listed in Table 4.3 along with a brief description of pertinent model properties. In the second case, some v and w wind components are subjectively adjusted as a sensitivity test. The results of the first test are described before specifying the wind field modifications of the second test.

A horizontal section of modelled and observed reflectivites at the 6.5 km level in the observed wind case is illustrated in Fig. 4.14. The model correctly retrieves the 60 dBZ core at (6.0, 14.0), and produces an echo depression at (4.0, 13.0) similar to the bounded weak echo region in the observations at the same location. This feature is due to the presence of a strong updraft (Fig. 4.11) which retards the growth and accumulation of large particles. In high resolution observations (not shown), the BWER is only about 500 m in diameter. The model is capable of resolving this small feature with a decrease in grid size, although the wind data is not resolved on so fine a scale. The crescent shape of the core as it curves eastward is well reproduced in the model, although the reflectivity maximum at (12.0, 15.0) is not observed. This feature is due primarily to hail falling out of the precipitation core

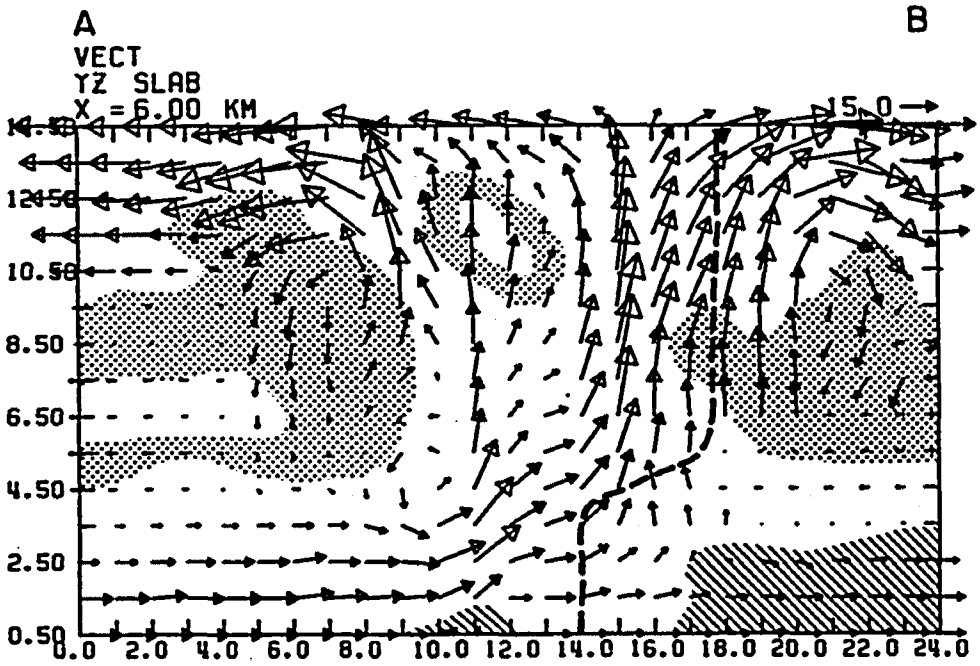

Fig. 4.12 Observed wind field in the vertical south-north cross-section AB, as oriented in Fig. 4.11. Velocity scale is indicated at upper right. Stippling denotes westerlies between 15 and 20 ms^{-1}, with unstippled closed regions indicating higher values. Hatched regions indicate westerlies less than -7 ms^{-1}. In experiment 28-2, updrafts at each grid point to the right of the dashed line are zeroed.

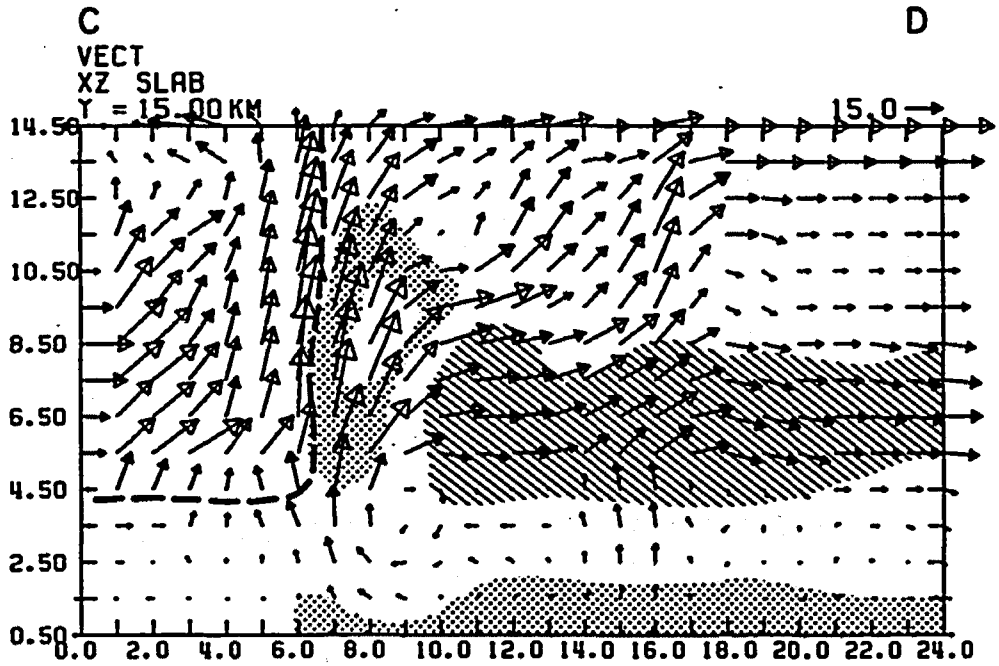

Fig. 4.13 Same as in Fig. 4.12, but for vertical west-east cross-section CD. Light stippling denotes a v component between 10 and 15 ms^{-1}, while hatching denotes a v component less than -10 ms^{-1}. In experiment 28-2, updrafts to the right of the dashed line are reduced by 90% and zeroed below the dashed line.

TABLE 4.3: Case Studies (1716 CST, 28 May 1977)

EXPERIMENT	DESCRIPTION
28-1	Warm/cold cloud (same as Exp. 27-1)
28-2	Warm/cold cloud, modify v,w field

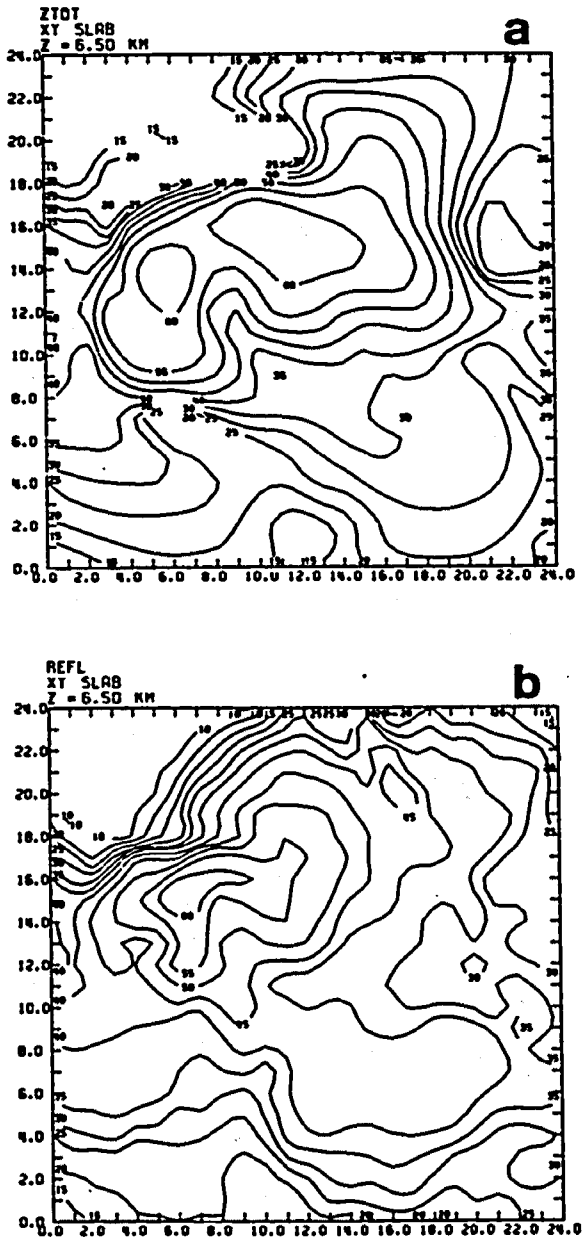

Fig. 4.14 Horizontal field of modelled (a) and observed (b) reflectivities at 6.5 km, from the output of experiment 28-1. Corresponding velocities appear in Fig. 4.11. Contour interval is 5 dBZ.

further west, with subsequent accumulation and growth in the (cloudy) updraft at (8.0, 15.0). Because of this simple cause-effect relationship, this secondary updraft is likely of spurious origin. The echo trough at (9.0, 12.0) relates to the downdraft and is well reproduced.

The nature of the spurious echo maximum is further explained by inspection of the west-east vertical cross section of modelled and observed reflectivities in Fig. 4.15. The main core at (6,7.5) is well reproduced, as is the downward extension of the core to (5,1.5). The reflectivity maximum aloft is clearly related to the updraft core (Fig. 4.13). The false maximum between (12,1.5) and (12,8.5) is seen as an eastward extension of the core, while observed reflectivity shows a trough at (8,7.5) and a rather narrow core in the horizontal. The spurious updrafts cancel sedimentation, and strong westerly winds carry suspended precipitation horizontally in the model. An additional manifestation of the spurious updraft is the precipitation minimum and weak echo region in the vicinity of (8,4.5) in the model, a region where observed precipitation is evidently encouraged to fall out and form a low level reflectivity maximum. Since observed reflectivities near the updraft summit at (6,14.5) are much higher than modelled reflectivity, the vertical advection (and hence the kinematic upper boundary condition) should probably be locally increased.

Additional clues to the presence of wind analysis errors are evident from inspection of a vertical south-north cross section of modelled and observed reflectivities in Fig. 4.16. The overall echo configuration including an elevated core at (15,7.5), anvil reflectivity plumes at (8,11.5) and (20,12.5), rear flank gradient at (17,7.5), and slanted

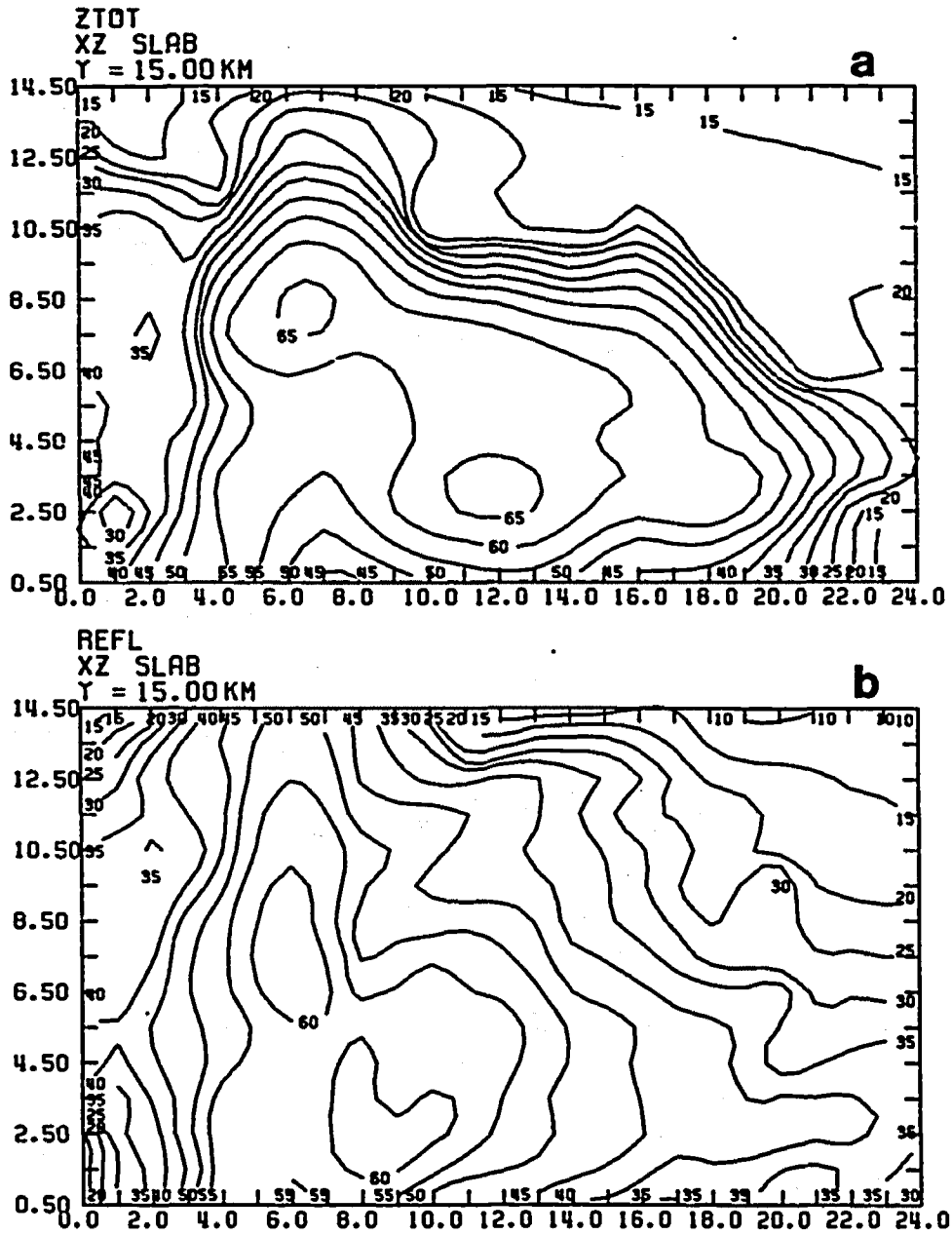

Fig. 4.15 Same as in Fig. 4.14, but in vertical cross-section CD as oriented in Fig. 4.11.

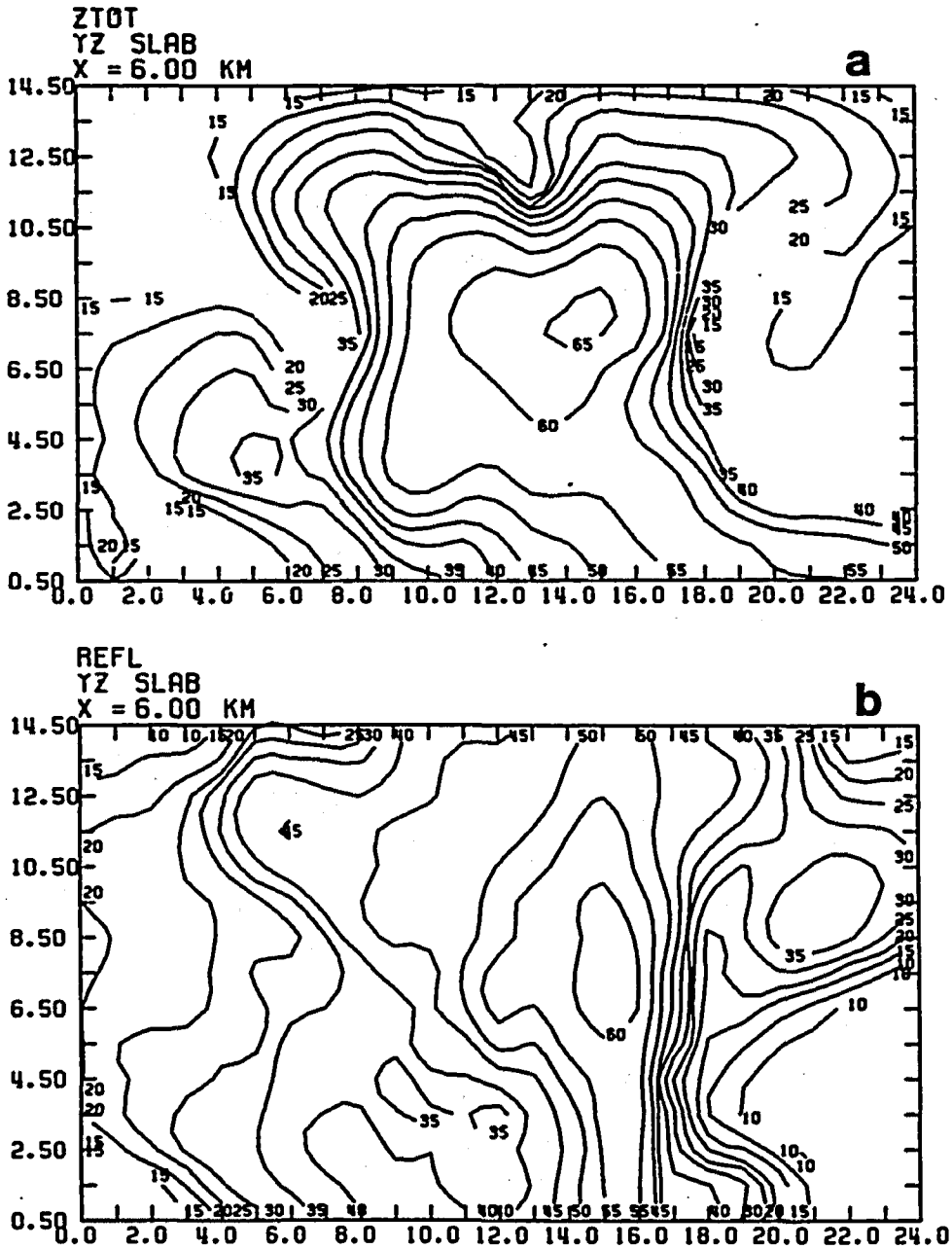

Fig. 4.16 Same as in Fig. 4.14, but in vertical cross-section AB as oriented in Fig. 4.11.

precipitation debris patterns at (6,2.5) and (19,1.5), are all well retrieved. The updraft bifurcation, pointed out earlier in the discussion of Fig. 4.12, produces an echo bifurcation at (13,11.5) that is not observed. The same velocity feature at low levels allows the partial collapse of the observed BWER. Elimination of the updraft bifurcation would probably eliminate the spurious echo pattern through increased vertical advection. The 45° tilt of the low level modelled precipitation core is obviously spurious, and is due to a coincidence of strong updrafts and southerly flow across the precipitation core. The flow pattern in the erect observed precipitation core is not consistent with classical models or the output of dynamic models (see for example Fig. 4.14a of Wilhelmson and Klemp, 1978), which colocate downdrafts and a horizontal flow reversal with the precipitation shaft. Horizontal flow north of the core evidently reverts to a southerly direction, because the outflow of precipitation to the north at low levels is correctly retrieved.

In order to test whether the errors proposed above are plausible, experiment 2 is conducted using a subjectively modified wind field as illustrated by Fig. 4.11, Fig. 4.12, and Fig. 4.13. In the horizontal section at 6.5 km (Fig. 4.11), updrafts to the east of the cross-section AB have been reduced below the average fallspeed of hail to avoid spuriously high reflectivities due to large hail mixing ratios. For x greater than or equal to 8, the observed updrafts are reduced by 90%. For y greater than or equal to 18, observed updrafts are set to zero. In the vertical south-north cross-section (Fig. 4.12), updrafts at each gridpoint to the right (north) of the heavy dashed area are set to zero

to allow precipitation fallout. Additionally, the positive v component between y = 14 and y = 17 and below z = 4.5 is set to zero in order to crudely simulate a velocity reversal in the precipitation core. In the vertical west-east cross-section (Fig. 4.13), updrafts to the right (east) of the heavy dashed line are reduced by 90% and zeroed below that line. Because the velocity adjustments are so large at some points, the subjectively modified updrafts could with equal plausibility be considered downdrafts. Subjectively adjusted winds are not readjusted to satisfy mass continuity. Velocity divergence plays a minor role in the model continuity equations, compared to the role of velocity itself in the advection terms. A desirable improvement in this decision process would be to optimize the adjustment, in other words to maximize agreement of modelled and observed reflectivity with minimal wind adjustment. A simple subjective modification seems more appropriate here.

The retrieved model reflectivities for the modified wind case in the same cross-sections as Fig. 4.14, Fig. 4.15 and Fig. 4.16, are presented in Figs. 4.17a through c respectively. These may be compared with observed reflectivities shown in panel b of the three former figures. Inspection of Fig. 4.17a reveals that the spurious reflectivity maximum at (12,15) has vanished due to weakening of the eastern updraft core. The anticyclonically curving crescent shaped core at (7,15) is clearly retrieved. Due to reduced hail content east of the primary core, the distinctive V-shape of the observed echo emerges in the retrieval. Fig. 4.17b reveals that increased hail fallout results in a more steeply sloped echo to the east of the core and a westward contraction of the low level echo extent. The modelled local maximum

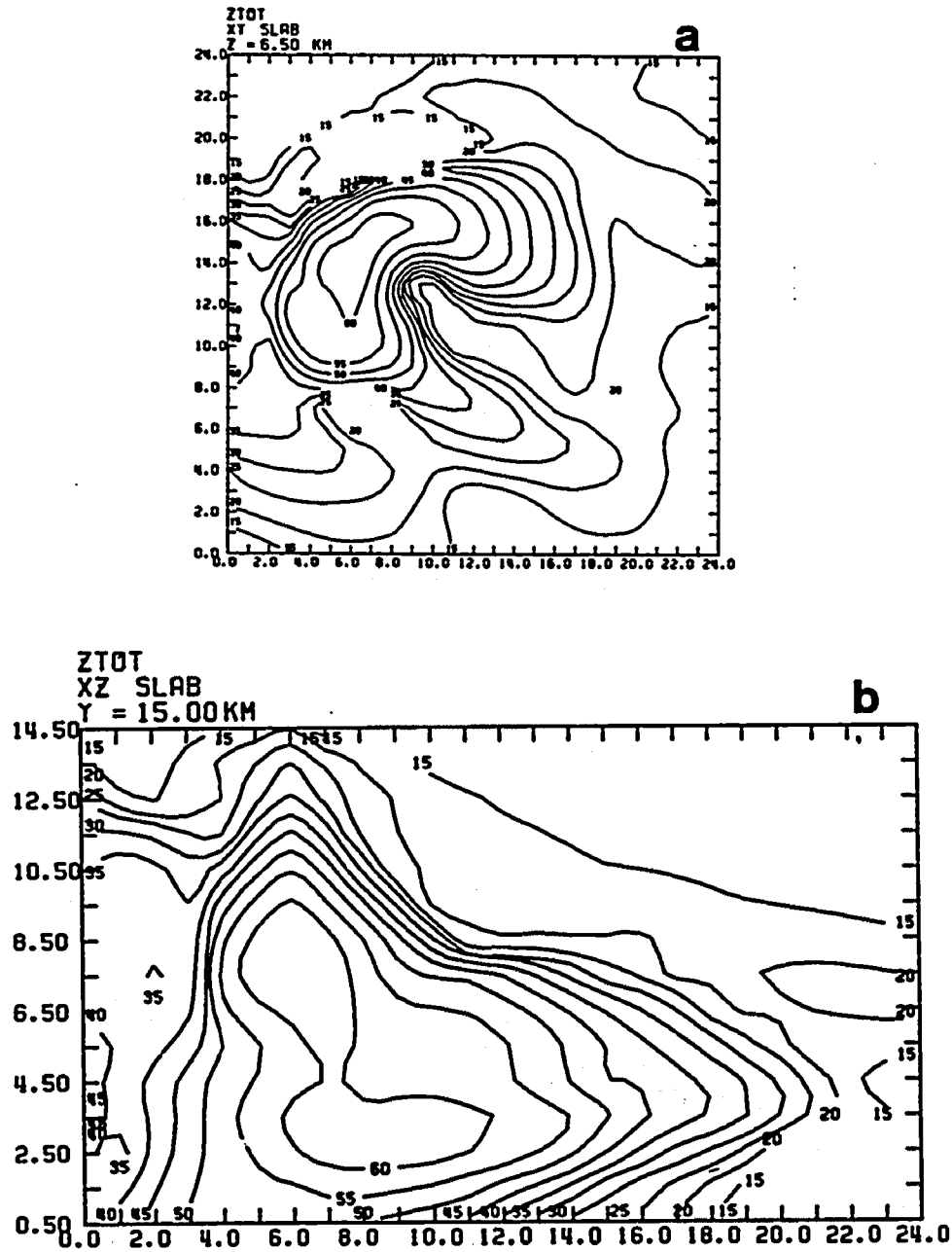

Fig. 4.17 Computed model total reflectivities for experiment 28-2. Panel (a) corresponds to Fig. 4.14, (b) corresponds to Fig. 4.15, and (c) corresponds to Fig. 4.16. Contour interval is 5 dBZ.

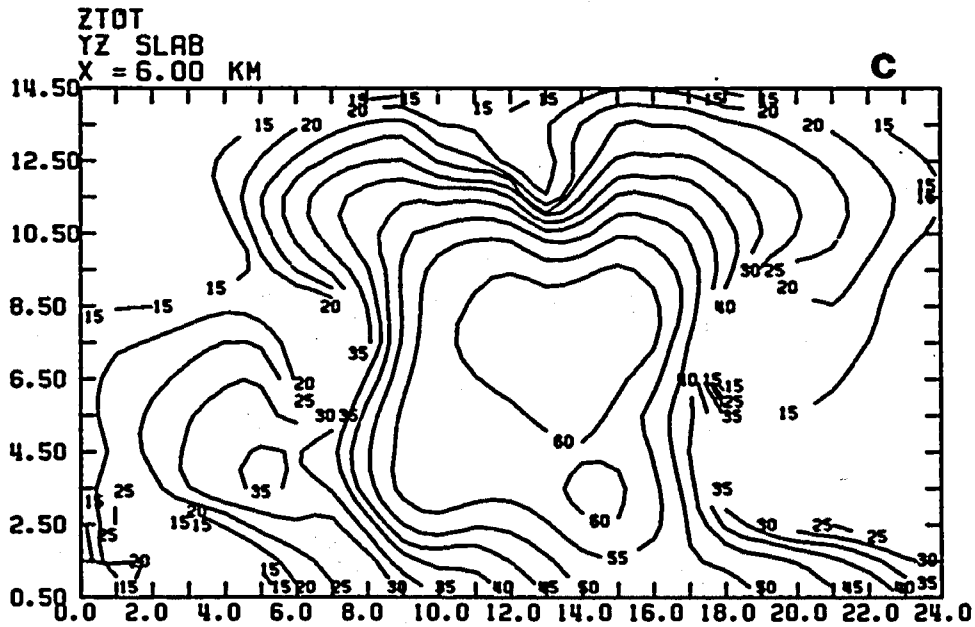

Fig. 4.17 (continued)

reflectivity of 60 dBZ at (9,3.5) is in good agreement with the 59 dBZ observed reflectivity, and the observed 60 dBZ region surrounding this point is also reproduced. The spurious BWER noted in Fig. 4.15a at (8,3.5) has been filled as observed. Comparing Fig. 4.17c with Fig. 4.16, the inclination of the low level core is much closer to vertical, as observed. A velocity sign change probably exists near (14,0.5), so that precipitation is advected from the north and the gradient futher steepened.

In conclusion, a simple and subjective wind field modification consistent with classical and dynamic models, has resulted in significant improvement in the verification of model reflectivity. The inconsistencies noted between retrieved and observed reflectivity appear to be largely due to kinematic factors, although approximate microphysical processes undoubtedly contribute to retrieval errors. As a logical extension of the results of Chapter III which established the importance of advection processes, it is further concluded that large non-random errors in the wind field may be important. Model reflectivities provide evidence of the degree and location of radar sampling errors such as beam smoothing, poor sampling of low-level divergence, differing resolutions provided by each radar, and systematic range/azimuth errors of the radar gate locations[1].

[1]The reflectivity fields from the Norman and CHILL radars have the same configuration at a given level, but are displaced relative to each other. A related error of radial velocity could conceivably produce severely biased vector velocity and divergence fields.

4.4 Precipitation growth rates

Model output from the experiments 27-1 and 28-2 has been used to diagnose instantaneous precipitation growth rates for these cases. The procedure used is to run the cloud model for one time step, followed by printing out and plotting of the growth rates without subsequent integration in time. The goal is to establish the relative magnitudes of the processes and the spatial arrangements of the predominant processes within the clouds. The precipitation development during model integration is described. The deductive capabilities of the model are illustrated by a brief discussion of the hail growth process in the 28 May case.

The characteristic orders of magnitude of precipitation rates are illustrated by the composited results of the 27 May 1979 and 28 May 1977 model integrations. Table 4.4 lists major microphysical and kinematic processes affecting the cloud, rain, hail, and ice mixing ratios. The typical magnitudes of warm cloud thermodynamic processes in deep convection have been discussed in Chapter III. Typical precipitation processes are grouped in columns according to their rates which are listed at the top of each column in Table 4.4. The water cycle in mature deep convective clouds is dominated by the flow of water substance from the vapor phase to the various hydrometeors via condensation, conversion and accretion processes. A key finding is the dominance of advection, sedimentation and diffusion processes in the spatial redistribution of existing water substance. This result explains and confirms the close relationships between wind and water fields that provide the foundation of the classical storm models

TABLE 4.4: Characteristic orders of magnitude of precipitation rate ($gg^{-1}s^{-1}$). Composite of 28 May 1977 and 27 May 1979 cases. Rates are diagnosed directly from model output of cases 27-1 and 28-2, that are described in the text.

$\sim 10^{-5}$	$\sim 10^{-6}$	$\lesssim 10^{-7}$
condensation	rain evaporation	cloud self-collection
rain accretion of cloud	hail accretion of cloud	hail accretion of cloud
rain freezing	(dry mode)	(wet mode)
rain sedimentation	ice accretion of cloud	hail accretion of ice
hail melting	ice sublimation	ice nucleation
hail sedimentation	ice melting	ice deposition
ice-hail conversion	ice sedimentation	
cloud freezing	ice horizontal advection	
cloud ice sublimation		
rain, hail horizontal advection		
rain, hail, ice vertical advection		
rain, hail, ice diffusion		

discussed in Chapter I. The fact that significant variation of cloud microphysics does not result in significant changes of the overall modelled echo configuration in the 27 May 1979 case is explained by the relative importance of the kinematic effects.

An important conclusion from Table 4.4 is that the magnitudes of the various accretion and ice nucleation/deposition precipitation mechanisims show significant differences. The rain accretion of cloud is greater by one order of magnitude than hail or ice accretion of cloud, despite similar characteristic mixing ratios. The sum of hail and ice accretion of cloud approaches the order of rain accretion, so that cold cloud accretion processes are nonetheless important. These relationships are due to the much lower concentration of hail (counteracting the high fallspeed) versus rain; and the much lower fallspeed of ice than rain (despite similar concentrations). An important consequence of the difference in accretion rates is that cloud mixing ratios in the rain precipitation core are of order 0.1 g kg^{-1}, while cloud mixing ratios in the ice portion of the core are of order 1 g kg^{-1}. This increase of cloud with height in the precipitation-filled updraft provides a vertical advective tendency which, upon combination with relatively weak ice/hail accretion rates, produces a balance with cloud condensation. The accretion process appears to be a much more efficient precipitation mechanism than the ice nucleation/deposition process. The model suggests that large particle recirculation and sedimentation may dominate primary ice nucleation in updraft cores. Heymsfield et al. (1979) have previously speculated on this possibility.

The model calculations in the 28 May case indicate that hail distribution mean diameters in the precipitation core typically range from 0.5 cm to 0.8 cm, while the threshold diameter for onset of wet growth (Appendix D.3) is above 1.8 cm within the same region. Hence, the hail distribution is dominated by dry growth. This suggests that low density riming may be an important effect, and explains why bulk wet growth rates are small compared to the dry growth rates (see Table 4.4).

The spatial distributions of various microphysical processes for the 28 May 1977 and 27 May 1979 cases are illustrated schematically in Fig. 4.18. These vertical west-east cross-sections through the cloud core depict regions of cloud self-collection (cross-hatched), the combined rain, hail and ice accretion of cloud (left-slanted hatching), rain evaporation (right-slanted hatching), and cloud condensation (heavy dashed outline). Accretion rates are lumped together for ease of presentation with little loss of generality, because rain and ice/hail accretion are essentially separated by the -15° C temperature surface with little overlap. Hail and ice accretion are coincident and of roughly the same magnitude. Hypothetical trajectories of cloud droplets (labelled C), rain drops (R), hail (H), and ice crystals (I) are also shown, as are selected isotherms (fine dashed lines). These estimates are based on the retrieved mixing ratios. On May 28 (Fig. 4.18a), cloud is converted by coalescence to small raindrops only on the eastern side of the main updraft. Cloud amounts are reduced mainly by rain accretion, while the mean droplet diameter is relatively large and the magnitude of the collection kernel amenable to coalescence. Cloud droplet growth is accelerated through a reduced droplet concentration with a

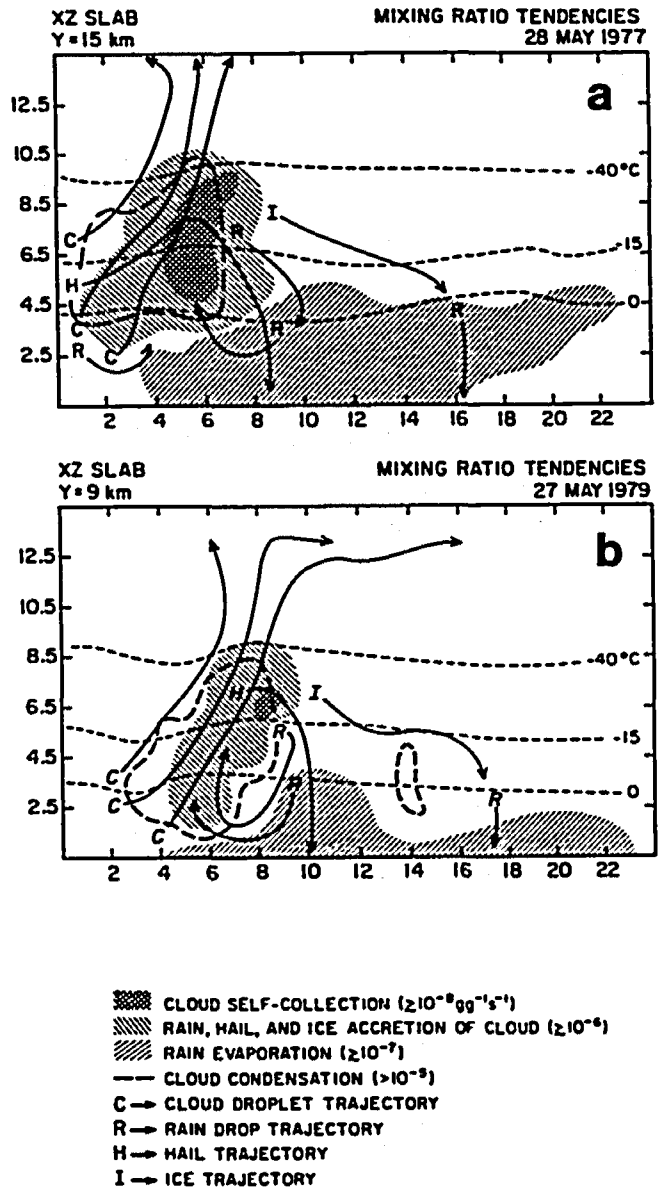

Fig. 4.18 Vertical west-east cross-sections schematically depicting selected microphysical processes in experiments 28-2(a) and 27-1(b). The sections selected in (a) and (b) correspond to the vertical sections CD, as oriented in Fig. 4.11 and Fig. 4.1 respectively. Hypothetical individual particle trajectories are included for reference. Thin dashed lines represent selected isotherms (°C). The key explains the various features.

fixed condensation rate. Little or no autoconversion occurs in the western half of the updraft because the cloud droplets there are too small ($D < 15\ \mu m$). The path of a hypothetical autoconverted raindrop initiated at (7,7.5), is recirculated in low levels back into the base of the main updraft to proceed with rapid accretion growth. Raindrops injected at (1,2.5) and produced by precipitation debris from the feeder cell west of the main updraft, are also ingested into the main updraft followed by rapid accretion growth. Hail embryo particles originating in the feeder cell and injected at (1,5.5) are carried through the main updraft, and experience rapid growth by accretion. These hailstones fall out of the cloud to the east of the main updraft and do not recycle. Drops originating from some of the melting hail near the melting level at (9,3.5), are also recycled back into the updraft base. Ice crystals outside the main updraft at (9,7) are carried to the east as they slowly descend, eventually reaching the melting level and producing drops too far downstream from the updraft to be recirculated. The mixing ratio and concentration of recycling raindrops is modified by low level evaporation. Uncollected cloud droplets are carried rapidly upward above the -40°C level to supply water substance to the storm anvil. The flow of water substance on 27 May (Fig. 4.18b) is analogous to the 28 May case, being dominated by the accretion transfer from cloud to hydrometeors. In this case, the lack of hydrometeor injection from a feeder cell upstream contributes to a significantly weaker echo core. The two convective cells studied here are in their mature phase, characterized by intense precipitation cores where accretion predominates.

The ice nucleation/deposition and cloud autoconversion processes are relatively important in the early stages of cloud development in the model, before hydrometeor content progresses to the point where accretion predominates. This observation is in accord with the conclusions of Dye et al. (1974) regarding precipitation formation in Colorado convection.

In the control case 27-1, additional model data (not shown) shows that a rain reflectivity first echo forms 15 minutes after the start of the model integration in the immediate vicinity of gridpoint (8,9,4.5). The 2 dBz echo is located on the interface of the updraft and downdraft, where the recycling of small precipitation particles is favored. The echo intensity rises to 28 dBz at 16 minutes and 35 dBz at 17 minutes. Browning and Atlas (1965) observed similar intensification rates in Oklahoma. Cloud droplet mean diameter increases by condensation from 6 μm at cloud base to 14 μm at 4.5 km, which is below the 15 μm diameter threshold for onset of autoconversion. Ice crystals nucleate above the freezing level and grow by vapor diffusion and cloud collection, acquiring sufficient mass for the distribution mean diameter to exceed 100 μm. These ice particles are low in concentration, with typical values of .1 l^{-1} at 4.5 km and 1.0 l^{-1} at 6.5 km. These particles apparently recycle along the downwind side of the updraft, descend below the freezing level, and melt to form drizzle - sized rain drops. These 100 μm drops are subsequently entrained into the updraft below the freezing level, and grow rapidly by accretion of cloud as they rise to the 4.5 km level. The warm cloud coalescence model integrations of Berry and Reinhardt (1974d) clearly illustrate the destabilizing effect

of the injection of drizzle drops into cloud (see their Fig. 3). The scenario for first echo development in this case is a nonlinear feedback between ice nucleation/growth processes (with subsequent ice melting) and rain accretion of cloud occurring in the vicinity of the updraft-downdraft interface. The turbulent transport of hydrometeors across the interface zone enhances the recycling process. In the gamma warm cloud experiment 27-3, the first echo formed later due to autoconversion and in a different region of the cloud. That ice was excluded from that experiment provides strong evidence for the importance of ice processes in the early formation of precipitation in convective clouds. Dye et al. (1983) and Miller et al. (1983) argue for the importance of ice particle recycling and the need for persistence of kinematic features favorable to that process.

4.5 Hail growth on 28 May 1977

The hail production mechanisms in the Wynnewood storm are of particular interest because the storm produced abundant large hail. The retrieval technique is capable of assisting in the resolution of complex cloud microphysical problems such as hail formation and growth. Ziegler et al. (1983), hereafter referred to as paper Z, identify the large hail growth trajectories in the Wynnewoood storm using a Lagrangian model for individual hailstones and a quasi-adiabatic cloud model. Such a model has considerable power, although its deductive capabilities are probably significantly weakened because the cloud model used is not internally consistent. Lagrangian model results are strongly dependent on the embryo type and location specified in the initial condition, although nature produces a mixture of embryo properties that is generally

ill-defined in an **a priori** sense. Use of the kinematic microphysical modelling approach mitigates each of these defects. Cloud properties in Lagrangian models are derived with advection and accretion effects omitted, although this dissertation clearly demonstrates the predominance of these processes. The kinematic microphysical model includes these effects, and further describes the rain and ice processes leading to hail embryo formation.

The applicability of model output to a study of hail formation and growth is illustrated in Fig. 4.19 by selected horizontal cross-sections of model output at the 6.5 km level. Fig. 4.11 shows the wind field in this plane, while Fig. 4.17a shows the retrieved total reflectivity. Regions of updraft between 15 and 30 ms^{-1} are indicated by light stippling. Part (a) of Fig. 4.19 shows the temperature departure (C) from the environment, part (b) shows q_c (gg^{-1}), part (c) shows q_h (gg^{-1}), while parts (d) through (f) show the rain freezing rate ($gg^{-1}s^{-1}$), the ice-hail conversion rate, and the hail rate of cloud accretion (dry mode), respectively. The horizontal projection of the predominant hailstone trajectory A described in paper Z, is indicated by a heavy solid line in Fig. 4.19c. The arrowhead at the end of the trajectory indicates the direction of displacement of the hailstone.

Fig. 4.19a reveals that growing hail experiences large temperature differences while traversing the updraft. Downdrafts are warm and unsaturated at (3,10) and (9,11) due to adiabatic descent, contrary to the treatment in paper Z wherein downdrafts were necessarily assigned the properties of the far environment. As shown by Fig. 4.19b, cloud mixing ratios of up to 2 g kg^{-1} are present in the updraft cores. In

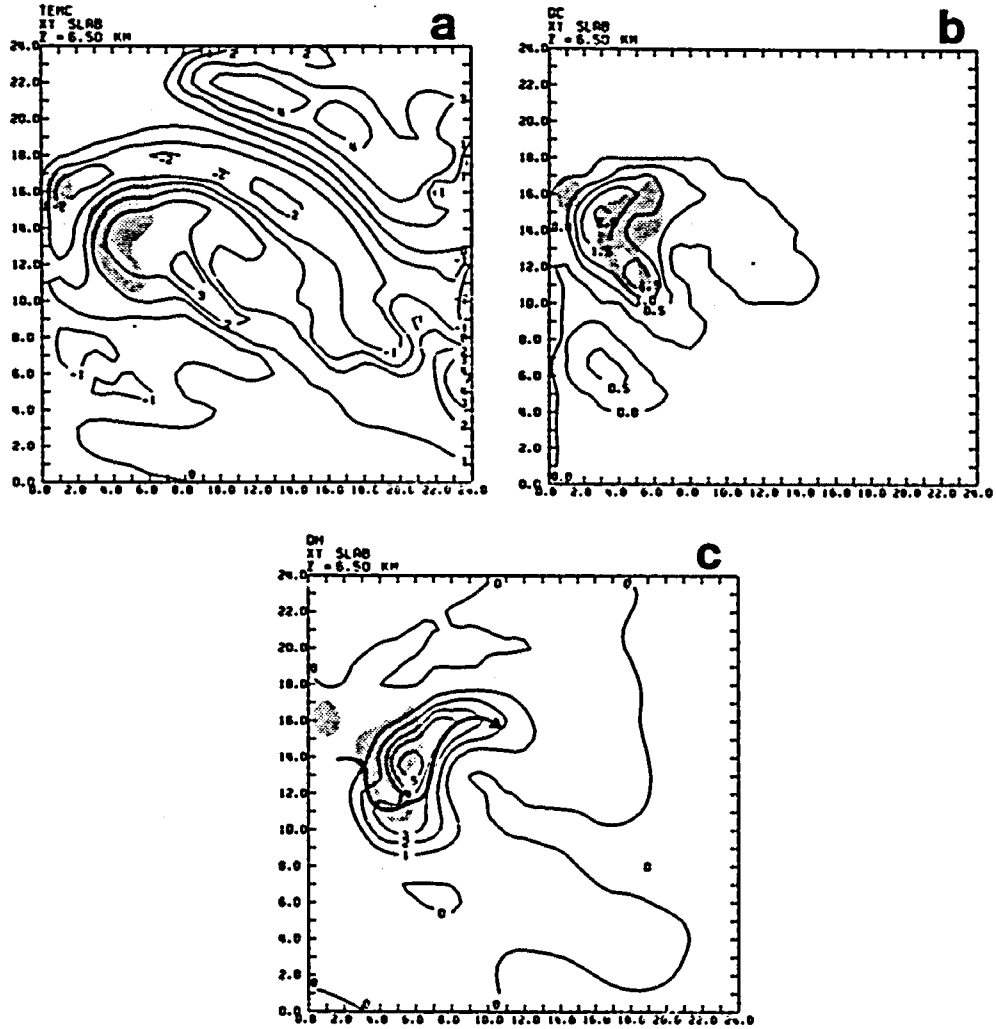

Fig. 4.19 Selected model output for experiment 28-2 in horizontal sections at 6.5 km. (a) temperature (°C) deviation from the environment, contour interval 1 C; (b) q_c (g kg^{-1}), contour interval 0.5 g kg^{-1}; (c) q_h(g kg^{-1}), contour interval 0.5 g kg^{-1}; (d) rain freezing rate R11 scaled by 10^6 (g $g^{-1}s^{-1}$), contour interval 10^{-6} g g^{-1} s^{-1}; (e) ice-hail conversion rate R29 scaled by 10^6 (g $g^{-1}s^{-1}$), contour interval 10^{-6} g g^{-1} s^{-1}; (f) hail dry mode accretion of cloud rate R15 scaled by 10^7 (g g^{-1} s^{-1}), contour interval 10^{-7} g g^{-1} s^{-1}. The predominant trajectory of hailstone A (from paper Z, see text) is indicated by the heavy solid curve in panel (c). Light stippling denotes updrafts between 15 and 30 ms^{-1}, and the enclosed unstippled region indicates updrafts exceeding 30 ms^{-1}.

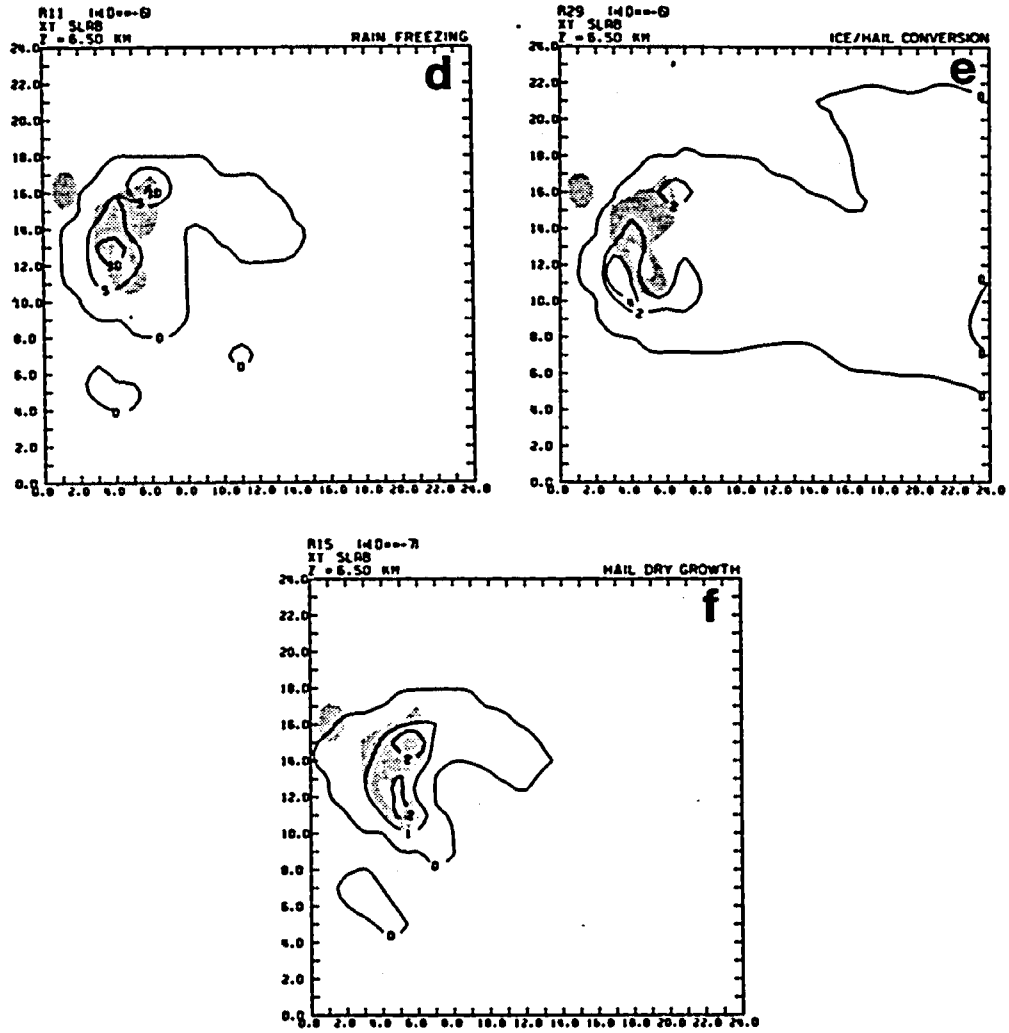

Fig. 4.19 (continued)

paper Z cloud was located in shallow middle level updrafts, whose bases were above the moist layer and should not contain significant condensate. Due to horizontal advection, the cloud describes the same comma-like shape as the echo. In Fig. 4.18c, the configuration of the core of maximum hail mixing ratio has the same S-shape as the predominant trajectory. This suggests a scenario wherein the 3-dimensional model is growing size-distributed hail along the predominant trajectory, producing the characteristic S-shaped mixing ratio and echo pattern. Fig. 4.19d indicates that considerable rain freezing is occurring within the updrafts, supplying a source of ice embryos for hail growth. Most of the sampled hail on 28 May has frozen drop embryos. The coincidence of spuriously high hail mixing ratios (coordinates (4.0, 11.0) in Fig. 4.19c) with peak ice-hail conversion in Fig. 4.19e, indicates that ice accumulation in this region is occurring too quickly. The model is possibly overemphasizing the recycling of rain from the low level precipitation core into the updraft core, in strong contrast to the observed reflectivity structure which features a weak echo region underlying the updraft maximum and associated bounded weak echo region. Wind analysis errors could cause the implied precipitation trajectory errors. The subsequent growth of hail by accretion (Fig. 4.19f) extends northward (downwind) from the eastern edge of the main updraft. The partial enclosure of the main updraft on its west and south flank by the U-shaped ice-hail conversion region as well as the configuration of the hail accretion zone, are features broadly consistent with the findings of Heymsfield and Musil (1982) regarding the particle growth processes in middle levels of a Colorado hailstorm.

A key difference between the 28 May case and Colorado hailstorms is that most of the Colorado hail embryos are graupels (Knight et al., 1974). The Oklahoma storm may possibly owe its relative propensity for frozen drop embryos to the existence of the rain maximum in middle levels of the main updraft. This rain maximum may be partially maintained by recycling, as previously discussed. Subsequent vertical advection, freezing (Fig. 4.19d), ice conversion to hail (Fig. 4.19e) and accretion of cloud (Fig. 4.19f) leads to the high hail mixing ratios (Fig. 4.19c). The Colorado storms frequently have very low reflectivities between cloud base and the freezing level, suggesting the presence of very low rain mixing ratios and negligable frozen drop embryo production. An important question for future research is whether the relative abundance of graupel and frozen drop embryos is modulated by the degree to which drops are recycled into the main updraft. The often cited difference in the height of cloud base in Colorado versus Oklahoma storms (Dye et al., 1974) may relate to the degree to which recycling drops evaporate in the unsaturated subcloud layer.

CHAPTER V

SUMMARY

The goal of this research is the development and utilization of a technique to analyze hydrometeor distributions and thermal fields within observed mature convective storms. The major working hypothesis is that the wind field exerts a strong influence on hydrometeor fields. The relative importance of the various thermodynamic, microphysical and transportative forcing mechanisms have been assessed on the basis of the output of a three-dimensional kinematic cloud model that employs Doppler wind fields. This retrieval method is a logical extension of the tradition of kinematic cloud physics models. A new warm cloud parameterization based on a gamma function representation of cloud and rain distributions, has been developed to improve the model microphysics. The distinct shortage of verification and calibration of existing microphysical models is mitigated by adopting a model sensitivity test approach, using observed reflectivities to verify the model diagnosis. The quasi-steadiness assumption and various numerical aspects of the kinematic model have been tested using input from a dynamically simulated cloud for verification. Real data tests have been performed on intense and weak convection in order to test the model response to observed winds, determine model parameter sensitivites, and deduce the detailed thermal and microphysical structure.

5.1 Results

The verification of a new warm cloud coalescence parameterization reported in Chapter II, reveals good agreement with a highly resolved

finite difference coalescence model over a range of cloud distribution parameters. Two key physical attributes of this model are that the cloud autoconversion rate is proportional to the sixth power of mean droplet diameter as well as cloud mixing ratio, and that the mean drop diameter may increase despite a constant rain mixing ratio. A new parameterization for hail accretion of cloud has also been described in Chapter II. This parameterization features the simultaneous representation of dry and wet modes in adjoining size intervals spanning the entire size range. Low density riming effects are partially included.

The tests of the warm cloud kinematic model utilizing proxy data in Chapter III, generally reveal that the model has considerable diagnostic skill despite the steadiness assumption. Relative errors of all model variables are small in the cloud core, increasing outside the core and in the anvil region. The absolute errors are everywhere rather small. The errors in the thermal variables are generally smallest, since these are tracer quantities whose variation is fundamentally constrained by the characteristic solution of the advection equation and the boundary values of the problem. Rain mixing ratio errors are larger due to the nonlinear effects of sedimentation and cloud accretion, and are believed to arise from the steadiness assumption. Based upon the results of sensitivity tests, the following observations and recommendations are submitted;

1) The kinematic model steady state solution provides a valid approximation of thermal and microphysical variables simulated in a three-dimensional time dependent dynamic model. Substitution of observed winds for simulated winds should not in theory affect this conclusion.

2) The addition of white noise to the wind field in a simulation of Doppler observation errors, does not produce a significant degradation of retrieved fields. Random errors in observed wind fields will also not generate significant retrieval errors. This conclusion is not necessarily warranted in the event that random errors greatly exceed those used in the simulation. Systematic errors, which could result in large errors due to a net displacement of parcel trajectories, are not included in these tests.

3) Neglecting turbulent dissipation results in noise generation during the model integration.

4) The steady solution is independent of the initial condition (of course, the time-dependent solution is a function of the initial conditions).

5) Despite storm non-steadiness, a term-by-term evaluation of model equations reveals that the local derivative is negligable compared with at least two other terms within the storm core. This fact permits approximate retrieval with the steady solution, and renders feasible the extension of the retrieval method to observed storms which are probably at best only quasi-steady.

6) The advection terms are among the largest terms in the model equations, demonstrating the overwhelming influence of the wind field on configuration of thermal and microphysical variables in convective storms.

It is proposed that all important conclusions drawn from the proxy test results are also applicable to the full warm/cold cloud model as applied to real data. Observations provided by aircraft penetrations could be used to test the validity of this assumption.

The real data model tests described in Chapter IV, show good agreement between observed and modelled radar reflectivities and also illustrate the abundance of relevant data generated by the model. The real data tests utilize data from two separate cases of deep convection in Oklahoma, the first on 27 May 1979 and the second on 28 May 1977. Nine tests incorporating different combinations of microphysical parameters with a constant wind field are performed for the 27 May case. Two tests are performed on the 28 May data with fixed microphysical parameters, the first using the observed wind field and the second using a subjectively modified wind field.

The main results of the 27 May tests as reported in Chapter IV are summarized as follows;

1) Good agreement is observed between retrieved and observed radar reflectivities, despite noticeable discrepancies in reflectivity measured by each radar and uncertainty regarding the optimum method for computing radar reflectivity from model output.

2) The contribution to total reflectivity is dominated by rain processes below the freezing level and ice processes above the freezing level. Melting of ice precipitation debris is an important modifier of overall low level reflectivity, and the resulting rain reflectivity is sensitive to the particular

hybridization scheme used between the one-parameter ice distributions and the two-parameter rain distribution. Recycling may provide an important stimulus for precipitation development in updrafts.

3) The bulk warm cloud model produces retrieved reflectivities in very good agreement with observations, despite simplified parameterized microphysics and exclusion of ice microphysics. Core reflectivities are rather large, probably due to an excessive precipitation efficiency in this type of model.

4) The gamma warm cloud parameterization produces reduced overall core reflectivities, and a distinct low level maximum in excellent agreement with observations. This feature is due to the large hydrometeor self-collection process.

5) The peak hail mixing ratio and reflectivity are dependent on the value of the ice-hail conversion parameter D_g, since this parameter controls the rate at which ice mass is shifted to the hail distribution. Retrieved reflectivities are too high if D_g is decreased significantly below 3 mm, and show good agreement with observations if D_g is increased to 5 mm. The optimum value of D_g appears to lie in the range 3-5 mm, although varying other model parameters independently of hail mixing ratio (e.g. hail concentration) could conceivably extend these limits.

6) The partial inclusion of variable rime density in the hail dry growth parameterization results in retrieved reflectivities much closer to observations, than is obtained with a fixed

density of 0.9 g cm^{-3}. The high density assumption leads to an overestimated riming rate.

7) The assumed width of the cloud droplet distribution does not have an important effect on retrieved reflectivities or cloud properties in general.

8) The restriction of the model domain to two space dimensions results in the production of serious artifacts in the retrieved precipitation fields, most noticeably downwind from the updraft core at low levels.

The same microphysical sensitivities may apply to other storm cases, although future case studies would help to answer this question.

The main results of the 28 May tests as reported in Chapter IV are listed as follows;

1) Systematic wind field errors may be roughly approximated by using the kinematic model to find major discrepancies between observed and retrieved reflectivities. The spurious precipitation features must be unambiguously related to specific wind field features to deduce the appropriate wind field adjustment.

2) Evidence of systematic vertical velocity errors in the 28 May wind analysis is noted in two areas. Updrafts greater than the order of typical hydrometeor fallspeed are analyzed well downstream from the storm core, while updrafts are also analyzed within low levels of the intense precipitation core. Both features are at variance with conceptual and dynamic simulation storm models, and produce severe artifacts in retrieved reflectivities.

3) Incorporation of simple subjective wind field modifications into the 28 May wind analysis which are motivated by items 1) and 2) above, result in better overall agreement between observed and retrieved reflectivities[1].

Diagnosis of precipitation growth rates for the 27 May and 28 May cases as well as advection, diffusion and sedimentation rates, permits a ranking of the various processes. The prominence of the condensation and accretion processes is noted, as well as the overwhelming importance of advection and sedimentation in redistributing existing precipitation. Primary ice nucleation and cloud autoconversion are evidently not very important mechanisms for generating hydrometeor mass during the mature storm phase. These processes are vital to the initiation of precipitation late in the cumulus phase, with mass transfer subsequently dominated by accretion and freezing/melting as the storm approaches maturity. The recycling of millimetric-sized hydrometeors into the main updraft is evidently important in maintaining the overall echo core structure in the mature storm phase.

The versatility of kinematic model output is illustrated by a discussion of hail formation and growth on 28 May. The model implicitly generates graupel and frozen drop embryos, which subsequently accumulate considerable mass as they are advected through the cloud along the predominant trajectory. The model provides internally consistent

---

[1]While verification of retrieved reflectivities is encouraging, this does not constitute a necessary and sufficient condition for correct diagnosis of *in situ* microphysical characteristics. An additional condition providing sufficiency would be a correctly modelled distribution shape, if reflectivity varies only with hydrometeor size and concentration.

thermal and microphysical quantities which are vital to such studies. Model output suggests that a high proportion of frozen drop embryos relates to the survival of recycling drops.

5.2 Philosophical questions and model limitations

The observed wind fields in convective storms are clearly related to coincident thermal and microphysical fields by an appropriate set of continuity equations. The microphysical processes, which play an important role in the continuity of heat and water substance, have been parameterized to the extent where significant retrieval errors could result. A verification dilemma is encountered wherein the residual discrepancies between retrieved and observed reflectivities may plausibly originate in wind field errors, in the use of approximate Z-q relationships, in parameterization errors, or a combination of these three factors.

There are several important model limitations. An initial condition must be specified in order to study the time-dependent solution, which requires either very comprehensive observations (not available) or use of the steady approximation at the initial time. The model does not accurately retrieve thermal variables in the clear environment, which is not in steady state and for which Doppler observations are not available. Higher model spatial resolution is required to reproduce narrow features such as the BWER on 28 May or shallow features such as the gust front. The environmental wind fields and the lateral boundary conditions on environmental temperature and moisture may be rather poorly defined, and variations of these parameters can have a great impact on precipitation production in the convective cell. Non-random wind field

errors and a parameterized microphysical representation may introduce additional retrieval errors.

5.3 Recommendations for future research

This investigation suggests several areas of possible future research. Time-spaced wind analyses should be inserted into the model to study the full time-dependent solution. Use of the model to assist in dynamic and hail growth studies is another area of great potential. The kinematic and dynamic retrieval schemes could be merged using variational methods (Sasaki, 1958), to provide retrieved temperature and pressure fields posessing internal consistency with the complete set of governing equations. The thunderstorm electrification problem could be addressed using knowledge of the coexisting air currents and hydrometeor distributions.

Microphysical studies of individual hydrometeor growth will profit from an improved model of the spatial distributions of temperature and cloud water content. The conventional assumption of quasi-adiabatic cloud temperature and water profiles in hail growth studies applied to real clouds may be substantially in error. This is due to the fact that critical effects such as advection, diffusion, and hydrometeor accretion of cloud (implied by high radar reflectivities) are not accounted for in those studies.

Techniques have recently been developed for the retrieval of perturbation pressure and temperature fields in convective storms, given detailed knowledge of the momentum fields (Hane and Scott, 1978; Hane et al., 1981, Brandes, 1983). These methods are based on inversion of the momentum equations appropriate for deep moist convection. They are

theoretically capable of yielding the true thermodynamic fields, given accurate observed winds. The current lack of knowledge concerning the water vapor and hydrometeor buoyancy fields may limit the retrieval ability of these schemes, considering for example the compensation of a three degree potential temperature excess by a 10 g kg^{-1} water load in the vertical momentum equation. In many of the dynamic retrieval method tests, the water substance buoyancy was either left out of the procedure altogether or included as specified from the input cloud model data. A numerical modelling approach is proposed to supplement hydrometeor data, which is not sampled on scales approaching the Doppler wind information.

Fundamental to all of these proposed studies is the need for verified model realism, hence a concurrent and methodical aircraft sampling program should be undertaken to augment Doppler and surface network data. Particularly interesting meteorological features which could be studied in the near future are time-evolving tornadic storm hook echos, bounded weak echo regions, and important cloud features such as the wall cloud and the V-shaped (satellite-observed) cloud top temperature pattern. The cloud model microphysical parameterization should be expanded to obtain more detailed and accurate knowledge of the thermal and microphysical structure of observed convective storms.

BIBLIOGRAPHY

Abramowitz, M. and Irene Stegun, 1964: **Handbook of Mathematical Functions**, Natl. Bur. Stds. Appl. Math. Ser., 55, 1046 pp.

Alofs, Darryl J. and Tung-Hsi Liu, 1981: Atmospheric measurements of CCN in the supersaturation range 0.013 - 0.681%, J. Atmos. Sci., 38, 2772-2778.

Barnes, Stanley L., 1970: Some aspects of a severe, right-moving thunderstorm deduced from mesonetwork rawinsonde observations, J. Atmos. Sci., 27, 634-648.

Battan, Louis J., 1973: **Radar observation of the atmosphere**, Univ. of Chicago Press, 324 pp.

Beard, K.V. and H.R. Pruppacher, 1969: A determination of the terminal velocity and drag of small water drops by means of a wind tunnel, J. Atmos. Sci., 26, 1016-1022.

Beard, K.V., 1976: Terminal velocity and shape of cloud and precipitation drops aloft, J. Atmos. Sci., 33, 851-864.

Berry, Edwin X., and Richard L. Reinhardt, 1974a: An analysis of cloud drop growth by collection: Part I. Double distributions, J. Atmos. Sci., 31, 1814-1824.

_____, 1974b: An analysis of cloud drop growth by collection: Part II. Single initial distributions, J. Atmos. Sci., 31, 1825-1831.

_____, 1974c: An analysis of cloud drop growth by collection: Part III. Accretion and self-collection, J. Atmos. Sci., 31, 2118-2126.

_____, 1974d: An analysis of cloud drop growth by collection: Part IV. A new parameterization, J. Atmos. Sci., 31, 2127-2135.

Bigg, E.K., 1953: The supercooling of water, Proc. Phys. Soc. London, B66, 668-694.

Blottner, F.G., 1970: Finite difference methods of solution of the boundary layer equations, AIAA Journal, 8, 193-205.

Brazier-Smith, P.R., S.G. Jennings and J. Latham, 1972: The interactions of falling water drops: Coalescence, Proc. R. Soc., A326, pp.393-408.

_____, 1973: Raindrop interactions and rainfall rates within clouds, Quart. J. Roy. Meteor. Soc., 99, 260-272.

Browning, Keith A., 1964: Airflow and precipitation trajectories within severe local storms which travel to the right of the winds, J. Atmos. Sci., 21, 634-639.

_____, 1965: Some inferences about the updraft in a severe local, storm, J. Atmos. Sci., 22, 669-677.

_____ and David Atlas, 1965: Initiation of precipitation in vigorous convective clouds, J. Atmos. Sci., 22, 678-683.

_____ and G.B. Foote, 1976: Airflow and hail growth in supercell storms and some implications for hail suppression, J. Roy. Met. Soc., 102, 499-533.

_____, 1977: The structure and mechanisms of hailstorms, Meteor. Monog., 16, 38, 1-43.

Byers, Horace R. and Roscoe R. Braham, Jr., 1948: Thunderstorm structure and circulation, J. Met., 5, 71-86.

Chalon, J.-P., J.C. Fankhauser and P.J. Eccles, 1976: Structure of an evolving hailstorm, Part I: General characteristics and cellular structure, J. Atmos. Sci., 104, 564-575.

Chisholm, A.J. and Marianne English, 1973: Alberta hailstorms, Meteor. Monog., 14, 36, 98 pp.

Clark, Terry L., 1974: A study in cloud phase parameterization using the gamma distribution, J. Atmos. Sci., 31, 142-155.

_____, 1976: Use of log-normal distributions for numerical calculations of condensation and collection, J. Atmos. Sci., 33, 810-821.

_____, 1979: Numerical simulations with a three-dimensional cloud model: Lateral boundary condition experiments and multicellular severe storm simulations, J. Atmos. Sci., 36, 2191-2215.

_____ and W.D. Hall, 1983: A cloud physical parameterization method using movable basis functions: Stochastic coalescence parcel calculations, J. Atmos. Sci., 40 1709-1728.

Cotton, William R., 1972: Numerical simulation of precipitation development in supercooled cumuli-Part I., Mon. Wea. Rev., 100, 757-763.

Davies-Jones, Robert P., 1974: Discussion of measurements inside high-speed thunderstorm updrafts, J. Appl. Meteor., 13, 710-717.

Dye, James E., Charles A. Knight, Vim Toutenhoofd, and Theodore W. Cannon, 1974: The mechanism of precipitation formation in northeastern Colorado cumulus III. Coordinated microphysical and radar observations and summary, J. Atmos. Sci., 31, 2152-2159.

Fankhauser, J.C., 1976: Structure of an evolving hailstorm. Part II: Thermodynamic structure and airflow in the near environment, Mon. Wea. Rev., 104, 576-587.

Federer, B. and A. Waldvogel, 1975: Hail and raindrop distributions from a Swiss multicell storm, J. Appl. Met., 14, 91-97.

Fletcher, N.H., 1962: **The Physics of Rain Clouds**, Cambridge Univ. Press, 390 pp.

Foote, G.B. and P.S. du Toit, 1969: Terminal velocity of raindrops aloft, J. Appl. Met., 8, 249-253.

_____ and Harold W. Frank, 1983: Case study of a hailstorm in Colorado. Part III: Airflow from triple Doppler measurements, J. Atmos. Sci., 40, 686-707.

Garrett, R.A. and Vaughn D. Rockney, 1962: Tornadoes in northeastern Kansas, May 19, 1960, Mon. Wea. Rev., 90, 231-240.

Goff, R. Craig, 1975: Thunderstorm-outflow kinematics and dynamics, NOAA Tech. Memo. ERL NSSL-75, Norman, 63 pp., [NTIS #PB-250808/AS].

Gunn, K.L.S. and Marshall, J.S., 1958: The distribution with size of aggregate snowflakes, J. Met., 15, 452-461.

Gunn, R. and G.D. Kinzer, 1949: The terminal velocity of fall for water drops in stagnant air, J. Met., 6, 243-248.

Hane, Carl E., 1973: The squall line thunderstorm: Numerical experimentation. J. Atmos. Sci., 30. 1672-1690.

_____, and Bryan C. Scott, 1978: Temperature and presure perturbations within convective clouds derived from detailed air motion information: Preliminary testing, Mon. Wea. Rev., 106, 654-661.

_____, R.B. Wilhelmson and Tzvi Gal-Chen, 1981: Retrieval of thermodynamic variables within deep convective clouds: Experiments in three dimensions, Mon. Wea. Rev., 109, 564-576.

Heymsfield, Andrew J., 1978: The characteristics of graupel particles in northeastern Colorado cumulus congestus clouds, J. Atmos. Sci., 35, 284-295.

_____, Peter N. Johnson and James E. Dye, 1978: Observations of moist adiabatic ascent in northeast Colorado cumulus congestus clouds, J. Atmos. Sci., 35, 1689-1703.

_____, Charles A. Knight and James E. Dye, 1979: Ice initiation in unmixed updraft cores in northeast Colorado cumulus congestus clouds, J. Atmos. Sci., 36, 2216-2229.

_____, Arthur R. Jameson and Harold W. Frank, 1980: Hail growth mechanics in a Colorado storm: Part II: Hail formation processes, J. Atmos. Sci., 37, 1779-1807.

_____, and Dennis J. Musil, 1982: Case study of a hailstorm in Colorado. Part II: Particle growth processes at mid-levels deduced from in-situ measurements, J. Atmos. Sci., 39, 2847-2866.

Hobbs, P.V., Shirley Chang and John D. Locatelli, 1974: The dimensions and aggregation of ice crystals in natural clouds, J. Geo. Res., 19, 2199-2206.

Houze, Robert A., Jr., Peter V. Hobbs, Paul H. Herzegh, and David B. Parsons, 1979: Size distributions of precipitation particles in frontal clouds, J. Atmos. Sci., 36, 156-162.

Joe, P.I., Roland List, and G.B. Lesins, 1980: Ice accretions part II: Rain production by cloud water conversion, J. Rech. Atmos., 14, 357-364.

Kessler, Edwin, 1969: On the distribution and continuity of water substance in atmospheric circulations, Meteor. Monog., 10, 32, 84 pp.

_____, Ed., 1983: Thunderstorms: A social, scientific and technological documentary Vol.I: The thunderstorm in human affairs, Univ. of Oklahoma Press, 186 pp.

Klemp, Joseph B. and Robert B. Wilhelmson, 1978: The simulation of three-dimensional convective storm dynamics, J. Atmos. Sci., 35, 1070-1096.

_____, R.B. Wilhelmson and P.S. Ray, 1981: Observed and numerically simulated structure of a mature supercell thunderstorm, J. Atmos. Sci., 38, 1558-1580.

_____ and Richard Rotunno, 1983: A study of the tornadic region within a supercell thunderstorm, J. Atmos. Sci., 40, 359-377.

Knight, Charles A., Nancy C. Knight, James E. Dye and Vim Toutenhoofd, 1974: The mechanism of precipitation formation in northeastern Colorado cumulus I. Observations of the precipitation itself, J. Atmos. Sci., 31, 2142-2147.

Koenig, L.R., 1971: Numerical modeling of ice deposition, J. Atmos. Sci., 28, 226-237.

Leighton, H.G. and R.R. Rogers, 1974: Droplet growth by condensation and coalescence in a strong updraft, J. Atmos. Sci., 31, 271-279.

Lilly, D.K., 1965: On the computational stability of numerical solutions of time-dependent non-linear geophysical fluid dynamics problems, Mon. Wea. Rev., 93, 11-26.

Long, Alexis B., 1974: Solutions to the droplet collection equation for polynomial kernels, J. Atmos. Sci., 31, 1040-1052.

Low, T.B. and Roland List, 1982: Collision, coalescence and breakup of raindrops. Part I: Experimentally established coalescence efficiencies and fragment size distributions in breakup, J. Atmos. Sci., 39, 1591-1606.

Macklin, W.C. and I.H. Bailey, 1966: On the critical liquid water concentrations of large hailstones., Quart. J. Roy. Meteor. Soc., 92, 297-300.

Marshall, J.S. and W. McK. Palmer, 1948: The distribution of raindrops with size, J. Met., 5, 165-166.

Marwitz, J.D., 1972: The structure and motion of severe hailstorms. Part I: Supercell storms, J. Appl. Meteor., 11, 166-179.

Miller, L.J. and J.C. Fankhauser, 1983: Radar echo structure, air motion and hail formation in a large stationary multicellular thunderstorm, J. Atmos. Sci., 40, 2399-2418.

Musil, Dennis J., 1970: Computer modeling of hailstone growth in feeder clouds, J. Atmos. Sci., 27, 474-482.

Nelson, Stephan P., 1983: The influence of storm flow structure on hail growth, J. Atmos. Sci., 40, 1965-1983.

Newton, Chester W., 1966: Circulations in large sheared cumulonimbus, Tellus, 18, 699-713.

Ogura, Yoshimitzu and Tsutomu Takahashi, 1971: Numerical simulation of the life cycle of a thunderstorm cell, Mon. Wea. Rev., 99, 895-911.

Orville, Harold D. and Fred J. Kopp, 1977: Numerical simulation of the life history of a hailstorm, J. Atmos. Sci., 34, 1596-1618.

Passarelli, Richard E., Jr., 1978: An approximate analytic model of the vapor deposition and aggregation growth of snowflakes, J. Atmos Sci., 35, 118-124.

Pflaum, J.C. and H.R. Pruppacher, 1979: A wind tunnel investigation of the growth of graupel initiated from frozen drops, J. Atmos. Sci., 36, 680-689.

_____, 1980: Hail formation via microphysical recycling, J. Atmos. Sci., 37, 160-173.

Planck, V.G., R.O. Berthel and L.V. Delgado, 1980: The shape of raindrop spectra for different situations and averaging periods, J. Rech. Atmos. 14, 301-309.

Pruppacher, Hans R. and James D. Klett, 1978: **Microphysics of clouds and precipitation**, D. Reidel, 714 pp.

Ray, Peter S., Conrad L. Ziegler, William Bumgarner, and Robert J. Serafin, 1980: Single- and multiple-Doppler radar observations of tornadic storms, Mon. Wea. Rev., 108, 1607-1625.

_____ and Karen L. Sangren, 1983: Multiple-Doppler radar network design, J. Clim. Appl. Met., 32, 1444-1454.

Roache, Patrick, 1972: **Computational Fluid Dynamics**, Hermosa Publishers, Albuquerque, N.M., 446 pp.

Robert, A.J., 1966: The integration of a low order spectral form of the primitive meteorological equations, J. Met. Soc. Japan, 44, 237-245.

Rogers, R.R., 1976: **A short course in cloud physics**, Pergamon Press, 227 pp.

Rutledge, Steven Allan, 1983: A numerical study of cloud and precipitation processes in mesoscale rainbands, Ph.D. dissertation, University of Washington, Seattle, 220 pp.

Ryan, R.T., H.H. Blau, Jr., P.C. von Thüna , and M.L. Cohen, 1972: Cloud microstructure as determined by an optical cloud particle spectrometer, J. Appl. Met., 11, 149-156.

Sasaki, Y., 1958: Objective analysis based on the variational method. J. Meteor. Soc. Japan, 36, 77-88.

Schlesinger, Robert E., 1978: A three-dimensional model of an isolated thunderstorm: Part I. Comparative experiments for variable ambient wind shear, J. Atmos. Sci., 35, 690-713.

Silverman, Bernard A. and Morton Glass, 1973: A numerical simulation of warm cumulus clouds: Part I. Parameterized vs. non-parameterized microphysics, J. Atmos. Sci., 30, 1620-1637.

Smagorinsky, J., 1963: General circulation experiments with the primitive equations: 1. The basic experiment, Mon. Wea. Rev., 91. 99-164.

Smith, P.L., Jr., C.G. Myers and H.D. Orville, 1975: Radar reflectivity factor calculations in numerical cloud models using bulk parameterization of precipitation, J. Appl. Met., 14, 1156-1165.

Soong, Su-Tzai and Yoshimitzu Ogura, 1973: A comparison between axisymmetric and slab-symmetric cumulus cloud models, J. Atmos. Sci., 30, 879-893.

Squires, P., 1958: The microstructure and colloidal stability of warm clouds. Part I - The relation between structure and stability, Tellus, 10, 256-261.

Srivastava, R.C., 1971: Size distribution of raindrops generated by their breakup and coalesence, J. Atmos. Sci., 28, 410-415.

_____, 1978: Parameterization of raindrop size distributions, J. Atmos. Sci., 35, 108-117.

Takahashi, Tsutomu, 1981: Warm rain development in a three-dimensional cloud model, J. Atmos. Sci., 38, 1991-2013.

Toutenhoofd, Vim and Joseph B. Klemp, 1983: An isolated cumulonimbus observed in northeastern Colorado: Comparison of field observations with results of a three-dimensional simulation, Mon. Wea. Rev., 111, 468-478.

Twomey, S., 1959: The nuclei of natural cloud formation, Part II: the supersaturation in natural clouds and the variation of cloud droplet concentration, Geofys. Pura E Appl., 43, 243-249.

Wilhelmson, Robert B. and Joseph B. Klemp, 1978: Simulations of right- and left-moving storms produced through storm splitting, J. Atmos. Sci., 35, 1097-1110.

Williams, Richard and Peter J. Wojtowicz, 1982: A simple model for droplet size distribution in atmospheric clouds, J. Appl. Met., 21, 1042-1044.

Wisner, Chester, H.D. Orville, and Carol Myers, 1972: A numerical model of a hail-bearing cloud, J. Atmos. Sci., 29, 1160-1181.

Ziegler, Conrad L., Peter S. Ray and Nancy C. Knight, 1983: Hail growth in an Oklahoma multicell storm, J. Atmos. Sci., 40, 1768-1791.

APPENDIX A

ANALYTIC INTEGRATION METHODS

Several analytic methods are used when evaluating various integrals in the parameterizations. The convolution integral and the integral of a product of power and exponential functions, are frequently encountered.

The convolution integral appears in the form

$$g(x) = \int_0^x (x-y)^a y^b dy,$$

where a and b are real numbers. This integral may be expressed in the form

$$F_1 * F_2 = \int_0^x F_1(x-y)\, F_2(y)\, dy,$$

where $F_1 * F_2$ is the convolution of F_1 and F_2. The convolution theorem states that

$$\mathbf{L}(F_1 * F_2) = f_1(s)\, f_2(s),$$

where a boldface L denotes the Laplace transform and $f(s) = \int_0^\infty e^{-st} F(t) dt$. Here $F_1(x) = x^a$ and $F_2(x) = x^b$. The Laplace transforms are $f_1(s) = \Gamma(a+1)/s^{a+1}$ $(a+1 > 0)$ and $f_2(s) = \Gamma(b+1)/s^{b+1}$ $(b+1 > 0)$, where

Γ is the complete gamma function. Then the product of the transforms is $f_1(s)\ f_2(s) = \Gamma(a+1)\Gamma(b+1)/s^{a+b+2}$. Taking the inverse transform yields

$$L^{-1}(f_1(s)f_2(s)) = g(x) = \Gamma(a+1)\ \Gamma(b+1)\ x^{a+b+1}/\Gamma(a+b+2), \qquad (A.1)$$

which is the desired integral.

The general form of the integral involving a product of power and exponential functions is $\int_0^c x^a e^{-bx} dx$, where a,b and c are positive real numbers. Two cases involving a finite or infinite upper integration limit c are encountered. For the case of c finite, there follows

$$\int_0^c x^a\ e^{-bx} dx = \gamma(a+1,bc)/b^{a+1}, \qquad (A.2)$$

where γ is the incomplete gamma function. For the case of c infinite,

$$\int_0^\infty x^a e^{-bx} dx = \Gamma(a+1)/b^{a+1}, \qquad (A.3)$$

where Γ is the complete gamma function. Definitions of and useful identities involving γ and Γ may be found in Abramowitz and Stegun (1964).

APPENDIX B

PROPERTIES OF THE GAMMA DISTRIBUTION MODEL

The distribution of cloud and rain are represented by the Gamma function of the general form

$$n(v) = \left[N(\nu+1)^{\nu+1}(v/v_o)^{\nu}\ e^{-(\nu+1)v/v_o}\right]/\Gamma(\nu+1)v_o\ , \qquad (B.1)$$

where N is the total concentration (cm^{-3}), v_o is the mean volume (cm^3), ν is the shape parameter, v is volume, Γ is the complete gamma function, and n is the concentration per unit volume interval. The change of variable $x = v/v_o$ is frequently used in the various derivations employing this distribution function.

The n-th moment of the Gamma distribution is obtained by multiplying eq. (B.1) by v^n and integrating over all volume following the formula (A.2). If the n-th moment is denoted M_n, then there follows

$$M_n = (N(\nu+1/v_o)^{\nu+1}/\Gamma(\nu+1)) \int_o^{\infty} v^{\nu+n} e^{-(\nu+1)v/v_o}\, dv$$

$$= \Gamma(\nu+n+1)\ N\ v_o^n/\Gamma(\nu+1)(\nu+1)^n. \qquad (B.2)$$

From eq. (B.2), the zeroth and first moments are respectively N and Nv_o. The mass-weighted mean volume is $M_2/M_1 = (1+1/(\nu+1))\ v_o$.

The radar reflectivity of the rain distribution will be used to verify the numerical model output against observed reflectivities.

Radar reflectivity Z is defined by $Z \equiv \int_0^\infty n(D)\, D^6 dD$, where D is drop diameter and n is number concentration density. Using the relation $n(D)\, dD = n(v)dv$, mapping D onto v, and expressing n(v) according to eq. (B.1), the reflectivity is expressed as

$$Z = 3.6 \times 10^{13}(\nu+2)\, N\, v_o^2/(\nu+1)\pi^2 \quad [mm^6 m^{-3}]. \tag{B.3}$$

The volume variance of the gamma distribution is related to v_o and ν in a straightforward manner. The variance is written as

$$\sigma^2[v] = E[v^2] - (E[v])^2,$$

where an E denotes statistical expectation. Now using the first three power moments N, Nv_o, and $(1+1/(1+\nu))Nv_o^2$, it follows that $E[v] = M_1/M_o = v_o$ and furthermore that $E[v^2] = M_2/M_o = (1+1/(1+\nu))v_o^2$. The resulting expression of relative volume variance is (Berry and Reinhardt, 1974a)

$$\text{Var } v \equiv \sigma^2[v]/v_o^2 = (1+\nu)^{-1} . \tag{B.4}$$

The approximate relation Var r = 0.14 Var v associates the relative variances of radius and volume.

Rain concentration fallspeed is computed for the mean volume drop, with mixing ratio fallspeed for the mass weighted mean volume drop (Srivastava, 1978). For mean drop radius $r_o > 0.06$ cm fallspeed is expressed by (Rogers, 1976)

$$V_r = 20.1\, r_o^{1/2}\, (\rho_o/\rho)^{1/2} , \tag{B.5}$$

while for $r_o < 0.06$ cm the appropriate relation is

$$V_r = 80.0\ r_o\ (\rho_o/\rho)^{1/2} \ . \qquad \text{(B.6)}$$

These expressions are based on the Gunn and Kinzer (1949) fallspeed data with an empirical correction for height due to Foote and du Toit (1969). Terminal fallspeeds predicted using eq. B.6 are within 3% of the Gunn and Kinzer data or the Beard and Pruppacher (1969) values. Fallspeeds determined from eq. B.5 are within 10% of the Gunn and Kinzer data or the Beard (1976) values. A mass-weighted mean fallspeed appropriate for an equivalent inverse-exponential size distribution with equal water content to the gamma rain distribution, is (Klemp and Wilhelmson, 1978a)

$$V_r = 36.34\ (\rho q_r)^{0.1346}\ (\rho_o/\rho)^{1/2} \ . \qquad \text{(B.7)}$$

All fallspeeds are in units of ms^{-1}.

The drop distribution is frequently plotted in units of liquid water content per unit log radius. The peak liquid water content location at volume v is expressed by $v = (\nu+2)\ v_o/(\nu+1)$.

APPENDIX C

WARM CLOUD PARAMETERIZATION

Section C.1 Cloud autoconversion parameterization

This section treats the parameterization of coalescence of cloud droplets to initiate rain formation. The coalescence process produces larger droplets, and small drops possessing fallspeeds of order 10 cm s^{-1} are ultimately formed. The term "autoconversion" refers to a particular discretization of this transition, wherein the droplet distribution is subdivided into non-precipitating and precipitating size categories. As droplets coalesce, a small fraction of the associated mass is transferred to the precipitating size category. The non-precipitating category is called "cloud" and the precipitating category is called "rain". The governing kinetic equation for the evolution of the droplet distribution is the stochastic coalescence equation (SCE) which may be written in the form (Pruppacher and Klett, 1978)

$$\frac{dn(v,t)}{dt} = \tfrac{1}{2}\int_0^v K(u,v-u)n(u,t)n(v-u,t)\,du$$

$$-n(v,t)\int_0^\infty K(v,u)n(u,t)du. \qquad (C.1.1)$$

This equation describes the change of number density of droplets of volume v through binary collision and coalescence of droplets whose volumes v-u and u add to the volume v. The collection kernel K(u,v)

($cm^{-3}s^{-1}$) is proportional to the coalescence rate of drops of volumes u and v in an expected sense. This parameterization uses a test function approach to evaluate eq. (C.1.1) analytically, and the resulting expressions are integrated to obtain moment tendency equations.

The integrands in eq. (C.1.1) are rendered analytic by substituting the gamma distribution for n(v) along with accurate polynomial approximations P(u,v) of K(u,v) due to Long (1974). These take the form

$$P(v,u) = \begin{cases} a_1(v^2+u^2) \ , & R < 50\ \mu m \quad \text{(C.1.2a)} \\ a_2(v+u) \ , & R > 50\ \mu m \quad \text{(C.1.2b)} \end{cases}$$

or alternatively

$$P(v) = \begin{cases} a_3\, v^2 \ , & R < 50\ \mu m \quad \text{(C.1.3a)} \\ a_4\, v \ , & R > 50\ \mu m \ . \quad \text{(C.1.3b)} \end{cases}$$

These approximations are applicable over specified ranges of collection drop radius R. In eqs. (C.1.2), $a_1 = 9.44 \times 10^9$ and $a_2 = 5.78 \times 10^3$ while in eqs. (C.1.3), $a_3 = 1.1 \times 10^{10}$ and $a_4 = 6.33 \times 10^3$. For sake of generality, eqs. (C.1.2) are used to evaluate the autoconversion integral although the treatment is nearly identical using eqs. (C.1.3). Furthermore, the total drop distribution is separated into two portions, with cloud droplets having radii less than 41 μm and rain drops

exceeding that radius (Berry and Reinhardt, 1974b). Hence, only eq. (C.1.3a) is applicable for autoconversion.

Insertion of eq. (B.1) for cloud and eq. (C.1.3a) into eq. (C.1.1) with the change of variable $x = v/v_o$ and evaluatuion of the gain and loss integrals using formulas (A.1) and (A.3), results in the expression

$$\frac{dn}{dt} = a_1 v_o [N(\nu+1)^{\nu+1}]^2 e^{-(\nu+1)x}(Ax^{2\nu+3} - Bx^{\nu+2} - Cx^{\nu}), \qquad (C.1.4)$$

where $A = \Gamma(\nu+3)/\Gamma(2\nu+4)$, $B = (\nu+1)^{-(\nu+1)}$ and $C = \nu+2/(\nu+1)^{\nu+2}$.

The moment tendencies are obtained by multiplying eq. (C.1.4) by $x^n v^{n+1}$ (see Appendix B) and integrating over x. The appropriate integration interval is zero to $x_m = v_m/v_o$, where v_m is the maximum cloud droplet volume (corresponds to r = 41 μm). For typical clouds with mean droplet radii of approximately 10 μm or less, $v_m \gg v_o$ and it follows that a valid approximation of the moment integral obtains for an infinite upper limit. Using formula (A.2) to evaluate the moment tendency integrals, eq. (C.1.4) transforms to

$$\frac{dM_n}{dt} = a_1 v_o^{n+2} N^2 [A\gamma(2\nu+n+4,D) - B\gamma(\nu+n+3,D)$$

$$-C\gamma(\nu+n+1,D)]/(\nu+1)^{n+2}, \qquad (C.1.5)$$

where $A = (\nu+1)(\nu+2)/\Gamma(2\nu+4)$, $B = 1/\Gamma(\nu+1)$, $C = (\nu+1)(\nu+2)/\Gamma(\nu+1)$ and $D = (\nu+1)\, x_m$.

The model moment tendency expressions could in general be derived directly from eq. (C.1.5) with power series approximations of γ. A

wiser choice is to adopt the valid approximation $v_m = \infty$, for two reasons. Since autoconversion is generally rather slow, the first moment tendency as expressed by eq. (C.1.5) would be the result of a small difference of large terms. Furthermore, the incomplete gamma function will vanish from the zeroth moment tendency expression with the amount of necessary computation accordingly reduced. In the limit as v_m approaches infinity, eq. (C.1.5) yields

$$\frac{dM_o}{dt} = - a_1 M_1^2 \, (\nu+2)/(\nu+1). \qquad \text{(C.1.6)}$$

It is easily shown that $\lim_{v_m \to \infty} dM_1/dt = 0$, using the fact that $\lim_{v_m \to \infty} \gamma(\alpha,x) = \Gamma(\alpha)$. This result expresses total water conservation and serves as a useful verification of the rather lengthy analytic procedures employed here.

A hybrid parameterization is used here, wherein the zeroth moment tendency is expressed by eq. (C.1.6) and the first moment tendency is based on empirical curve fits of finite difference coalescence model output. Following Berry and Reinhardt (1974b), a characteristic water content change L and time scale τ is assigned to the autoconversion process. For specified cloud conditions, the quantity L/τ expresses an average autoconversion rate. The appropriate empirical formulas for L and τ are

$$L = 2.7 \times 10^{-2} \, N \, v_o \, (10^{12} r_b^3 \, r_o - 0.4) \qquad [\text{g cm}^{-3}]$$

and

$$\tau = 3.72 \times 10^{-3}(10^{4}r_b - 7.5)^{-1}(Nv_o)^{-1} \quad [s],$$

where $r_o = (3v_o/4\pi)^{1/3}$ and $v_b = v_o(1+\nu)^{-1/2}$ [cm]. The formula for the first moment tendency is

$$\frac{\delta M_1}{\delta t} = -L/\tau \qquad [g\ cm^{-3}\ s^{-1}],$$

since autoconversion decreases cloud water content. The autoconversion is set to zero if $r_b < 7.5$ μm, because the time scale τ becomes infinite at that radius. Droplet concentration decreases via eq. (C.1.6) even if autoconversion is zero, since small coalescing droplets may produce a new droplet smaller than the threshold size of $r_m = 41$ μm. For $\nu = 0$, $r_b = r_o$ and autoconversion commences at $r_o = 7.5$ μm. For $\nu = 3$, autoconversion begins at $r_o = 9.5$ μm. Autoconversion is delayed for narrow droplet distributions. The formulas are based on data in the ranges $10\ \mu m < r_o < 18\ \mu m$ and $0 < \nu < 3$, so that care should be taken in extrapolating the results. The delta notation refers to the units of the tendency, nonetheless representing the substantial derivative.

A development similar to eq. (C.1.5) could be performed for the effect of autoconversion on the rain phase. A simpler representation would be more compatible with the cloud formulation. The formula of Berry and Reinhardt (1974b), which relates rain number concentration to rain mixing ratio during autoconversion, has been adopted here. Expressed in differential form this relation appears as

$$\frac{dN_r}{dt} = 3.5 \times 10^{6} \frac{\delta M_1}{\delta t}.$$

With mixing ratio units appropriate for the bulk model (gg^{-1}), the zeroth and first moment tendencies for cloud are

$$\frac{dM_o}{dt} = -a_1 N_c^2 v_c^2 (\nu_c+2)/(\nu_c+1) \qquad [cm^{-3}s^{-1}] \qquad (C.1.7)$$

and

$$\frac{dM_1}{dt} = -\rho_w L/\rho_a \tau \qquad [gg^{-1} s^{-1}]. \qquad (C.1.8)$$

Using the relation correlating rain mixing ratio to number concentration and employing water conservation, the corresponding rain tendencies are

$$\frac{dM_o}{dt} = -3.5 \times 10^6 \left.\frac{\delta M_1}{\delta t}\right|_c \qquad (C.1.9)$$

and

$$\frac{dM_1}{dt} = -\left.\frac{dM_1}{dt}\right|_c . \qquad (C.1.10)$$

This autoconversion parameterization includes the effects of all possible coalescences since the moment tendencies are based upon integration of the SCE in discretized form. Rain accretion and self-collection are not evaluated during the early stages of coalescence to avoid counting these processes twice when combined with autoconversion. Berry and Reinhardt (1974b) have determined the radius of the predominant drop R_h, at which the peak of the newly formed rain distribution first appears, to be expressed in terms of cloud conditions as

$$R_h = 6.3 \times 10^{-2}/(10^4 r_b - 3.5) \quad [cm].$$

Employing the relation between total drop concentration and mixing ratio with adjustment of the coefficient by a factor of 1.2 to account for the extra time needed for the drop distribution to form a maximum[1], the drop concentration at the time of appearance of the maximum is approximately $N_{rm} = 4.2 \times 10^6$ L. If the radius of the mean volume drop r_o is less than R_h and $N_r < N_{rm}$, only cloud autoconversion is evaluated. Conversely if $r_o > R_h$ and regardless of the value of N_r, additional warm cloud processes such as accretion (Appendix C.2) and hydrometeor self-collection (Appendix C.3) are evaluated. These subjectively chosen conditions on R_h and N_{rm} qualitatively reflect dominance of accretion and self-collection over autoconversion following the emergence of the rain distribution maximum.

Section C.2 Rain accretion of cloud parameterization

In this section, the rain accretion of cloud parameterization is discussed. Because collector drops are much larger than collected droplets, the collection problem is greatly simplified. The governing kinetic equation is the SCE. Only the gain or loss integral in eq. (C.1.1) needs to be evaluated, depending upon whether rain or cloud are considered respectively. This reasoning follows from the separation of the drop distribution into two parts (refer to section C.1).

---

[1]The time necessary to form the rain distribution hump is roughly 1.2 times greater than the time to accumulate rain content L, according to the experimental data of Berry and Reinhardt (1974b).

To determine the cloud response to rain accretion, eq.(B.1) for cloud and rain is inserted along with the appropriate kernel eq. (C.1.2b) into the second (loss) integral in eq. (C.2.1). With the change of variable $x = v/v_c$ and using the integration formula (A.3), there follows

$$\frac{dn}{dt} = -a_2 N_c N_r (\nu_c+1)^{\nu_c+1} e^{-(\nu_c+1)x} (x^{\nu_c+1} + v_r x^{\nu_c}/v_c)/\Gamma(\nu_c+1) \quad . \quad (C.2.1)$$

The moment tendencies are obtained by the same method used in the autoconversion parameterization, except that the upper limit of integration here is infinite and the integration formula (A.3) is employed. The overlap of the lower tail of the rain distribution with the cloud distribution is neglected. The result is

$$\frac{dM_n}{dt} = - a_2 N_c N_r [A\Gamma(\nu_c+2+n) + B\Gamma(\nu_c+1+n)]/\Gamma(\nu_c+1) \quad , \quad (C.2.2)$$

where $A = v_c^{n+1}/(\nu_c+1)^{n+1}$ and $B = v_r v_c^n/(\nu_c+1)^n$. The zeroth and first moment tendencies (mixing ratio in gg^{-1}) are obtained by setting n to zero and unity respectively, in eq. (C.2.2). The moment tendencies for cloud accretion by rain are

$$\frac{dM_o}{dt} = -a_2 N_c N_r (v_c+v_r) \quad (C.2.3)$$

and

$$\frac{dM_1}{dt} = -a_2 N_c N_r v_c \rho_w [(\nu_c+2)v_c/(\nu_c+1) + v_r]/\rho \quad . \quad (C.2.4)$$

This process is active only if $M_{lr} > L$ or $R > R_h$ (see Section C.1). Eqs. (C.2.3) and (C.2.4) are employed only if $R > 50$ μm, due to the range of the collection kernel approximation. An analogous treatment applicable for $R < 50$ μm, where the collection kernel is approximated by eq. (C.1.2a), yields the moment tendency equations

$$\frac{dM_o}{dt} = -a_1 N_c N_r [(\nu_c+2)v_c^2/(\nu_c+1) + (\nu_r+2)v_r^2/(\nu_r+1)] \qquad (C.2.5)$$

and

$$\frac{dM_l}{dt} = -a_1 N_c N_r \rho_w [(\nu_c+3)(\nu_c+2)v_c^3/(\nu_c+1)^2 + (\nu_r+2)v_c v_r^2/(\nu_r+1)]/\rho. \qquad (C.2.6)$$

The corresponding effect of cloud accretion on the rain distribution may be simply treated, since the total concentration of drops remains constant as droplets are collected ($dN_r/dt = 0$). By conservation of mass, $dM_l/dt\big|_r = -dM_l/dt\big|_c$ It follows that

$$\frac{dM_o}{dt} = 0,$$

while

$$\frac{dM_l}{dt} = a_2 N_c N_r v_c \rho_w [(\nu_c+2)v_c/(\nu_c+1) + v_r]/\rho \qquad (C.2.7)$$

for $R > 50$ μm, or

$$\frac{dM_l}{dt} = a_1 N_c N_r \rho_w [(\nu_c+3)(\nu_c+2)\, v_c^3/(\nu_c+1)^2 + (\nu_r+2)v_c v_r^2\, /(\nu_r+1)]/\rho \qquad (C.2.8)$$

for $R < 50\ \mu m$. This process is active only if $R \geq R_h$ or $N_r \geq N_{rm}$ (Appendix C.1).

Section C.3 Large hydrometeor self-collection

The collection of raindrops by other raindrops, designated as the large hydrometeor self-collection mode by Berry and Reinhardt (1974a), is an important factor in the rapid increase in mean drop volume during the later stages of warm cloud coalescence. Inserting eq. (B.1) for rain and eq.(C.1.2b) into eq. (C.1.1) with the change of variables $x = v/v_o$ and evaluation of the gain and loss integrals using formulas (A.1) and (A.3), results in the expression

$$\frac{dn}{dt} = a_2[N(\nu+1)^{\nu+1}/\Gamma(\nu+1)]^2 e^{-(\nu+1)x}(Ax^{2\nu+2} - Bx^{\nu+1} - Cx^{\nu}) \qquad (C.3.1)$$

where $A = \Gamma^2(\nu+1)/2\Gamma(2\nu+2)$, $B = \Gamma(\nu+1)/(\nu+1)^{\nu+1}$ and $C = \Gamma(\nu+2)/(\nu+1)^{\nu+2}$. The corresponding moment tendencies are

$$\frac{dM_n}{dt} = a_2 N^2 v_o^{n+1} [\Gamma(2\nu+3+n)/2(\nu+1)\Gamma(2\nu+2) -$$

$$\Gamma(\nu+2+n)/(\nu+1)\Gamma(\nu+1) - \Gamma(\nu+1+n)/\Gamma(\nu+1)]/(\nu+1)^n, \qquad (C.3.2)$$

appropriate for $R > 50\ \mu m$. A similar treatment using eq. (C.1.2a) for $R < 50\ \mu m$, yields

$$\frac{dM_n}{dt} = a_1 N^2 [(\nu+2)\ \Gamma(\nu+1)\ \Gamma(2\nu+4+n)/(4\nu+6)\ \Gamma(2\nu+2) -$$

$$\Gamma(\nu+3+n) - (\nu+1)(\nu+2)\ \Gamma(\nu+1+n)]/[(\nu+1)/v_o]^{2+n}\Gamma(\nu+1). \qquad (C.3.3)$$

The individual moment tendencies are

$$\frac{dM_o}{dt} = -a_2 N^2 v_o \qquad \text{(C.3.4)}$$

for $R > 50$ μm, or

$$\frac{dM_o}{dt} = -a_1 N^2 v_o^{2(\nu+2)/(\nu+1)} \qquad \text{(C.3.5)}$$

for $R < 50$ μm, and

$$\frac{dM_1}{dt} = 0. \qquad \text{(C.3.6)}$$

Eq. (C.3.6) may be verified by setting n equal unity in either eq. (C.3.2) or eq. (C.3.3). This process is active only if $R \geq R_h$ or $N_r \geq N_{rm}$ (Appendix C.1).

Section C.4 Collisional breakup parameterization

The collisional breakup of raindrops has been investigated by Brazier-Smith et al. (1973) from an observational and numerical standpoint. They study the temporary coalescence of drops in the diameter range of 300 μm to 1500 μm, size ratios of 1.0 to 2.5, and impaction velocities from 0.3 to 3.0 ms^{-1}. Subsequent breakup in this size regime typically produces two large drops much like the original pair as well as several small "satellite" drops. While the number of small drops is strongly affected by satellite drop production, the rainfall rate (and mean volume) are virtually unaffected. Low and List (1982) perform collisional breakup experiments for size combinations of drop pairs with

drops ranging from 395 μm on to 4400 μm. They confirm the existence of the filament breakup mode, and identify additional breakup modes. For drop pairs with minimum diameter exceeding 1000 μm, the smaller colliding drop breaks into numerous fragments. However, these modes dominate the filament mode only for large drop diameters exceeding 3000 μm, which in natural rains occur rather infrequently. It is assumed here that only filament breakup is active, and furthermore that collisional breakup only acts to reduce the overall coalescence efficiency.

Srivastava (1971) has modelled the spontaneous disintegration of raindrops to investigate the role of this process in establishing inverse exponential size distributions. Srivastava (1978) has concluded that spontaneous breakup is negligable, compared with collisional breakup. Consequently, the parameterization neglects spontaneous breakup.

Modelling of collisional breakup is further simplified by adopting the coalescence efficiency of the most frequently colliding drop pair. Berry and Reinhardt (1974c) have demonstrated that the rate of stochastic collection is related to the kernel for the capture of predominate sized drops by drops 1.5 times their radius. The breakup coalescence efficiency is here parameterized by an exponential function of mean drop radius for a drop pair with radius of r_o and 1.5 r_o. Inspection of the coalescence efficiencies of Brazier-Smith et al. (1972) for mean drop radius less than 1 mm and those of Low and List (1982) for large drops at the radius ratio 1.5, reveals that the coalescence efficiency is approximately represented by the expressions

$$E_c = \begin{cases} 1.0 , & r_o < .03 \\ \exp[-50(r_o-.03)], & .03 < r_o < 0.1 \\ 0.0 , & r_o > 0.1 \end{cases} \qquad (C.4.1)$$

where r_o has units of cm. The large hydrometeor self-collection rate eq.(C.3.4) is multiplied by E_c to incorporate the breakup effect.[1]

Section C.5 Cloud droplet condensation growth parameterization

The kinetic equation for cloud droplet condensation growth is (Silverman and Glass, 1973)

$$\frac{dn(v,t)}{dt} = -\frac{\partial}{\partial v}\left[\dot{v}\, n(v,t)\right] , \qquad (C.5.1)$$

where the equivalence of mass and volume in differential terms has been utilized. Here n(v,t) is the cloud number density and $\dot{v}$ is the droplet volume condensation growth rate ($\dot{v} \equiv dv/dt$). The droplet growth is expressed in terms of thermodynamic variables, but secondary curvature and solute effects are neglected. The condensation growth of a droplet is (Pruppacher and Klett, 1978)

$$r\frac{dr}{dt} = C, \qquad (C.5.2)$$

where $C = (s-1)\,(L^2 \rho_w \varepsilon/KR_dT^2 + R_dT\,\rho_w/\varepsilon D\, e_s)^{-1}$. The quantity (s-1) is supersaturation, L is the latent heat of vaporization, ρ_w is water density, R_d is the individual gas constant for dry air, T is temperature, K

[1] E_c may be removed from under the integral sign because it is not a function of v.

is the coefficient of thermal conductivity of air, D is the diffusion coefficient of water vapor in air, and e_s is the equilibrium vapor pressure. Now using eq. (C.5.2), $\dot{v} = 4\pi r^2 \dot{r} = 4\pi r C$. Noting that $r = (3v/4\pi)^{1/3}$, it follows that

$$\dot{v} = 4\pi C(3/4\pi)^{1/3} v^{1/3}. \qquad \text{(C.5.3)}$$

The moment tendencies are obtained by multiplying eq. (C.5.1) by v^u and integrating over v. Then

$$\frac{dM_n}{dt} \equiv \int_0^\infty v^n \frac{dn(v,t)}{dt} dv = -\int_0^\infty v^n \frac{\partial}{\partial v} [n(v,t)\dot{v}] dv.$$

Evaluating the integral by parts, there follows

$$\frac{dM_n}{dt} = n\int_0^\infty \dot{v} n(v,t) v^{n-1} dv - [v^n \dot{v} n(v,t)]\Big|_0^\infty.$$

Using the fact that $\lim_{v\to\infty} n(v) = 0$ and noting from eq. (C.5.3) that $\lim_{v\to 0} \dot{v} = 0$, the above expression is rewritten as

$$\frac{dM_n}{dt} = n \int_0^\infty \dot{v}\, n(v,t) v^{n-1} dv. \qquad \text{(C.5.4)}$$

Substitution of eq. (B.1) for cloud and eq.(C.5.3) into eq. (C.5.4) and utilizing the integration formula (A.3) yields

$$\frac{dM_n}{dt} = 5.405\Gamma(\nu+n+1/3) v_o^{n-1/3} nCN/(\nu+1)^{n-2/3}\Gamma(\nu+1). \qquad \text{(C.5.5)}$$

Note from eq. (C.5.5) that condensation has no effect on the number concentration, which follows from the conservation equation (C.5.1). The first moment tendency (converted to gg^{-1} mixing ratio units) is written

$$\frac{dM_1}{dt} = 5.405\ \rho_w \Gamma(\nu+4/3) v_o^{1/3}\ CN/\rho\ (\nu+1)^{1/3} \Gamma(\nu+1). \qquad (C.5.6)$$

Section C.6 Cloud nucleation parameterization

Cloud condensation nuclei (CCN) may be activated during supersaturated cloud conditions. The degree of supersaturation is a result of the counteracting effects of generation associated with moist-adiabatic or diabatic cooling processes such as saturated rising motion or melting of hail and ice, and depletion via condensation onto activated centers. The space scale of nucleation may be rather small compared to the model resolution, so that a parameterized approach to nucleation appears to be justified (Clark, 1974). Two nucleation regions in the cloud are at inflow boundaries and at internal points where microphysically reduced supersaturation depletion mechanisms no longer balance maintained generating processes.

An expression relating number of activated nuclei N to supersaturation s takes the form

$$N = C\ s^k, \qquad (C.6.1)$$

where $s = q_v/q_{vs}^{-1}$ and C and k are treated as constants for a given air mass type. Twomey (1959) used $k = 0.4$ and $C = 2000\ cm^{-3}$ for continental air in Australia. Alofs and Liu (1981) found $k = 0.643$ and $C = 3990$

($0.0483 < s < 0.681\%$), or $k = 3.85$ and $C = 6.62 \times 10^7$ ($0.013 < s < 0.0483\%$). The control version of the model uses the Alofs and Liu CCN distribution as the cloud boundary condition. The text presents results of a sensitivity test where C is reduced to 1000 cm^{-3}.

Twomey (1959) has obtained approximate expressions for upper bounds of s and N in rising air parcels. After deducing s_{max}, the corresponding value of N_{max} is determined from eq. (C.6.2). The final expression takes the form

$$N_{max} = C^{2/k+2}[A_1^{3/2}\ w^{3/2}/2\pi\ \rho_w A_2 A_3^{3/2}\ k\ B(k/2,3/2)]^{k/k+2}, \qquad (C.6.2)$$

where C and k are as previously defined, w is vertical air velocity ($cm\ s^{-1}$), ρ_w is the density of water ($g\ cm^{-3}$), B is the Beta function, and A_1 through A_3 are thermodynamic quantities. By definition,

$$A_1 = \varepsilon\ L_v g/R_d T^2 c_p - g/R_d T,$$

$$A_2 = R_d T/\varepsilon\ e_s + \varepsilon\ L_v^2\ /p\ T\ c_p,$$

$$A_3 = \rho_w R_v T/e_s\ D_w + L_v\ \rho_w (L_v/R_v T - 1)/K_a T.$$

Also

$$B(k/2,3/2) \equiv \int_0^1 x^{k/2-1}(1-x)^{1/2}dx = \Gamma(k/2)\ \Gamma(3/2)/\Gamma(k+3/2).$$

For $k = 0.643$, B is approximately equal to 2.52.

The cloud nucleation parameterization assumes that nucleation occurs either at the bottom or lateral cloud boundaries, or within the cloud interior where the condensation rate is insufficient to maintain exact saturation. During the semi-implicit adjustment step, the droplet concentration is determined from eq. (C.6.2) at cloud boundary gridpoints with normal inflow. The dynamic tendency of N is effectively replaced by the quasi-Lagrangian treatment implicit in eq. (C.6.2). A mixed Eulerian-Lagrangian modelling approach was proposed by Clark (1974) as a possible technique for mitigating the problem of low spatial resolution at cloud boundaries. At interior cloud gridpoints, eq. (C.6.1) along with an estimate of s from the condensation adjustment step is used to calculate droplet concentration. If $N < \alpha N_{max}$, $(0 < \alpha < 1)$, adjustment yields $N = \alpha N_{max}$. If $N > \alpha N_{max}$, no adjustment occurs. Because eq. (C.6.1) has no time scale associated with it, the parameter α is currently set to 0.5 to reduce the amplitude of possible step increases in N. Adjustments in the cloud interior using eq. (C.6.1) are rather infrequent in comparison to nucleation on the cloud boundaries.

Section C.7 Rain evaporation parameterization

The treatment of rain evaporation in subsaturated air is formally identical to the treatment of cloud condensation growth in supersaturated conditions (Section C.5), except that the saturation ratio $s = q_v/q_{vs}$ is less than unity and the enhancement of vapor diffusion associated with ventilation of the freely falling drops must be accounted for (Pruppacher and Klett, 1978). Substituting rain distribution parameters

for cloud parameters and including the ventilation effect, the bulk evaporation rate is

$$\frac{dq_r}{dt} = 5.405\ \rho_w \Gamma(\nu+4/3)\ v_o^{1/3} C\ f_v N/\rho(\nu+1)^{1/3}\ \Gamma(\nu+1), \quad \text{(C.7.1)}$$

where C is as defined in section C.5 (here $s - 1 < 0$) and the weighted average ventilation factor (Klemp and Wilhelmson, 1978a)

$$f_v = 1.6 + 124.9(\rho q_r)^{0.2046} \quad \text{(C.7.2)}$$

is used.

APPENDIX D

HAIL PARAMETERIZATION

Section D.1 Hail distribution model

The hail distribution is assumed to follow an inverse exponential distribution of the form

$$n(D) = N_{oh} e^{-\lambda_h D}, \qquad (D.1.1)$$

where N_{oh} is the intercept parameter and λ_h is the slope parameter. The intercept parameter is computed from

$$\lambda_h = (\pi \rho_h N_{oh} \rho^{-1} q_h^{-1})^{0.25}, \qquad (D.1.2)$$

where ρ_h is the distribution averaged ice density (g cm^{-3}), ρ is air density, and q_h is hail mixing ratio (gg^{-1}). The histories of individual hailstones are not determined by the model. In all computations involving distribution averaged ice density, ρ_h assumes a value of 0.9 g cm^{-3}. This value is likely to be too high in regions of the cloud with growth conditions conducive to low density riming. The intercept parameter takes the value 4×10^{-4} cm^{-4} (Orville and Kopp, 1977). The diameter dividing the hail distribution ice content in half is $D_o = 3.67 \lambda_h^{-1}$ (Kessler, 1969). The mass-weighted mean terminal fallspeed of the hail distribution is

$$V_h = 1.93\,\lambda_h^{-0.5}\,(4\,g\,\rho_h/3C_D\rho)^{0.5}, \qquad (D.1.3)$$

where g is the acceleration of gravity and C_D is the drag coefficient. In these studies, C_D is taken as 0.6. For true average ice density below 0.9 g cm^{-3}, the fallspeed and sedimentation rate will be overestimated. For example, if ρ_h is actually equal 0.5 g cm^{-3}, fallspeed is 34% too high. The individual hailstone fallspeed is

$$V_T = (4\rho_I gD/3C_D\rho\ )^{1/2}\ , \qquad (D.1.4)$$

where ρ_I is the average ice density (g cm^{-3}) of an individual hailstone. Average ice density ρ_h is a weighted average of $\rho_I(D)$, although the current parameterization does not compute these quantities.

Following Smith et al. (1975), the equivalent radar reflectivity of hail is computed using the formulas

$$Z_e = 1.368 \times 10^{14}\,N_{oh}/\lambda_h^7 \qquad (D.1.5)$$

for dry hail and

$$Z_e = 10^{12}(720\,N_{oh}/\lambda_h^7)^{0.95}\ , \qquad (D.1.6)$$

for wet hail, where Z_e has units of $mm^6\ m^{-3}$. Since ρ_h is currently not a model dependent variable, an assumed value $\rho_h = 0.9$ is used in reflectivity computations. For true values of Z_e and ρ_h of 55 dBZ and

0.5 g cm^{-3} respectively, the computed Z_e value would be 60.1 dBZ (see Appendix E.1 for density correction).

Section D.2 Computation of the incomplete gamma function

The expressions for dry and wet growth of hail require the evaluation of several incomplete gamma functions. The incomplete gamma functions take the forms

$$\gamma(a,x) = \int_0^x t^{a-1}e^{-t}dt$$

and

$$\Gamma(a,x) = \Gamma(a) - \gamma(a,x),$$

where a is a specified constant, x is the independent variable and $\Gamma(a)$ is the complete gamma function. A lookup table is used to store computed values of $\gamma(a,x)$ for a range of x values, and interpolation in x allows simple computation of approximate values. $\Gamma(a)$ is specified for the particular set of constants used in the parameterization. The incomplete gamma function is asymptotic for large x, and is expressed in terms of the confluent hypergeometric Kummer function as (Abramowitz and Stegun, 1964)

$$\gamma(a,x) = a^{-1}x^a e^{-x}M(1,1+a,x), \qquad (D.2.1)$$

Values of $\gamma(a,x)$ are computed from eq.(D.2.1) for small x. In the limit of large x, the hypergeometric function is expressed as (Abramowitz and Stegun, 1964)

$$M(1,1+a,x) = \Gamma(1+a)\, e^x x^{-a}$$

so that

$$\lim_{|x|\to+\infty} \gamma(a,x) = a^{-1}x^a e^{-x}\Gamma(1+a)\, e^x x^{-a} = a^{-1}\Gamma(1+a). \quad \text{(D.2.2)}$$

The values of the parameter a range between one and four in the hail parameterization. Computation of $\gamma(a,x)$ for these values and for $x \leq 30$ shows that $\gamma(a,x)$ has attained the asymptotic value predicted by eq. (D.2.2) near $x = 10$. $\gamma(a,x)$ is a strong function of x for $x \leq 10$ only. Consequently, values of $\gamma(a,x)$ may be tabulated for $x \leq 10$ with eq.(D.2.2) used for $x > 10$.

The parameterization utilizes values of $\gamma(a,x)$ or $\Gamma(a,x)$ for a = 1, 2, 3.5 and 4.0. Tabulated values of $\gamma(a,x)$ for specified value of x are shown in the following table:

x	$\gamma(1.0,x)$	$\gamma(2.0,x)$	$\gamma(3.5,x)$	$\gamma(3.66,x)$
0.01	9.95 (-3)	4.96 (-5)	2.83 (-8)	1.29 (-8)
0.05	4.87 (-2)	1.20 (-3)	7.68 (-6)	4.54 (-6)
0.1	9.51 (-2)	4.67 (-3)	8.36 (-5)	5.52 (-5)
0.5	3.93 (-1)	9.02 (-2)	1.71 (-2)	1.46 (-2)
1	6.32 (-1)	2.64 (-1)	1.33 (-1)	1.26 (-1)
2	8.64 (-1)	5.93 (-1)	7.31 (-1)	7.67 (-1)
4	9.81 (-1)	9.08 (-1)	2.21 (0)	2.53 (0)
6	9.97 (-1)	9.82 (-1)	2.98 (0)	3.52 (0)
8	9.99 (-1)	9.96 (-1)	3.23 (0)	3.86 (0)
10	9.99 (-1)	9.99 (-1)	3.30 (0)	3.95 (0)
∞	1.00 (0)	1.00 (0)	3.32 (0)	4.00 (0)

The row corresponding to $x = \infty$ contains values specified according to eq. (D.2.2). Additionally, $\Gamma(2.0) = 1.0$, $\Gamma(3.5) = 3.32$, and $\Gamma(4.0) = 6.0$. Linear interpolation on γ yields less than 5% error for $1 \leq x \leq 10$.

Section D.3 Transition diameter D_w for dry/wet growth

There exists a hailstone diameter D_w such that, for given ambient conditions and steady hailstone heat content, a hailstone grows in the dry mode with diameter $D < D_w$ and in the wet mode for $D > D_w$. Nelson (1983) provides expressions for the fraction of accreted water frozen during wet growth (F_f), as well as for mass accumulation rates of cloud water and ice crystals on a growing hailstone. At the transition state from dry to wet growth, the surface of the hailstone is at freezing and 100% of the accreted water is frozen. Corresponding parameter values are $T_s = 273.1$ °K and $F_f = 1.0$, while the difference between the temperatures of the environment and growing hailstone is the environmental undercooling (ΔT). Inserting the transition state parameter values into the expression for fraction of accreted water frozen and solving for D_w, there follows

$$D_w = [A(E_w r_w(L_f + C_{pw}\Delta T) + E_i r_i C_{pi}\Delta T) / (K\Delta T - L_v d_i \Delta\rho)]^{-4/3}, \qquad (D.3.1)$$

where $A = (4\ g\ \rho_h/3C_D\rho)^{1/4}/2.32(\rho/\mu)^{1/2}$. In eq. (D.3.1), r_w and r_i are the cloud and ice mixing ratios respectively, E_w and E_i are the water and ice collection efficiencies respectively, and ρ_h is hailstone density.

Assuming $\rho_h = 0.9$ g cm^{-3}, $E_w = 0.8$ (corresponding to mean hail diameter of 0.5 cm and mean droplet radius of 10 μm) and $E_i = 1.0$, eq. (D.3.1) may be evaluated for a range of temperatures and cloud and ice

water contents. The resulting data table is then used to fit an empirical expression for D_w. Computations are performed over the temperature range zero to -29°C, cloud water range of 0.25 to 7.5 g m^{-3}, and ice content range from zero to 5.0 gm^{-3}. An exponential function is found to fit the data rather well, with errors less than 0.1 cm in the range of mean hailstone volume diameters corresponding to hail mixing ratios from 1 to 10 g m^{-3}. This function takes the form

$$\hat{D}_w = \exp(\Delta T/(11\ W_c - 1.3\ W_i + 1)) - 1, \qquad (D.3.2)$$

where ΔT is environmental undercooling (°C), W_c is cloud water content (g m^{-3}), and W_i is ice content (g m^{-3}). In mixing ratio units of q (gg^{-1}), the expression has the alternate form

$$\hat{D}_w = \exp(\Delta T/(1.1 \times 10^7 \rho q_c - 1.3 \times 10^6\ \rho q_i + 1)) - 1, \qquad (D.3.3)$$

where q_c and q_i are cloud and ice mixing ratios and ρ is air density (g cm^{-3}).

Section D.4 Hail dry growth parameterization

In this section, the bulk accretion rate of cloud under dry growth conditions is deduced. Since ice crystal sticking efficiency is normally very small for dry growth conditions, ice accretion is neglected in the treatment. The current treatment of dry growth differs significantly from previous efforts (Wisner et al., 1972; Orville and Kopp, 1977), which effectively assume that a single growth mode is applicable to the entire hail distribution. This parameterization partitions the

hail distribution according to the dry/wet growth threshold diameter D_w (Appendix D.4), with dry growth taking place only for hail with $D < D_w$. This parameterization also acknowledges the importance of low density riming during dry growth, and attempts to include the effect of low ice density on fallspeed[1] in the computation of the dry growth accretion rate. Previous Eulerian parameterized models assume solid ice density during dry growth, which may produce serious model bias errors.

The bulk dry growth rate is written as

$$\frac{dq_h}{dt} = \int_0^{D_w} E_c q_c V_T \frac{\pi D^2}{4} \, n(D) \, dD, \qquad (D.4.1)$$

where D_w is the transition diameter for dry to wet growth, E_c is the collection efficiency, q_c is cloud water mixing ratio, V_T is individual hailstone terminal fallspeed, and $n(D)$ is number concentration density of hail. Since in general both E_c and V_T are functions of D, expressions for these quantities are needed to evaluate eq. (D.4.1). Additionally, varying rime density affects average hail density which in turn affects V_T.

The collection efficiency E_c is a function of collector and collected particle size. An approximate empirical formula for E_c based on the computed collection efficiencies of Bailey and Macklin (1966) is

$$\hat{E}_c (D,r) = \exp(-11.4 \, r^{-1.6} D), \qquad (D.4.2)$$

---

[1] A lower density reduces fallspeed. See eq. (D.1.4).

where r is droplet radius (μm) and D is hailstone diameter (cm). The fit, valid at -20°C and for $C_D = 0.55$, has less than 15% error for $D < 2$ cm. The curve has been fit to yield zero error at $D = 1.0$ cm and $5\ \mu m < r < 30\ \mu m$. The expression assumes the boundary condition $E_c(0,r) = 1.0$. The mean value theorem may be applied to E_c in eq. (D.4.1) in order to bring it outside the integral sign. The average collection efficiency $\bar{E}_c$ is approximated by $\hat{E}_c(D_o, r_o)$, where D_o and r_o are respectively the mean hail diameter and mean volume droplet radius.

The individual fallspeed is proportional to ice density ρ_I. Although the model does not compute individual ice density, the average ice density is related to the ice layer (rime) density ρ_L. The rime density ρ_L may be written as

$$\rho_L = a(v_o d/2T_s)^b, \qquad \text{(D.4.3)}$$

where a and b are constants, d is droplet diameter (μm), v_o is impaction speed (ms^{-1}), and T_s is the absolute value of hailstone surface temperature (for dry growth, $T_s < 0°C$). Macklin (1962) found $a = 0.11$ and $b = 0.76$, while Pflaum et al. (1979) found $a = 0.261$ and $b = 0.38$. In this study, $a = 0.2$ and $b = 0.5$.

Surface temperature T_s can be mathematically modelled as a weighted average of wet growth conditions ($T_s = 0$) and ambient conditions ($T_s = T_a$). The weights are expressed in terms of the hailstone heat balance condition. The surface temperature varies approximately as a linear function of D in the heat balance relation. With the boundary

conditions $\lim_{D\to 0} T_s = T_a$ and $T_s = 0$ at $D = D_w$, the surface temperature is approximated by

$$T_s = T_a(1-D/D_w), \qquad (D.4.4)$$

where T_s and T_a are absolute values of surface and ambient temperatures (°C) respectively, and D is hailstone diameter (cm). The concentration weighted surface temperature may be obtained by combining eq. (D.4.4) and the hail distribution function (D.1.2), integrating from zero to D_w using formula (A.2), and normalizing by total hail number concentration $N_t = N_{oh}/\lambda_h$. The resultant average temperature is

$$\bar{T}_s = [\gamma(1,\lambda_h D_w) - \gamma(2,\lambda_h D_w)/\lambda_h D_w]T_a, \qquad (D.4.5)$$

Now expressing impaction velocity as $v_o = cv_T$ $(0 < c < 1)$ and using $\bar{T}_s$ in place of T_s, eq. (D.4.3) gives

$$\rho_L = [a(10^{-2}cd(4g/3C_D\rho)^{1/2}/2\bar{T}_s)^b]^{1/1-b/2}\ D^{b/2-b}\ . \qquad (D.4.6)$$

Making the crude assumption that $\rho_I = \rho_L$[1] and substituting eq.(D.4.6) into eq.(D.1.4), the individual fallspeed is finally expressed as

---

[1]This assumption may be better than $\rho_I = 0.9$ g cm^{-3}. A possible model improvement is the addition of ρ_I as a model dependent variable. Average ice density would then vary by advection, diffusion, the riming rate, and other factors. Inclusion of advection would effectively incorporate growth history along the predominant hail trajectory.

$$V_T = [a(10^{-2}cd/2\bar{T}_s)^b \ (4g/3C_D\rho)]^{1/2-b}D^{1/2-b} \ . \qquad (D.4.7)$$

In the study, the impaction parameter c is set to 0.75.

The bulk dry growth rate may now be evaluated. Inserting $\hat{E}_c$, eq. (D.4.7) and eq.(D.1.2) into eq.(D.4.1) with use of the formula (A.2) yields

$$\frac{dq_h}{dt} = 0.25\pi \ N_{oh}\bar{E}_c q_c [a(10^{-2}cd/2\bar{T}_s)^b \ (4g/3C_D\rho)]^{1/2-b} \ x$$

$$\lambda_h^{-(7-3b)/(2-b)}\gamma(7-3b/2-b,\lambda D_w). \qquad (D.4.8)$$

The incomplete gamma function γ is numerically evaluated using formulas in Appendix D.2.

Closure is imposed on the cloud distribution by specifying that the cloud mean volume does not change with accretion by hail. Differentiating the first moment and holding v_c constant yields

$$\frac{dN_c}{dt} = \rho \ \frac{dq_c}{dt} \ /v_{c,} \ . \qquad (D.4.9)$$

Conservation implies $dq_c/dt = - dq_h/dt$.

Sensitivity tests on the effect of assuming high density ice on the subsequent accretion rates and hail content utilize an equation very similar to eq.(D.4.8) except that ρ_I here is a prespecified constant. The bulk dry growth rate in this special case is

$$\frac{dq_h}{dt} = 0.25\pi\, N_{oh}\bar{E}_c\, q_c(4\rho_I g/3C_D\rho)^{1/2}\, \lambda_h^{-3.5}\, \gamma(3.5,\lambda_h D_w). \qquad (D.4.10)$$

In the sensitivity tests $\rho_I = 0.9$ g cm^{-3}.

Section D.5 Hail wet growth parameterization

Hailstones for which diameter $D > D_w$, grow in the wet regime with $\rho_I = 0.9$ g cm^{-3}. The individual wet growth rate may be written as (Musil, 1970)

$$\frac{dM}{dt} = 2\pi DC(\rho LD\Delta q_v - K_a T_a)/L_f + C_w T_c +$$

$$\rho\pi D^2 V_T q_i E_i (1 - C_{pi} T_c/(L_f + C_{pw} T_c)), \qquad (D.5.1)$$

where C is the hail ventilation coefficient, ρ is air density (g cm^{-3}), L is latent heat of vaporization, D is diffusivity, q_v is vapor mixing ratio (gg^{-1}), k_a is conductivity, T_c is temperature (°C), V_T is terminal fallspeed (ms^{-1}), q_i is ice mixing ratio (gg^{-1}), L_f is latent heat of fusion, and M is hailstone mass (g).

The bulk wet growth rate is written

$$\frac{dq_h}{dt} = \int_{D_w}^{\infty} \rho^{-1} \frac{dM}{dt}\, n(D)\, dD, \qquad (D.5.2)$$

where ρ is air density, $\frac{dM}{dt}$ is the individual growth rate, and n(D) is number concentration density. Inserting eq. (D.5.1), eq. (D.1.1), and eq. (D.1.4) into eq.(D.5.2) and using formula (A.2), the wet growth rate is

$$\frac{dq_h}{dt} = 2\pi\ C\ N_{oh}\ (\rho L_v D\Delta q_v - K_a T_c)\Gamma(2,\lambda_h D_w)/\rho(L_f + C_w T_c)\ \lambda_h^2$$

$$+ \pi\ N_{oh} q_i E_i (4g\rho_h/3C_D\rho)^{1/2}\ (1 - C_{pi}T_c/L_f + C_{pw}T_c) \cdot$$

$$\Gamma(3.5,\ \lambda_h D_w)/4\lambda_h^{3.5}. \qquad \text{(D.5.3)}$$

The incomplete gamma function Γ is evaluated numerically using formulas in Appendix D.2.

The wet growth expression need not be evaluated if the fraction of ice residing at diameters greater than D_w is negligible compared to the total hail mass. Now the hail mixing ratio for $D > D_w$ is

$$q_w = \rho_h \pi\ N_{oh} e^{-\lambda_h D_w} (D_w^3\lambda_h^3 + 3D_w^2\lambda_h^2 + 6D_w\lambda_h + 6)/6\rho\lambda_h^4. \qquad \text{(D.5.4)}$$

Now let $\varepsilon = q_w/q_h$, where q_w is evaluated from eq. (D.5.4). If $\varepsilon < \varepsilon_o$, wet growth is not evaluated. For these studies ε_o is set to 0.05.

The term Δq_v is the difference between saturation vapor mixing ratio at the hailstone surface and the far environment. Assuming a plane water surface at 0°C for the hailstone surface condition, this difference is expressed as $\Delta q_v = q_{vo} - q_v$, where q_v is the environmental mixing ratio. At the hailstone surface, it follows that $q_{vo} = \varepsilon\ e_{so}/p = 3.8/p$, with p being air pressure (mb). The vapor deviation may be reexpressed as $\Delta q_v = 3.8/p - q_v$.

The hailstone ventilation coefficient C may be computed from

$$C = 0.58(\rho D V_t/\mu)^{1/2},$$

where ρ is air density, D is hail diameter, V_T is terminal fallspeed, and μ is dynamic viscosity. The distribution averaged value of C, computed from $\bar{C} = .58(\rho D_o V_h/\mu)^{1/2}$ with T = 0° C, $\rho = 7 \times 10^{-4}$ g cm^{-3}, and $q_h = 10^{-3}$ gg^{-1}, is approximately equal to 10. These values are representative of conditions in modelled wet growth zones[1]. Closure is imposed on the cloud distribution in a manner identical to that for the hail accretion of cloud with dry growth (Appendix D.4).

Section D.6 Hail melting to rain

Following Orville and Kopp (1977) and considering only conduction, forced convection and evaporation effects, hail melting is represented as

$$\frac{dq_h}{dt} = 2\pi N_{oh}(K_a T_c + L_v D\rho\Delta q_v)\left[1.6/\lambda_h^2 + 0.48(4g\rho_I/3C_D\rho)^{1/4}/\nu^{1/2}\,\lambda^{2-3/4}\right]/\rho L_f, \qquad \text{(D.6.1)}$$

where L_v is latent heat for vaporzation, L_f is latent heat of fusion, K_a is thermal conductivity of air, T_c is temperature (°C), ν is the kinematic viscosity of air, C_D is the drag coefficient, D is vapor diffusivity, and Δq_v is the difference of environmental vapor mixing ratio and saturation mixing ratio at the hailstone surface (water coating assumed to be at equilibrium with ice).

Closure is imposed on the rain distribution by assuming that melting hail produces drops with a mean diameter of 1 mm. This assumption

[1]Under the same conditions, individual hailstones with D > 1 cm have C values approaching 50 or greater.

is justified to a limited extent by the observations of Joe et al. (1980). The parameterization could alternatively assume that the drop number concentration increase is equal to the hail number concentration decrease accompanying the decrease in hail mixing ratio. The melting behavior of individual ice particles and the subsequent disposition of the meltwater is more precisely a complicated function of the ice particle Reynolds number (Rasmussen et al.[1], 1982). The problem of converting the Lagrangian formulation of such a model to the current parameterized model appears to be intractable. The concentration change is expressed by the change in rain mixing ratio in a gamma distribution with the specified mean diameter. If q_r and N_r denote the initial value of the mixing ratio and drop concentration respectively, with a star indicating the appropriate adjusted value, there the change in number concentration is

$$N_r^* - N_r = \rho(q_r^* - q_r)/v_o, \qquad \text{(D.6.2)}$$

and v_o is the mean volume corresponding to the specified mean diameter. By conservation of water substance, $dq_r/dt = - dq_h/dt$.

Section D.7 Hail accretion of ice

Hail is assumed to accrete ice crystals during wet growth only. Thermal effects associated with this process are neglected. The collection efficiency of wet hail for ice crystals is assumed to be

[1]Rasmussen, R.M., V. Levizzani and H.R. Pruppacher, 1982; A theoretical and wind tunnel study of the melting behavior of small and large spherical ice particles. **Proceedings**, Conf. Cloud Physics, Chicago, AMS, 587 pp.

unity. The expression for continuous collection of ice is a simple modification of the continuous growth expression for cloud of Orville and Kopp (1977), where an integration from the threshold diameter D_w (Appendix D.3) to infinity replaces an integration over all diameters with attendant utilization of the incomplete gamma function (Appendix A). The continuous collection of ice by wet hail is

$$\frac{dq_h}{dt} = \pi N_{oh} E_i q_i (4g\rho_I/3C_D\rho)^{1/2} \Gamma(3.5,\lambda_h D_w)/4\lambda_h^{3.5}, \qquad (D.7.1)$$

where Γ is the incomplete gamma function and E_i is the collection efficiency for ice. Values of Γ are computed using formulas in Appendix D.2.

APPENDIX E

ICE PARAMETERIZATION

Section E.1 Ice distribution model

The ice distribution model is identical in form to the hail distribution model (Appendix D.1) and is written as

$$n(D) = N_{oi} e^{-\lambda_i D}, \qquad \text{(E.1.1)}$$

where N_{oi} is the intercept parameter and λ_i is the slope parameter. The slope parameter is computed from

$$\lambda_i = (\pi \rho_i N_{oi} \rho^{-1} q_i^{-1})^{0.25}, \qquad \text{(E.1.2)}$$

where ρ_i is ice density (g cm^{-3}), ρ is air density, and q_i is ice mixing ratio (gg^{-1}). A value for ρ_i of 0.5 g cm^{-3} is used in this study. The intercept parameter takes the value of (Houze et al., 1979) $N_{oi} = 10^{-1}$ cm^{-4}. This value of N_{oi} is also supported by in-situ T-28 ice particle measurements in a Colorado storm (Heymsfield and Musil, 1982). The ice concentration is expressed by $N_T = N_{oi} \lambda_i^{-1}$. The mass-weighted mean fallspeed of the ice distribution is (Ogura and Takahashi, 1971)

$$V_i = 31.2 \, f_o (\rho q_i)^{0.12} (\rho_o / \rho)^{0.5}, \qquad \text{(E.1.3)}$$

where V_i is in ms^{-1} and the parameter f_o is set to 0.37 to simulate graupel-like particles. An altitude correction has been added to the terminal velocity formula, after Foote and du Toit (1969).

The ice radar reflectivity is computed using the Rayleigh approximation of Smith et al. (1975) for small hail, which is analogous to eq. (D.1.5) but includes a correction for reduced ice density. The resulting expression is

$$Z = 7.2 \times 10^{14}(|K_i|^2/|K_r|^2)N_{oi}/\lambda_i^7 , \qquad \text{(E.1.4)}$$

where the dielectric constant for ice is expressed as $|K_i|^2 = 0.243\ \rho_i^2$ (Battan, 1973), the rain dielectric constant $|K_r|^2 = 0.93$, and Z has units of $mm^6\ m^{-3}$.

Section E.2 Raindrop freezing to ice

Frozen drops are identified with small precipitating ice due to the great similarity between distribution shape and mean size of rain and ice. Following Wisner et al. (1972), the change in number of liquid drops per unit volume due to freezing is written as

$$\frac{dN}{dt} = B'Nv(e^{A'T_c}-1), \qquad \text{(E.2.1)}$$

where A' and B' are the Bigg (1953) freezing parameters, the quantity T_c is the undercooling, N is drop number concentration, and v is drop volume. Inserting eq. (E.1) for rain into eq. (E.2.1), converting from mass density to mixing ratio (gg^{-1}) units, and integrating over all v

with integral evaluation using formula (A.3), the freezing rate is written as

$$\frac{dq_r}{dt} = \rho_w B'N(\nu+2)v_o^2 \, (e^{A'T_c}-1)/\rho(\nu+1) \qquad \text{(E.2.2)}$$

and

$$\frac{dN}{dt} = B'Nv_o(e^{A'T_c}-1).$$

Considering the properties of the gamma distribution, the associated tendency of mean volume is

$$\frac{dv_o}{dt} = B'v_o^2(e^{A'T_c}-1)/\nu+1,$$

a quantity that is greater than zero for all v_o and $\nu > -1$. For millimetric drops at -10°C, $\Delta v_o/v_o \sim 10^{-3}$ so that Δv_o is negligable. Hence during freezing, we set v_o = constant. The rain distribution is closed by

$$\frac{dN_r}{dt} = \rho \frac{dq_r}{dt} /v_o \, . \qquad \text{(E.2.3)}$$

From conservation $dq_i/dt = - dq_r/dt$.

Section E.3 Cloud ice nucleation parameterization

Ice crystals are nucleated at sub-freezing temperatures and at the expense of supercooled cloud water. This treatment is justified to a limited degree by Ostwald's rule of stages (Pruppacher and Klett, 1978) which states that a supersaturated phase (water vapor) does not directly

transform into the most stable state (ice), but rather into the next most stable or metastable state (supercooled water). Nucleation is assumed to occur only at water saturation and in the presence of the liquid phase. This is a reasonable approximation since only a negligible volume of the cloud core is (water) cloud-free and supersaturated with respect to ice.

Fletcher (1962) gives the number of ice nuclei N_i (g^{-1}) as

$$N_i = N_o \, e^{aT_c}, \qquad \text{(E.3.1)}$$

where T_c is the undercooling (°C), N_o has a value of 10^5 g^{-1} and the parameter a has a value of $0.6°C^{-1}$. The mixing ratio of nucleated ice particles may, with the input of eq.(E.3.1), be written as

$$\hat{q}_i = \rho_i v_i N_o e^{aT_c}, \qquad \text{(E.3.2)}$$

where v_i is an equivalent mean nucleated ice crystal volume and ρ_i is nucleated crystal density (g cm^{-3}). A value of v_i equal to 5.23×10^{-10} cm^3 is used here, which corresponds to a spherical particle of radius 5 μm. A value of ρ_i equal to 0.9 is also picked. In a virtually identical treatment, Rutledge (1983) picks a radius of 6.4 μm. In the presence of supercooled liquid cloud, q_i must at least equal the value prescribed by eq. (E.3.2) at any time. If necessary, the ice mixing ratio is increased to $\hat{q}_i$ and the cloud mixing ratio is proportionally

decreased. Cloud total number concentration is assumed to remain unchanged while mean volume v_o changes according to

$$\frac{dv_o}{dt} = \rho \frac{dq_c}{dt}/N_c. \qquad \text{(E.3.3)}$$

Effectively, cloud evaporates in order to supply the water vapor necessary for ice nucleation.

Section E.4 Ice riming of cloud

Riming of supercooled cloud water by size-distributed ice particles is parameterized in a fashion analogous to the Kessler (1969) rain accretion of cloud process. Houze et al. (1979) have demonstrated that snow crystals at altitude are distributed approximately according to an inverse exponential function, identical in form and in value of intercept parameter (see Appendix E.1) to that used by Kessler to describe rain. Adopting the form of the accretion equation used by Soong and Ogura (1973) for rain, substitution of q_i for q_r with appropriate modification of the coefficient gives

$$\frac{dq_i}{dt} = 2.2 \left|V_i/V_{ri}\right| E_{ic} q_c q_i^{0.875}, \qquad \text{(E.4.1)}$$

where E_i is the ice collection efficiency for cloud, V_i is the mass-weighted ice terminal fallspeed, and V_{ri} is the mass-weighted rain fallspeed associated with the given ice mixing ratio q_i. The ratio of terminal fallspeed effectively adjusts the collection rate for the lower ice terminal fallspeed. E_{ic} is varied between 0.5 and 1.0 to represent the complex and varied geometries of naturally occurring ice

particles. The fallspeed V_i is computed from eq.(E.1.3), while the fallspeed V_{ri} is computed from eq.(B.7) with insertion of q_i for q_r. Cloud mean volume is assumed to be constant during riming so that

$$\frac{dN_c}{dt} = \rho \frac{dq_c}{dt}/v_o. \qquad \text{(E.4.2)}$$

From conservation $dq_c/dt = -dq_i/dt$.

Section E.5 Deposition growth of ice

Ice crystals grow by vapor diffusion and deposition at the expense of coexisting cloud water in this parameterization. Deposition is neglected at water sub-saturation because water saturated conditions dominate in the cloud core. Deposition growth at sub-water saturation is likely to occur in precipitation debris regions, and could be included as a future model improvement. Koenig (1971) represents the depositional growth of a single crystal by

$$\frac{dm}{dt} = A_1 m^{A_2}, \qquad \text{(E.5.1)}$$

where m is the crystal mass (g) and A_1 and A_2 are temperature-dependent parameters. This rate could be scaled down to describe deposition at sub-water saturation. The crystal mass may be approximately related to diameter by the expression $m = 5.0 \times 10^{-4} D^2$ (Pruppacher and Klett, 1978). This expression combines a crystal density of 0.5 g cm^{-3} with an

appropriate expression for dendritic crystal volume. The change in mixing ratio by deposition growth has the form

$$\frac{dq_i}{dt} = \int_0^\infty \rho^{-1} \frac{dm}{dt} n(D)dD.$$

Inserting eq. (E.5.1) modified for dendritic crystal mass, and eq. (E.1.1) into the above expression and integration using formula (A.3) yields

$$\frac{dq_i}{dt} = N_{oi}A_1(5 \times 10^{-4})^{A_2}\Gamma(2A_2+1)/\rho\ \lambda_i^{2A_2+1}.$$

The parameter A_2 varies from 0.39 to 0.58 over a temperature range of 0° to -31°C, while A_1 varies over several orders of magnitude in the same temperature range. Since A_1 dominates the variability of the deposition rate, A_2 is set to 0.5. Then the final form of the deposition growth rate is

$$\frac{dq_i}{dt} = 2.2 \times 10^{-2}A_1N_{oi}/\rho\ \lambda_i^2 . \qquad \text{(E.5.2)}$$

Cloud total number concentration is assumed to be constant during deposition growth. Then

$$\frac{dv_c}{dt} = \rho\frac{dq_c}{dt}/N_c . \qquad \text{(E.5.3)}$$

From conservation $dq_c/dt = - dq_i/dt$.

Section E.6 Ice/hail conversion

A fraction of the total ice content is due to millimetric rimed particles. These particles may serve as hail embryos, and their transfer to the hail distribution should be represented. The transferred mass is accounted for by the total mixing ratio of ice particles having diameters exceeding an assumed minimum diameter D_g, which may be appropriate for small graupel. This quantity q_{ih} is

$$q_{ih} = \rho_i \pi N_{oi} e^{-\lambda D_g} (D_g^3 \lambda_i^{-1} + 3D_g^2 \lambda_i^{-2} + 6D_g \lambda_i^{-3} + 6\lambda_i^{-4})/6\rho, \quad \text{(E.6.1)}$$

where ρ_i is the graupel particle density (g cm^{-3}). In this study ρ_i is set to 0.5 g cm^{-3} and D_g is varied in the range of 0.1 to 0.5 cm. The hail mixing ratio q_h is increased by q_{ih}, with q_i decreased accordingly.

Section E.7 Cloud ice melting to rain

Following Ogura and Takahashi (1971), the melting rate of cloud ice is written as

$$\frac{dq_i}{dt} = 2.27 \times 10^{-6} C\, T_c (\rho q_i)^{0.525} / \rho\, f_o^{0.42}, \quad \text{(E.7.1)}$$

where C is the ventiliation coefficient given by

$$C = 1.6 + 5.7 \times 10^{-4} V_i^{1.5} / f_o$$

and the terminal fallspeed V_i (cm s^{-1}) is computed from eq.(E.1.3). Following the recommendation of Ogura and Takahashi, the parameter f_o is set at 0.37 to represent graupel pellets.

To impose closure with the rain distribution, the drop number concentration increase is assumed to be equal to the ice number concentration decrease accompanying the decrease in ice mixing ratio. The concentration change is expressed by the change in the ice distribution slope parameter λ_i(Appendix E.1) during the adjustment step. If λ and N_r denote the initial value of the slope parameter and drop concentration, respectively, with a star indicating the appropriate adjusted value, then the change in number concentration is

$$N_r^* - N_r = N_o(\lambda^* - \lambda)\ /\lambda^2. \qquad \text{(E.7.2)}$$

From conservation $dq_r/dt = - dq_i/dt$.

Section E.8 Sublimation of ice to vapor

Following Ogura and Takahashi (1971), the sublimation rate of ice is written as

$$\frac{dq_i}{dt} = C(1-q_v/q_{is})(\rho q_i)^{0.525}/\rho\ f_o^{0.42}(7 \times 10^5 + 2.5\times10^6/pq_{is}), \qquad \text{(E.8.1)}$$

where q_v is vapor mixing ratio (gg^{-1}), q_{is} is saturation mixing ratio with respect to a plane ice surface (gg^{-1}), and p is pressure (mb). Ice sublimation occurs at sub-ice saturation only. The ventilation coefficient C is defined in Appendix F.

APPENDIX F

CLOUD ICE SUBLIMATION

The sublimation of small non-precipitating cloud ice particles is governed approximately by a diffusion equation of the form (Rogers, 1976)

$$\frac{dM}{dt} = 4\pi\ CD(\rho_v - \rho_{si}), \qquad (F.1)$$

where M is particle mass (g), C is the electrical capacitance (cm), D is the vapor diffusivity of air ($cm^2\ s^{-1}$), ρ_v is vapor density of the ambient air ($g\ cm^{-3}$), and ρ_{si} is the saturation vapor density over ice ($g\ cm^{-3}$). In the parameterization, frozen cloud droplets with $r \approx 10\ \mu m$ are the only source of cloud ice. The capacitance assumes the spherical value C=r, and r is set to 10^{-3} cm (the mass M_x of the particle is 3.76×10^{-9} g). The diffusivity has an approximate value $D = 0.226\ cm^2 s^{-1}$. Rewriting eq.(F.1) in terms of the gradient of mixing ratio of vapor and assuming a monodisperse cloud ice distribution with mixing ratio q_x (gg^{-1}) and concentration (number per gram of air) $N_x = q_x/M_x$, we write the mixing ratio tendency in the form

$$\frac{dq_x}{dt} = 7.6 \times 10^5 \rho (q_v - q_{si}) q_x.$$

Here ρ is air density ($g\ cm^{-3}$), q_v is ambient vapor mixing ratio (gg^{-1}), and q_{si} in the saturation mixing ratio over ice (gg^{-1}).